Article

Cell Metabolism

Cystine import and oxidative catabolism fuel vascular growth and repair via nutrient-responsive histone acetylation

Graphical abstract

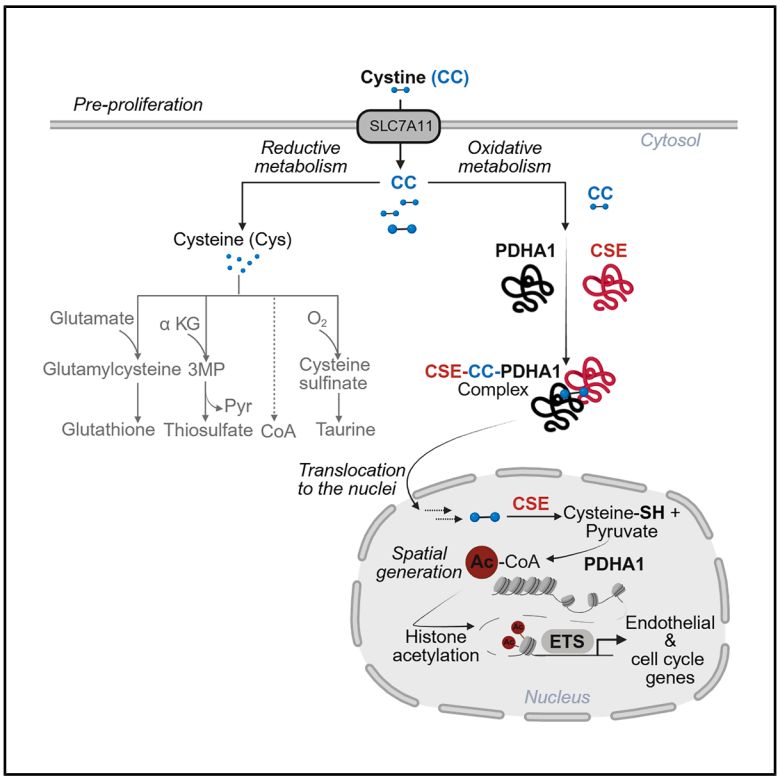

Highlights

- Endothelial cells shift metabolism prior to division, altering cystine import
- Nuclear cystine oxidation boosts acetyl-CoA, decorating histones and opening chromatin
- Reduced cystine oxidation skews endothelial transcription, impairing vascular growth
- Aging cuts cystinolysis, but cystine delivery enhances vascular repair after injury

Authors

Maria-Kyriaki Drekolia, Janina Mettner, Daiyu Wang, ..., Gergana Dobreva, Jiong Hu, Sofia-Iris Bibli

Correspondence

iris.bibli@medma.uni-heidelberg.de

In brief

Drekolia, Mettner, Wang et al. identified a nuclear metabolic pathway—triggered before cell division—that burns cystine to regulate the epigenome, unlock chromatin, and prime endothelial gene programs. This nutrient-responsive epigenetic circuit wanes with age, yet dietary cystine revives endothelial transcription and restores vessel growth in injury, disease, and aging.

Drekolia et al., 2026, Cell Metabolism *38*, 115–134
January 6, 2026
https://doi.org/10.1016/j.cmet.2025.10.003

CellPress

Cell Metabolism

CellPress
OPEN ACCESS

Article

Cystine import and oxidative catabolism fuel vascular growth and repair via nutrient-responsive histone acetylation

Maria-Kyriaki Drekolia,[1,2,20] Janina Mettner,[1,2,20] Daiyu Wang,[3,20] Fredy Delgado Lagos,[1] Christian Koch,[1] Dennis Hecker,[4] Jeanette Eresch,[5] Yifang Mao,[6] Marion Bähr,[7] Dieter Weichenhan,[7] Julio Cordero,[8] Janina Wittig,[1,2] Boran Zhang,[1] Hanyu Cui,[3,9] Xiaoming Li,[3] James A. Oo,[10] Andreas Weigert,[11,12] Mauro Siragusa,[2] Stephan Klatt,[2] Ingrid Fleming,[2,13] Stefan Günther,[13,14] Mario Looso,[13,14] Ralf P. Brandes,[10,13] Harald F. Langer,[13,15,16,17] Andreas Papapetropoulos,[18,19] Mahak Singhal,[6,15] Marcel H. Schulz,[4,13] Christoph Plass,[7] Joerg Heineke,[5,15] Gergana Dobreva,[8,13,15] Jiong Hu,[2,3] and Sofia-Iris Bibli[1,13,15,21,*]

[1]European Center for Angioscience, Department of Vascular Dysfunction, Medical Faculty Mannheim, Heidelberg University, Mannheim, Germany
[2]Goethe University Frankfurt, Institute for Vascular Signalling, Centre for Molecular Medicine, Frankfurt, Germany
[3]Department of Histology and Embryology and Sino-German Laboratory of CardioPulmonary Science, School of Basic Medicine, Tongji Medical College, Huazhong University of Science and Technology, Wuhan, China
[4]Goethe University Frankfurt, Institute for Computational Genomic Medicine, Frankfurt, Germany
[5]European Center for Angioscience, Department of Cardiovascular Physiology, Medical Faculty Mannheim, Heidelberg University, Mannheim, Germany
[6]European Center for Angioscience, Medical Faculty Mannheim, Heidelberg University, Mannheim, Germany
[7]Division of Cancer Epigenomics, German Cancer Research Center, Heidelberg, Germany
[8]European Center for Angioscience, Department of Cardiovascular Genomics and Epigenomics, Medical Faculty Mannheim, Heidelberg University, Mannheim, Germany
[9]Department of Cardiology, The First Affiliated Hospital of Henan University, School of Medicine, Henan University, Kaifeng, China
[10]Goethe University Frankfurt, Institute for Cardiovascular Physiology, Centre for Molecular Medicine, Frankfurt, Germany
[11]Goethe University Frankfurt, Institute of Biochemistry I, Faculty of Medicine, Frankfurt, Germany
[12]Department of Immunity of Inflammation, Institute for Innate Immunoscience (MI3), Medical Faculty Mannheim, Heidelberg University, Mannheim, Germany
[13]German Centre for Cardiovascular Research (DZHK), Berlin, Germany
[14]Cardio-Pulmonary Institute (CPI) Bioinformatics and Deep Sequencing Platform, Max Planck Institute for Heart and Lung Research, Bad Nauheim, Germany
[15]Helmholtz-Institute for Translational AngioCardioScience (HI-TAC) of the Max Delbrück Center for Molecular Medicine in the Helmholtz Association (MDC), Heidelberg University, Heidelberg, Germany
[16]Cardiology, Angiology, Haemostaseology, and Medical Intensive Care, Medical Centre Mannheim, Medical Faculty Mannheim, Heidelberg University, Mannheim, Germany
[17]Cardiovascular Systems Biology, Medical Centre Mannheim, Medical Faculty Mannheim, Heidelberg University, Mannheim, Germany
[18]Clinical, Experimental Surgery and Translational Research Center, Biomedical Research Foundation of the Academy of Athens, Athens, Greece
[19]Laboratory of Pharmacology, Faculty of Pharmacy, National and Kapodistrian University of Athens, Athens, Greece
[20]These authors contributed equally
[21]Lead contact
*Correspondence: iris.bibli@medma.uni-heidelberg.de
https://doi.org/10.1016/j.cmet.2025.10.003

SUMMARY

Endothelial metabolism underpins tissue regeneration, health, and longevity. We uncover a nuclear oxidative catabolic pathway linking cystine to gene regulation. Cells preparing to proliferate upregulate the SLC7A11 transporter to import cystine, which is oxidatively catabolized by cystathionine-γ-lyase (CSE) in the nucleus. This generates acetyl units via pyruvate dehydrogenase, driving site-specific histone H3 acetylation and chromatin remodeling that sustain endothelial transcription and proliferation. Combined loss of SLC7A11 and CSE abolishes cystine oxidative and reductive metabolism and causes embryonic lethality, whereas single deletions reveal distinct effects. SLC7A11 deficiency triggers compensatory cysteine *de novo* biosynthesis, partially maintaining angiogenesis, while CSE deletion disrupts nuclear cystine oxidative catabolism, transcription, and vessel formation. Therapeutically, cystine supplementation promotes vascular repair in retinopathy of prematurity, myocardial infarction, and injury in aging. These findings establish the role of

cystine nuclear oxidative catabolism as a fundamental metabolic axis coupling nutrient utilization to gene regulation, with implications for vascular regeneration.

INTRODUCTION

Vascular endothelial cells are vital instructive gatekeepers of organismal resilience, health, and lifespan.[1] Preserving their function delays age-related pathologies[2–5] and holds promise in regeneration.[6] Their homeostasis and growth rely on precise metabolic wiring,[7,8] with glycolysis and fatty acid oxidation driving vessel sprouting alongside growth factor signaling.[9,10] These findings are particularly relevant given the limited success of growth factor-centric angiogenesis therapies.[11] Beyond energy production, metabolites serve as building blocks for proteins and DNA/RNA and regulate protein modification and chromatin structure.[12,13] In particular, carbon sources communicate with histone marks, modulating gene activity[14] by altering interactions between DNA and nucleosomes.[15–19]

Although gene transcription is regulated by the epigenetic status,[16] how such changes regulate endothelial genes in angiogenesis—and their role in regenerative responses—remains unknown. While some studies exist on histone methylation and acetylation,[20–26] which is enriched over active genes and transcriptional co-regulators[22] *in vitro* and *in vivo*,[26] remains understudied in the vasculature. Notably, nutrient-independent histone acetylation (deacetylate function) has recently been described in maintaining vascular integrity[27,28] and angiogenic phenotypes.[29,30] However, whether and how the proliferating endothelium selectively modulates metabolite levels to regulate nutrient-responsive acetylation of histones and modify transcription during vessel formation remains unclear.

To address this, we profiled endothelial metabolism across cell-cycle states and found that solute carrier transporter (SLC) translation is cycle dependent. Cystine import via SLC7A11 precedes cell division and undergoes unexpected nuclear oxidative catabolism, fueling nuclear acetyl-CoA pools. Cystine also bridges metabolic enzymes and histone acetyltransferases, selectively acetylating H3 lysines, reorganizing chromatin, and activating endothelial transcriptional programs for proliferation and vessel growth. This pathway is unique to young tissues and declines with age, and cystine supplementation restores vascular repair in both young and aged conditions.

RESULTS

Metabolite import precedes endothelial proliferation

Initially, we reasoned that prior to G2/M entry, endothelial cells adjust protein translation and nutrient import to prepare for proliferation. To test this, we transduced human umbilical vein endothelial cells with an FUCCI lentivirus for live cell-cycle imaging. Cells were kept in contact inhibition for 10 days to induce quiescence,[31] then re-plated at low density to trigger proliferation (Figure S1A). Indeed, cells in contact inhibition were arrested at G0 (Figure S1B) and entered the G1 phase at 2 h and the S/G2/M phase by 12–24 h (Figures S1B and S1C) after adhesion (Figure S1D), without marked changes in the phosphorylation of the ribosomal protein S6 (Figure S1E). Next, we analyzed ribosomal occupancy using the RiboTag approach before (2 and 6 h) and during (12 and 24 h) S/G2/M entry, compared with quiescent G0 endothelium (0 h) (Figure 1A). Global translation shifted prior to and throughout cycling (Figure 1B). Loss of contacts induced translation of 868 mRNAs after 2 h, peaking at 12 h, while 1,261 mRNAs were repressed at 2 h, dropping gradually from 12 h (Figure 1B; Table S1_1). Interestingly, endothelial cells exhibited only an 18.3% overlap in ribosome-enriched mRNAs among the different time points (Figure S1F), indicating a temporal dynamic alteration of active-translation as they exit G0 and progress through the cell cycle (Figure S1G). Within 2 and 6 h after adhesion 38.6% of mRNAs were similar (Figure 1C), while cells entering the S/G2/M phase (12 h) and actively cycling (24 h) shared a 61% similarity (Figure 1D). Enrichment analysis revealed reduced translation of transcripts involved in angiogenesis, NOTCH, PDGF, and WNT signaling pathways, prior to S/G2/M entry (Figures 1E and 1F). In contrast, at 2 h post-adhesion, mRNAs related to BMP, TGF-β, and VEGF signaling were enriched (Figure 1E), followed by small molecules, ions, and amino acid transport mRNAs at 6 h and prior to the S/G2/M entry (Figure 1F). Upon entry into S/G2/M (12 and 24 h), mRNAs within the ribosome shifted toward cell-cycle and mitotic processes (Figures 1G and 1H). Temporal regulation of nutrient sensing was indicated by altered mRNA levels of solute carrier transporters (SLCs), particularly within 6 h after adhesion (Figures 1I–1L), involved in multiple processes such as amino acid, ion, nucleoside , and vitamin transport (Figure S1H), while the majority of the total RNA levels remained unchanged (Table S1_2). These data indicate that pre-proliferative endothelial cells prioritize translation over transcription of the SLCs and potentially import specific nutrients to prepare for division.

Unexpectedly, no differences were detected in glucose and mitochondrial related transporters or metabolism in the events preceding cell-cycle entry (Table S1_1; Figure 1M), indicating that nutrients other than glucose are required for early endothelial cell proliferation events. Indeed, metabolomic analysis during the G0 to G1 transition (0 vs. 2 h post-adhesion) showed early alterations of key amino acids, with cystine import and catabolism being among the most significant (Figure 1M), in line with the changes of the respective transporters, i.e., SLC3A2 and SLC7A11[32] (Figures 1I–1L). SLC7A11 mRNA and protein as well as intracellular cystine levels were enriched in 2 and 6 h after adhesion and dropped during actual cell division but always remained high compared with the quiescent conditions (0 h) (Figures 1N–1O). FUCCI-based analysis showed higher SLC7A11 surface expression in proliferating (24 h, G2/M, hGeminin-mAG$^+$) than in quiescent (0 h, G0, hCdt1-mCherry$^+$) cells (Figures S1I and S1J). The *in vitro* findings were reproduced in CD144$^+$ endothelial cells isolated from postnatal day (P) 6 murine retinas from FUCCI mice (Figure 1P). Targeted metabolomics in actively cycling endothelial cells from the murine retina *in vivo* also confirmed the higher levels of cystine and cysteine compared with the quiescence cells (Figure 1Q), supporting a

CellPress
OPEN ACCESS

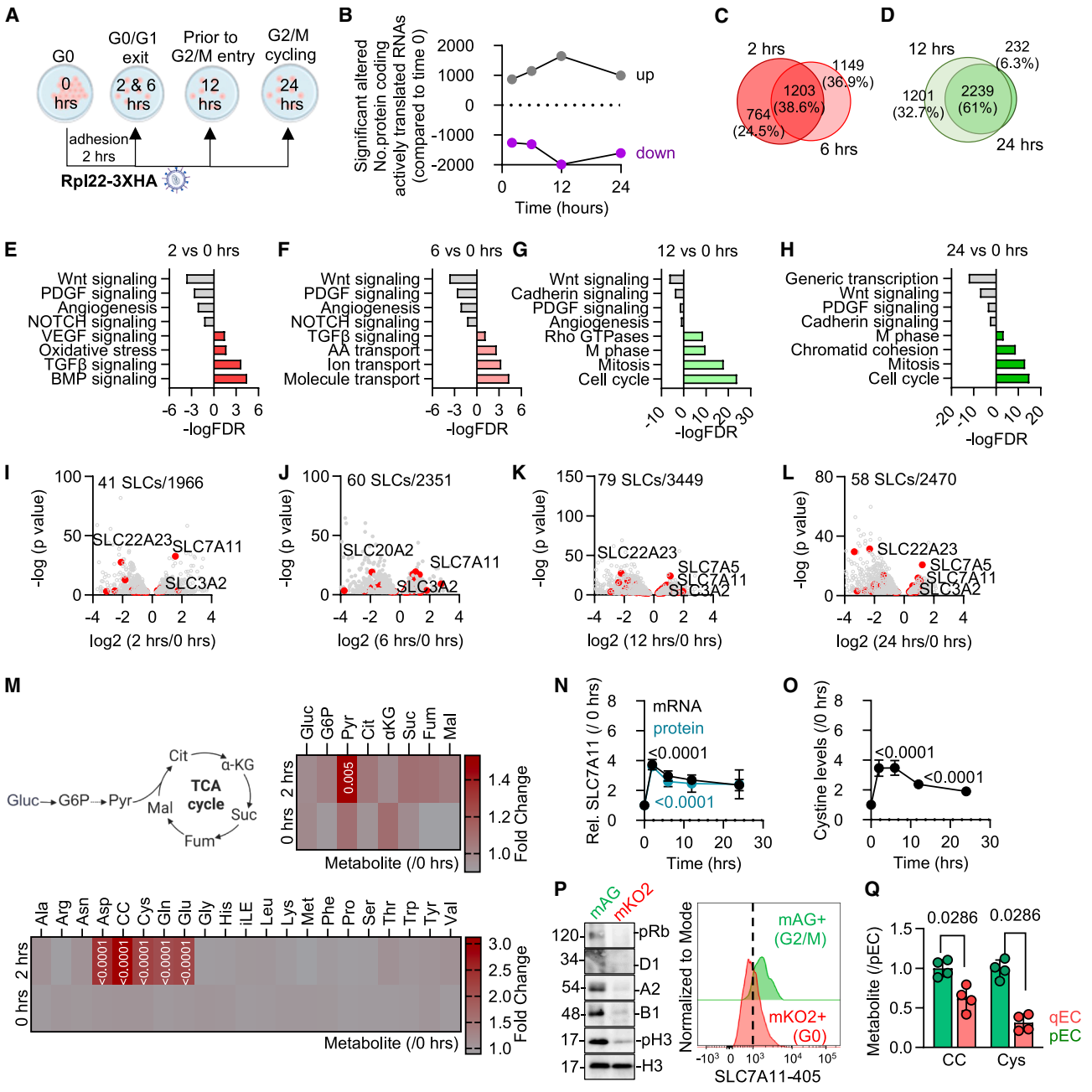

Figure 1. Translation of SLC7A11 and cystine import precede endothelial cell-cycle entry

Human umbilical vein endothelial cells (HUVECs) were maintained in contact inhibition for 10 days (0 h) or seeded after 10 days in low density to initiate the cell cycle.

(A) Experimental setup of cells infected with an Rpl22 lentivirus.

(B) Number of differentially detected mRNAs (log2FC [fold change] ≥ |0.25|).

(C and D) Venn diagrams showing overlapping mRNAs between (C) 2 and 6 h or (D) 12 and 24 h.

(E–H) Pathway enrichment analysis of up- and downregulated mRNAs.

(I–L) Volcano plots showing log_2FC mRNAs.

(M) Heatmaps showing metabolite levels (FC/0 h) detected at 0 and 2 h.

(N) Relative SLC7A11 mRNA and protein levels.

(O) Cystine levels.

(P) Phosphorylated (p) Rb at Ser807/811 (pRb), cyclin D1, cyclin A2, cyclin B1, pH3, and H3 and flow cytometry showing SLC7A11 surface expression in hGem-mAG (mAG+, G_2/M) and hCdt1-mKO2 (mKO2+, G_0) murine retinal endothelial cells ($CD144^+$) from postnatal day 6 (P6).

(Q) Cystine (CC) and cysteine (Cys) levels identified by targeted metabolomics in proliferative (pEC) or quiescent (qEC) P6 retinal endothelial cells.

n = 3–6 biological replicates and 1–2 technical replicates. Mann-Whitney (M and Q) and two-way ANOVA with Tukey's post-test (N).

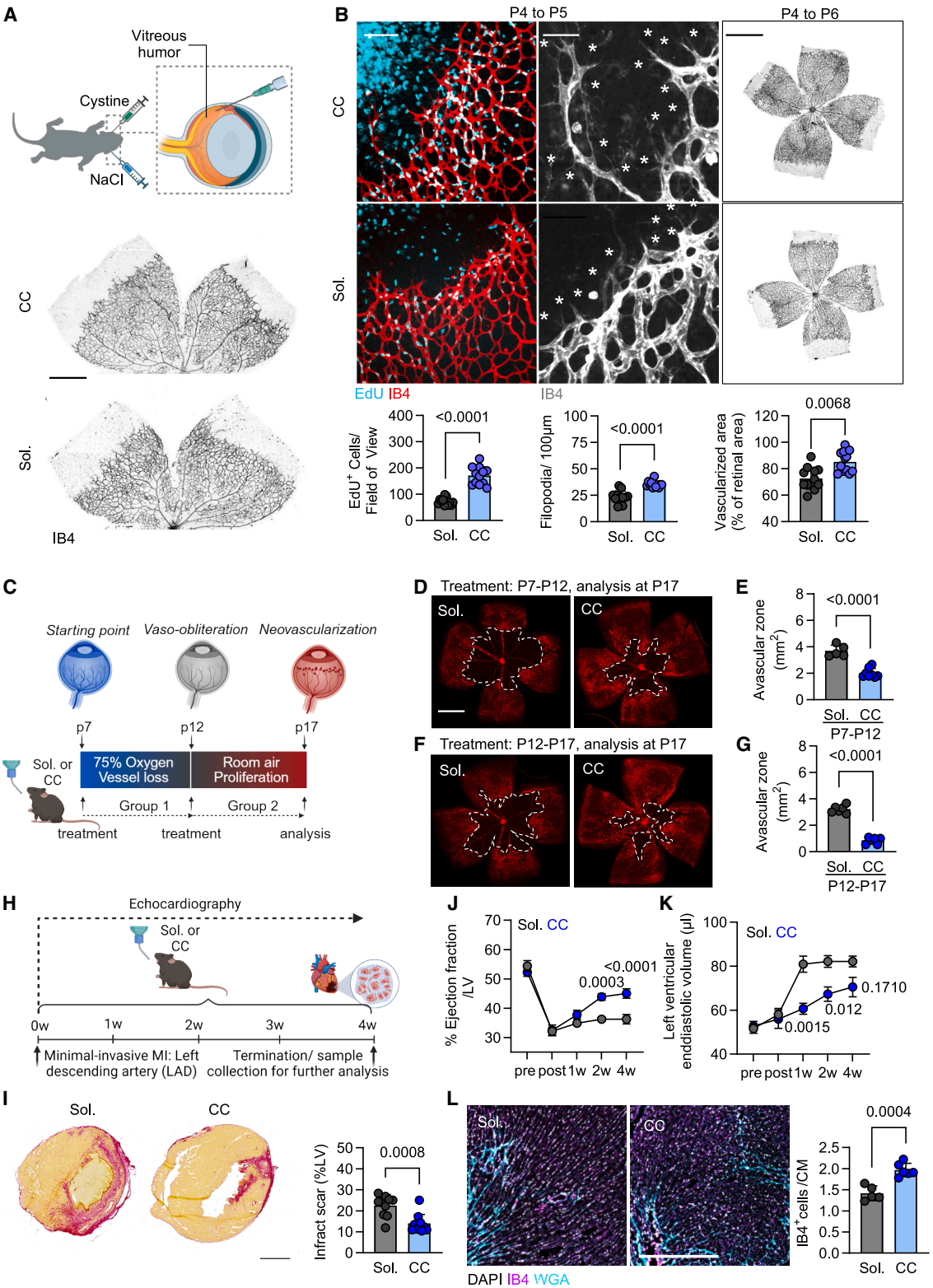

Figure 2. Cystine supplementation promotes vascular growth and repair after injury

(A) P4 murine pups were injected intravitreally with cystine (1 mmol/L) or NaCl in the contralateral eye; representative IB4 images of vascular endothelium (gray) from whole mounts at P5 (scale bar, 500 μm).

(legend continued on next page)

potential link between SLC7A11 and cystine import and catabolism in pre-proliferative endothelial cells.

Cystine supplementation promotes endothelial cell proliferation and reparative responses

Next, we examined cystine's role in endothelial cell-cycle entry (Figure S2A). Depletion of cystine and cysteine arrested cells at G0 (Figures S2B–S2E), while cystine supplementation re-established cell-cycle entry (Figures S2C–S2E). Similar results, albeit to a lesser extent, were observed after treating proliferating endothelial cells, grown in media containing cystine and cysteine, with a selective, potent, and metabolically stable inhibitor of the SLC7A11 transporter (imidazole ketone erastin, IKE)[33] (Figures S2F–S2I). Cyst(e)ine was necessary for the preservation of active ribosomal function, as indicated by the reduced levels of phosphorylation of the ribosomal protein S6 (a readout of active mTOR signaling and protein translation[34,35]) in cells cultured in its absence (Figure S2J) or following selective inhibition of the SLC7A11 (Figure S2K). Removal of cyst(e)ine (Figure S2L) or pharmacological inhibition of the SLC7A11 (Figure S2M) did not initiate apoptotic cell death, nor did it increase lipid peroxidation (Figure S2N), a marker of ferroptosis,[36] in line with reports that blood endothelial cells are resistant to ferroptosis.[37] Phenotypically, not only proliferation but also the ability of endothelial cells to sprout, indicative of the capacity of endothelial cells to acquire a tip cell identity,[38] was sensitive to cystine (Figures S2O and S2P). These findings were also replicated *ex vivo* in aortic ring sprouting assays (Figures S2Q and S2R). *In vivo*, intravitreal injection of cystine in wild-type mice at P4 increased the proliferation of the endothelium at P5, indicated by increased EdU incorporation, resulting in increased vascular growth and filopodia at P6 (Figures 2A and 2B). Exposure of wild-type mice to hyperoxia (from P7 to P12) and subsequent return to room air (from P12 to P17) (Figure 2C) following cystine supplementation resulted in reduced vaso-obliteration (Figures 2D–2G) as well as reduction of the avascular zone (Figures 2E and 2G), indicating a beneficial role of oral cystine in retinopathy of prematurity. To extend the therapeutic potential of cystine supplementation in neovascularization after injury, we also used a minimally invasive acute myocardial infarction model.[39] Addition of cystine 1 day prior and through a 4-week window post-surgery (Figure 2H) reduced infarct scar size (Figure 2I), improved ejection fraction (Figure 2J) and left ventricular end-diastolic volume (Figure 2K), and increased vascularization (Figure 2L) within the infarcted area. Taken together, these data demonstrate cystine's potential in promoting endothelial cell proliferation and vascular repair post-injury.

Cystine oxidative catabolism prior to G2/M entry selectively supports pyruvate generation and is indispensable for vascular growth

Next, we examined the metabolic fate of cystine and its catabolic products to understand its physiological relevance in pre-proliferating endothelial cells. Following import into the cells, cystine is reduced and generates two cysteine molecules. Cysteine can also be *de novo* biosynthesized by methionine/homocysteine through cystathionine-beta synthase (CBS), when the generated cystathionine is converted to cysteine by cystathionine-gamma lyase (CSE).[40] The generated cysteine further supports protein synthesis[41] or metabolically rewires to multiple pathways including glutathione biogenesis,[42] thiosulfate biogenesis,[43] CoA,[44] and taurine[45] biosynthesis, or is further catabolized by CSE to generate downstream metabolic intermediates, a process primarily characterized in eukaryotic cells[46] (Figure 3A).

To profile cystine metabolic flux, we performed isotope-tracing experiments with stable ^{13}C- or ^{34}S-labeled cystine (Figure 3A) in quiescent cells (0 h) versus cells high in SLC7A11 expression, exiting the G0 state (2 h) (Figure 3B). We found a significant increase of cystine uptake and almost 100% intracellular cystine labeling in cells exiting the G0 state, with approximately 70% of it supporting cysteine levels (Figure 3C), suggesting cystine import regulates the majority of the reductive cysteine biosynthesis in pre-proliferating endothelial cells. Although one of the glutathione biosynthesis enzymes was slightly reduced when cells were exiting the G0 state (Figure 3D), ^{13}C-cystine-derived glutathione levels were not altered in the two studied groups (Figure 3E; reaction 1, Figure 3A), indicative of the importance of cystine-reductive catabolism to maintain redox surveillance in the endothelium. ^{34}S-cystine tracing showed minimum incorporation to the 3-mercaptopyruvate (3MP) and thiosulfate products in non-quiescent cells compared with that in quiescent non-cycling endothelial cells (Figure 3F; reaction 2, Figure 3A), potentially resulting from the reduced 3-mercaptosulfurtransferase (MPST) translation (Figure 3G). In addition, glutamic-oxaloacetic transaminases/GOTs primarily utilize aspartate instead of cysteine, which was increased 2-fold in non-quiescent endothelial cells (Figure 3H). Although no significant differences were detected in the enzymes responsible for the addition of cysteine to CoA (Figure 3I), an approximate 50% reduction in the incorporation to CoA from ^{34}S-cystine was observed in non-quiescent cells (Figure 3J; reaction 3, Figure 3A). Similarly, despite the fact that the levels of the two key taurine biosynthetic enzymes were not altered (Figure 3K), a significant reduction in ^{34}S-cystine flux to taurine was observed in non-quiescent cells (Figure 3L; reaction 4, Figure 3A). Last, we evaluated the contribution of cystine to

(B) Immunofluorescent images and quantification of EdU$^+$ cells/field, filopodia/100 μm perimeter, and vascularized area at P5 (left) and P6 (right) retinas (scale bars, 100, 50, and 500 μm, respectively). EdU, cyan; IB4, red/gray.
(C) Schematic showing the retinopathy of prematurity (ROP) model and the respective treatment with solvent (Sol.) or 100 mg/kg/day cystine (CC) in the maternal drinking water.
(D–G) Immunofluorescent images of IB4 and quantification of avascular zone (white lines) (scale bar, 500 μm).
(H) Schematic showing the minimally invasive myocardial infarction model and the follow-up echocardiographic monitoring in mice receiving either solvent (Sol.) or 50 mg/kg/day cystine (CC) in the drinking water 1 day prior and up to 4 weeks post-surgery.
(I) Sirius red fibrosis staining and quantification of the infarct scar (scale bar, 1,000 μm).
(J and K) Echocardiographic analysis of the (J) ejection fraction and (K) left ventricular end diastolic volume.
(L) Immunofluorescent images of DAPI (gray), IB4 (magenta), and wheat germ agglutinin (WGA, cyan) (scale bar, 500 μm).
n = 5–12 biological replicates. Paired (A and B) and unpaired (D–G and I–L) Student's t test.

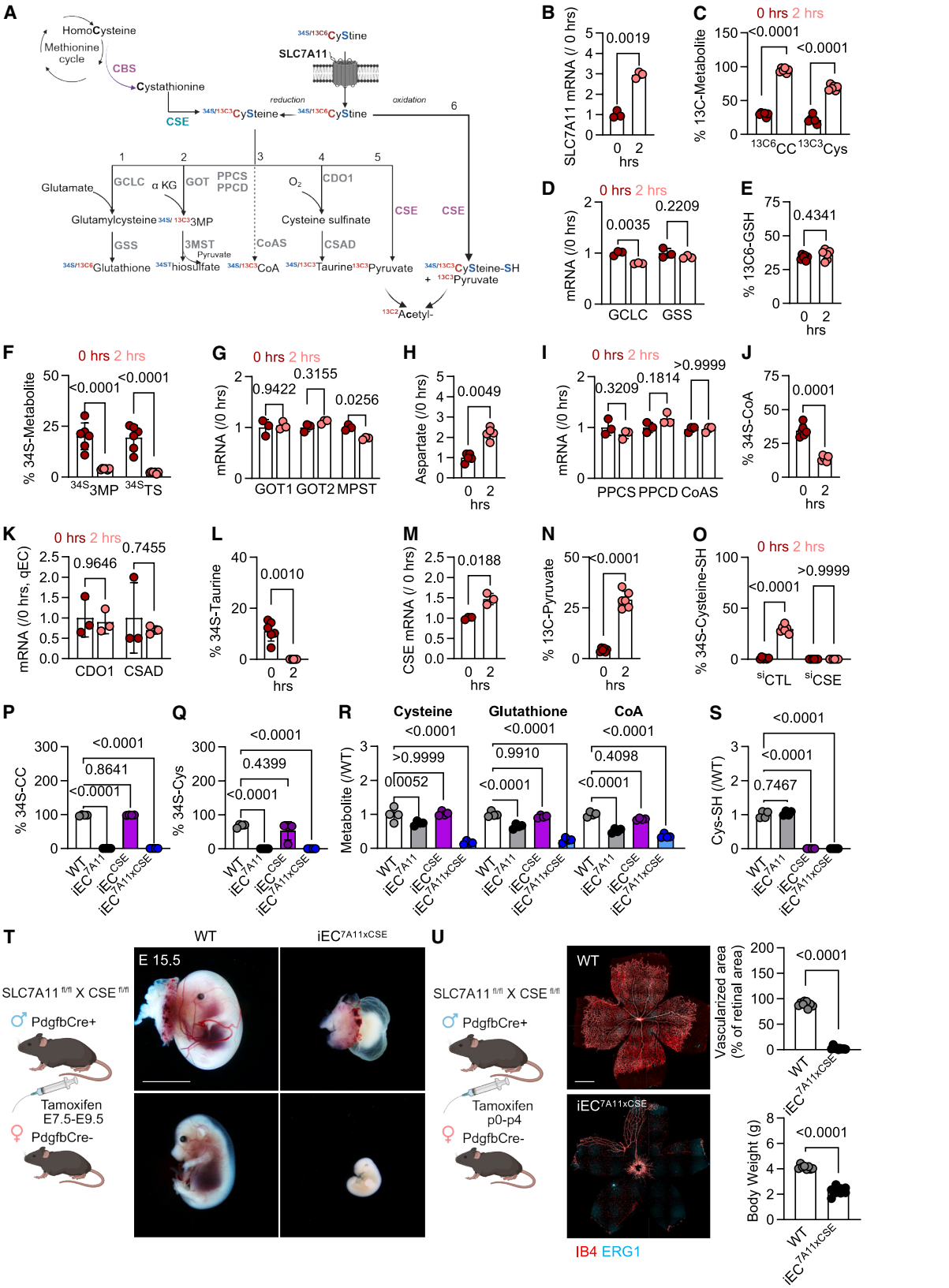

(legend on next page)

generate pyruvate. Such a metabolic flux can be regulated by the enzymatic activity of CSE through oxidative catabolism (reaction 6, Figure 3A), either directly by using cystine as a substrate or indirectly using cysteine instead (reaction 5, Figure 3A). In any case, CSE translation was increased in non-quiescent cells (Figure 3M), and a marked incorporation of carbons from cystine to pyruvate was detected (Figure 3N; reactions 5 and 6, Figure 3A). ^{34}S-cystine tracing confirmed that approximately 30% of cystine fluxes to cysteine persulfide (SH) exclusively in non-quiescent conditions, and CSE silencing halts such metabolic flux (Figure 3O). These data indicate a clear substrate preference and oxidative cystine catabolism by the CSE enzyme in non-quiescent conditions, a pathway that was recently reported in cancer cells.[47] Oxidative metabolism of cystine was evident not only within the first hours after the loss of quiescence but also in the actively proliferating endothelial cells (24 h). These cells preferentially support the reductive biosynthesis of glutathione and oxidative biosynthesis of pyruvate from cystine and do not favor pyruvate biosynthesis through the MPST enzyme, nor do they significantly support CoA or taurine biogenesis (Figure S3A). Genetic deletion of *Slc7a11* and dual genetic deletion of *Slc7a11* and *C*th (gene name for CSE) resulted in a complete loss of cystine import (Figure 3P) and cystine-derived cysteine in cultured proliferating cells (Figure 3Q). Cystine-derived intracellular cysteine in the CSE-deleted endothelium was similar to the wild-type endothelium (Figure 3Q). Unexpectedly, loss of the cystine transporter only partially affected the total intracellular cysteine levels and partially maintained the key metabolites of the reductive pathway (i.e., glutathione and CoA) similar to the single deletion of the CSE, while dual deletion of SLC7A11 and CSE collapsed both the reductive and the oxidative pathways (Figure 3R). The cystine oxidative metabolic flux was solely attributed to the CSE enzyme, as deletion of the gene resulted in undetectable cysteine-SH, which was preserved in the absence of the SLC7A11 (Figure 3S). Phenotypically, endothelial cells isolated from the SLC7A11/CSE double-knockout mice, with a complete loss of the reductive and oxidative cystine catabolism, did not proliferate (confluence fold change at 48 h = ~1) compared with the individual single-knockout endothelial cells (Figure S3B), lost their sprouting capacity (Figure S3C), and reduced activation of the ribosomal subunits, as indicated by the phosphorylation of the ribosomal protein S6 (Figure S3D). The loss of the proliferative and sprouting capacity in SLC7A11 or/and CSE-depleted endothelial cells was not due to increased apoptosis, as shown by annexin V signals (Figure S3E). *In vitro*, genetic ablation of CSE inhibited the proliferation of murine lung microvascular endothelial cells, an effect that was reversed by adenoviral-mediated overexpression of CSE (Figures S3F and S3G). Competition assays in which CSE-depleted cells were labeled with an RFP track empty adenovirus or with a GFP track CSE adenovirus showed that only GFP/CSE-positive cells sprout in a 3D culture system (Figure S3H). *Ex vivo* aortas from mice lacking CSE also showed reduced endothelial sprouting (Figure S3I). To evaluate the impact of simultaneous loss of the reductive and oxidative cystine metabolism in vascular growth, we crossed the *Slc7a11*$^{fl/fl}$ and CSE$^{fl/fl}$ mice with mice expressing the inducible Cre recombinase under the control of the *Pdgfb* promoter. Endothelial inducible deletion of both SLC7A11 and CSE at embryonic day (E)7.5 resulted in embryonic lethality and complete loss of vascular growth at E15.5 (Figure 3T). Such results were replicated in the postnatal murine retina model, in which inducible deletion of both genes from P0 to P4 resulted in restricted pup growth and attenuation of retinal vascularization at P6 (Figure 3U).

Distinct roles of SLC7A11 and CSE in pyruvate biosynthesis and vascular growth

Next, we attempted to delineate the impact of the cystine import and oxidative, but not reductive, catabolism in vascular growth. In line with the *in vitro* observations, developing endothelial cells at P6 with a genetic deletion of *Slc7a11* lost the capacity to import cystine, in contrast to the CSE-deleted or wild-type cells (Figure 4A). Retinal endothelial cells also showed reduced total intracellular cysteine, cysteine persulfide, and pyruvate levels in the absence of the SLC7A11 (Figure 4B), in contrast to the deletion of CSE, which resulted in a collapse of the oxidative pathway (Figure 4C). These data imply that in absence of the SCL7A11, the endothelium responds by increasing cysteine *de novo* biosynthetic pathways (Figure 4D).[40] As CBS is not expressed in endothelial cells,[40] we reasoned that when cystine import is halted, CSE alters its substrate preference to utilize homocysteine and cystathionine for supporting cysteine biosynthesis and further cysteine flux to glutathione

Figure 3. Pre-proliferating endothelial cells import and utilize cystine to support pyruvate generation

(A) Schematic presentation of the reductive and oxidative cyst(e)ine metabolism. GCLC, glutamate-cysteine ligase; GSS, glutathione synthetase; GOT, aspartate aminotransferase; 3MST, 3-mercaptopyruvatesulfurtransferase; PPCS, phosphopantothenate-cysteine ligase; PPCD, phosphopantothenoylcysteine decarboxylase; CoAS, coenzyme synthetase; CDO1, cysteine deoxygenase; CSAD, cysteine-sulfinic acid decarboxylase; CSE, cystathionine-gamma lyase; CBS, cystathionine-beta synthase; α-KG, alpha-ketoglutarate; 3MP, 3-mercaptopyruvate; cystine-SH, cysteine persulfide.

(B, D, G, I, K, and M) Relative levels of ribosome-enriched mRNAs involved in the cystine metabolism at 0 and 2 h after adhesion.

(C, E, and N) Percentage of ^{13}C incorporation from uniformly labeled cystine to (C) intracellular cystine and cysteine, (E) glutathione (GSH), or (N) pyruvate at 0 and 2 h after adhesion.

(F, J, L, and O) Percentage of ^{34}S incorporation from uniformly labeled cystine to (F) 3MP, thiosulfate (TS), (J) coenzyme A (CoA), (L) taurine, and (O) cysteine-SH at 0 and 2 h after adhesion. (O) Cells were transduced with a control siRNA (^{si}CTL) or with an siRNA directed against CSE (^{si}CSE).

(H) Relative aspartate levels at 0 and 2 h after adhesion.

(P, Q, and S) Percentage of ^{34}S incorporation from uniformly labeled cystine to (P) intracellular cysteine, (Q) cysteine, and (S) cysteine persulfide in cultured endothelial cells isolated from wild type (WT) or littermates with induced deletion of SLC7A11 and/or CSE.

(R) Levels of intracellular cysteine, glutathione, and CoA in samples as in (P).

(T) Stereomicrographic images of E15.5 embryos in Pdgfb Cre− (WT) and Cre+ (iEC^{SLC7A11xCSE}) mice treated with tamoxifen from E7.5 to E9.5.

(U) Immunofluorescent images of IB4 (red) and ERG1 (cyan) staining and quantification of vascularized area and body weight at P6 in Pdgfb Cre− (WT) and Cre+ (iEC^{SLC7A11xCSE}) mice treated with tamoxifen from P0 to P4.

n = 3–9 biological replicates and 1–2 technical replicates. Mann-Whitney (B, D, G–I, K, and M), paired Student's *t* test (C, E, F, J, L, and N–P), and one-way ANOVA with Dunnett's test (Q–S).

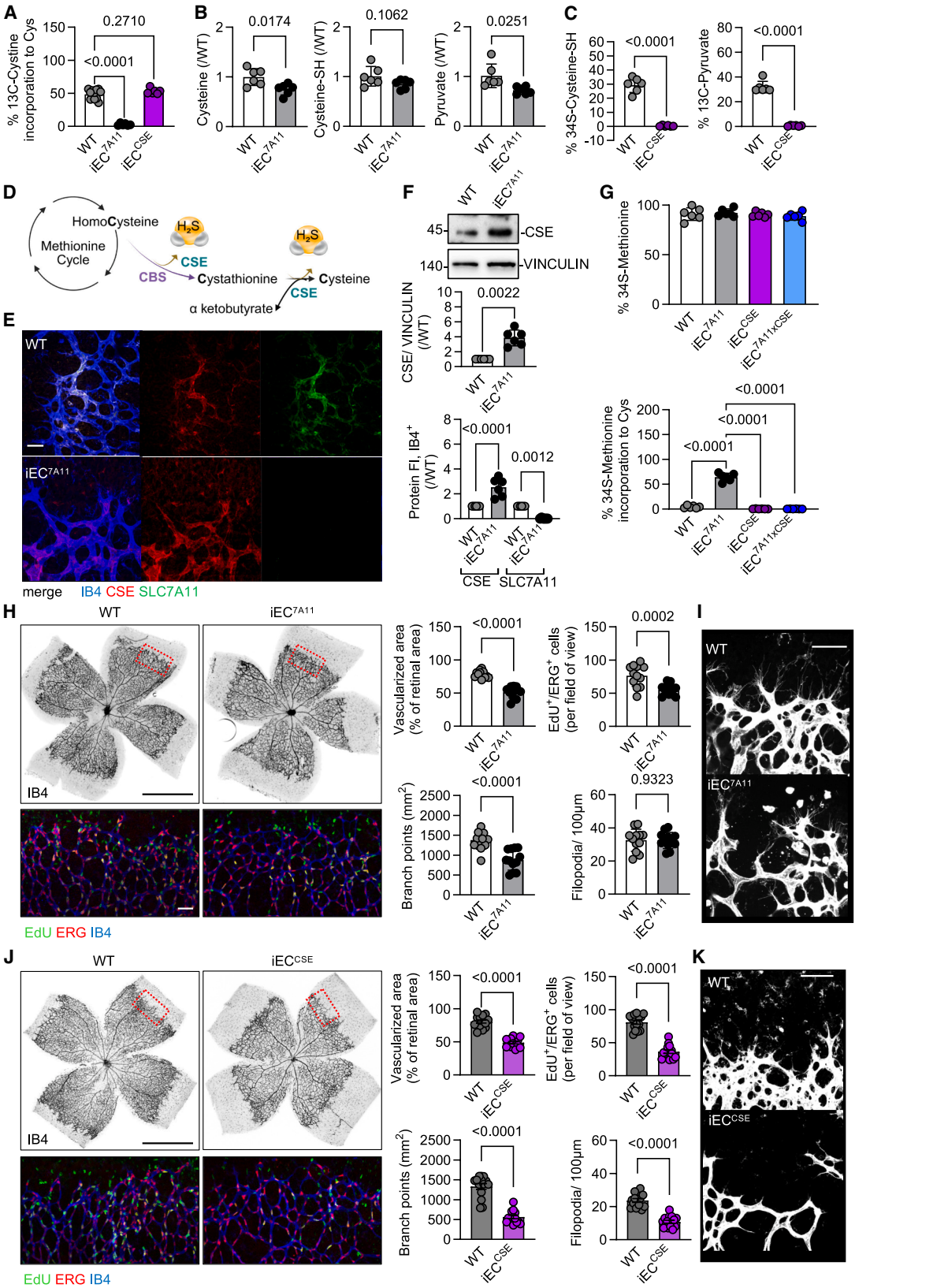

(legend on next page)

and pyruvate. Indeed, it has been proposed that CSE can serve as an alternative enzyme for homocysteine catabolism.[48] CSE expression was even potentiated following *Slc7a11* transient deletion (Figures 4E and 4F), and ^{34}S-methionine tracing showed a >50% increase in the incorporation of ^{34}S-to cysteine in SLC7A11-depleted endothelial cells compared with endothelial cells from wild type (Figure 4G), while double SLC7A11/CSE deletion reduced the methionine-derived cysteine levels (Figure 4G), strengthening the hypothesis that cysteine levels in the absence of cystine import are supported by CSE-mediated *de novo* biosynthesis of cysteine from methionine.

How does SLC7A11 deletion increase CSE expression to preserve cysteine biosynthesis? Cystine depletion from the growth media increased phosphorylation of the eukaryotic initiation factor-2α (eIF2α) on Ser51 (Figures S4A–S4D) , in line with an integrated stress response (IRS) activation,[49] which can regulate SLC7A11[50] and CSE through ATF4.[51,52] Indeed, inhibition of the general control non-derepressible (GCN) 2 (the kinase responsible for phosphorylation of eIF2a) in the absence of cyst(e)ine metabolites made the cells unable to upregulate SLC7A11 and CSE (Figure S4E). Taken together, these data propose that in response to cystine depletion/SLC7A11 absence, CSE increase in response to IRS goes hand in hand with a substrate preference switch, which is responsible for maintaining cysteine biogenesis and supporting both the reductive and oxidative pathways, suggesting a non-linear parallel metabolic pathway involving CSE.

In line with the partial reduction of the reductive cystine catabolic pathway, inducing the deletion of *Slc7a11* between P1 and P4 resulted in mild phenotypes at P6, with reduced vascular growth, proliferation, and branching/complexity of the retinal vasculature (Figure 4H). However, no significant difference was observed in the filopodia formation (Figure 4I), indicating that loss of SLC7A11 does not affect the capacity of the endothelial cells to undertake the tip cell identity. In contrast to the impact of SLC7A11 deletion, collapse of the oxidative cystine catabolism through *in vivo* endothelial-specific inducible CSE deletion resulted in reduced retinal angiogenesis, vascular density, proliferation, and filopodia (Figures 4J and 4K).

Cystine oxidative metabolism alters acetyl-CoA availability in the nuclear compartment

How does cystine oxidation support vascular growth? First, we tested whether the pathway's sulfide byproducts influence endothelial proteins via persulfidation.[53] Neither developing (P6) nor quiescent (P15) retinas showed significant global (Figure S4F) or vascular (Figure S4G) differences, and addition of a rapidly releasing H_2S donor had no effect on vascular growth *in vivo* (Figures S4H–S4J), suggesting a minor role for sulfur flux in retinal angiogenesis.

As such, next, we examined the cystine-to-pyruvate pathway's role in acetyl-moiety generation. During proliferation, most acetyl-CoA was derived from glucose, with about 25% acetyl-CoA coming from cystine carbons and only about 3% fluxing from palmitate. In contrast, in quiescent cells, acetyl-CoA from glucose and cystine decreased, while palmitate contribution rose above 30% (Figure 5A). Proliferating P6 retinal endothelial cells showed higher cystine-to-acetyl-CoA flux than quiescent cells, whereas glucose contribution was unchanged (Figure 5B). Despite acetyl-CoA's involvement in multiple metabolic routes (Figure 5C),[54] cystine carbons did not contribute to the metabolites within the TCA cycle, nor did they support ketogenesis, lipogenesis, or mevalonate biosynthesis (Table S1_3, Figure 5D). Instead, cystine oxidation modestly supported cytosolic, but not mitochondrial, cysteine persulfide, pyruvate, and acetyl-CoA, with a marked enrichment in nuclear acetyl-CoA during proliferation (Figure 5E). Nuclear acetyl-CoA generation would result from the citrate-mediated ACLY pathway, the acetate-related ACCS2 pathway, or the pyruvate-related PDH pathway.[54] Having ruled out the potential cystine-to-citrate contribution (Figure 5D), and given that cystine metabolically cannot flux to acetate, we next interrogated potential mechanisms of a cystine-pyruvate-PDH-dependent nuclear acetyl-CoA biosynthesis. A limited proteolysis mapping proteomic approach[55] (Figure S5A; Table S2) revealed that cystine interacted overall with approximately 10,000 peptides within the proliferating endothelium (Figure S5B). Unique interacting sequences of cystine included GTP binding, RhoGEF, and protein tyrosine kinase domains (Figure S5C) in peptides within the cytoplasm and nuclear compartment (Figure S5D), belonging to proteins involved primarily in the regulation of nucleocytoplasmic transport (i.e., importins KPNA3 or KPNB1, which are responsible for transport proteins with nuclear localization signals), cysteine metabolism (i.e., CSE and GOT1), and pyruvate metabolism (i.e., PKM and PDHX) (Figure S5E). Among those, cystine was found to interact with PDHA1 (Figure S5F; Table S2), and the results were validated using surface plasmon resonance (Figure S5G). Docking analysis[56] showed cystine binding to CSE and PDHA1 residues, with His177 of CSE forming a stabilizing hydrogen bond with cystine, which appears to enhance the proximity and potential interaction between CSE and PDHA1. MDAnalysis[57] indicated that cystine increased CSE-PDHA1-binding

Figure 4. Endothelial deletion of CSE, but not SLC7A11, affects vascular growth

(A) Percentage of ^{13}C-cystine to ^{13}C-cysteine (Cys) in endothelial cells isolated from WT, iEC^{7A11}, iEC^{CSE}, and iEC^{SLC7A11xCSE} retinas at P6.

(B) Levels of intracellular cysteine, cysteine-SH, and pyruvate.

(C) Percentage of ^{34}S and ^{13}C incorporation from uniformly labeled cystine to cysteine-SH and pyruvate.

(D) Schematic presentation of *de novo* cysteine biosynthesis from methionine.

(E) Immunofluorescent images of IB4 (blue) and quantification of fluorescent intensity (FI) of CSE (red) and SLC7A11 (green) from WT and iEC^{7A11} littermates (P6) (scale bar, 50 μm).

(F) SLC7A11 and CSE in samples as in (E).

(G) Percentage of ^{34}S-methionine incorporation into intracellular cysteine in samples as in (A).

(H and J) Immunofluorescent images and quantification of the developing vasculature (IB4, gray and blue), ERG (red), and EdU (green) in (H) WT and iEC^{7A11} and (J) WT and iEC^{CSE} littermates (P6) (scale bar, 500 μm).

(I and K) Immunofluorescent image of the vascular front in samples as in (H) and (J), respectively (scale bar, 250 μm).

n = 6–14 biological replicates. Unpaired (A–C, H, and J) and paired (F and G) Student's t test.

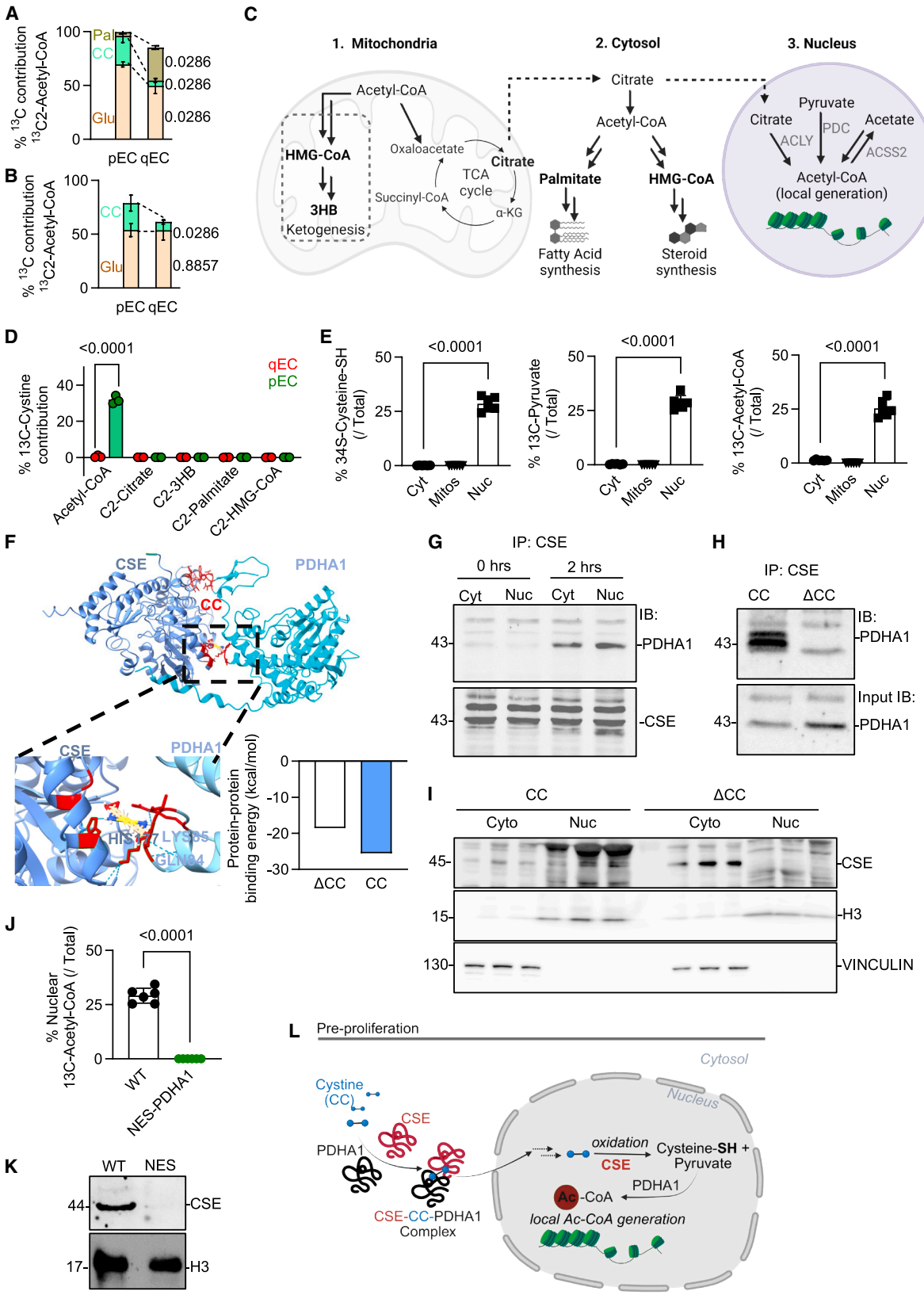

(legend on next page)

affinity from −18.2 to −25.5 kcal/mol (Figure 5F). Indeed, CSE-PDHA1 interactions occurred in nuclear and cytosolic fractions of pre-proliferative, but not quiescent, endothelial cells (Figure 5G) and were cystine dependent (Figure 5H). Given that CSE does not possess any pseudo or typical nuclear localization signal, and CSE also failed to enter the nucleus in the absence of cystine (Figure 5I), we reasoned that cystine scaffolds CSE to PDHA1, which jointly translocate within the nucleus at early stages of endothelial cell proliferation. Overexpression of a nuclear extraction signal (NES)-PDHA1 failed to generate any ^{13}C-cystine-derived acetyl-CoA within the nuclear compartment (Figure 5J) and prevented CSE nuclear entry (Figure 5K). Taken together, these data suggest that cystine oxidative catabolism occurs primarily within the nuclear compartment in pre-proliferating endothelial cells and depends on the availability of cystine and its capacity to initiate the CSE-PDHA1 interactions that translocate together into the nuclear compartment, supporting local acetyl-CoA biosynthesis (Figure 5L).

Cystine-derived acetyl-CoA promotes nutrient-responsive histone acetylation and regulates endothelial transcription

Loss of CSE reduced cystine-derived and global pyruvate/acetyl-CoA levels (Figures 6A and 6B). SILAC proteomics revealed that cystine carbons primarily decorate histone 3 and histone 4 lysines (Figure 6C), with major changes in H3K9ac, H3K23ac, H3K14ac, H3K18ac, H4K5ac, H4K8ac, and H2AK5ac—the most abundant marks in the proliferating endothelium (Figure 6D). Cystine contributed 59.95% to H3K9ac, 77.96% to H3K23ac, and 43.44% to H2AK5ac, while most other marks received <10% contribution, indicating a targeted rather than stochastic incorporation into histone acetylation. This specificity could not be replaced by other carbon sources, as mark abundance was not restored in CSE-deficient cells (Figure 6D). To understand how cystine carbons exerted unique specificity for those histone marks, next, we hypothesized that the CSE-PDHA1 complex, in the presence of cystine, may physically associate with histone acetyltransferases. Indeed, cystine promoted the CSE-PDHA1 interaction with GCN5 and HAT1 (Figure 6E), which are both identified as cystine-binding partners (Table S2) and are responsible for the acetylation of H3 at residues K9, K14, and K23 and H4 at K5, K8, K12, and H2AK5 but would have no impact on H3K27ac or other histone marks. These data indicate that (1) the specific lysine residues are non-stochastically altered from cystine carbons and (2) the epigenetic reprogramming is preceding proliferation.

To assess the impact of cystine-dependent histone acetylation on endothelial gene regulation, we performed ACT sequencing[58] on the most abundant acetylation sites, which correlated positively with chromatin accessibility in proliferating endothelial cells (Figures 6F and 6G; Table S3). We focused on marks with the highest cystine contribution and partial irreplaceability in CSE-deficient cells—H3K9ac and H3K23ac—along with H3K4me3 (cystine-independent and promoter-associated) and H3K27ac (minimally cystine dependent but strongly overlapping accessible chromatin in wild-type cells). CSE loss markedly reduced H3K9ac and H3K23ac (Figure 6H), both of which regulate active transcription and chromatin accessibility,[59] while leaving H3K27ac and H3K4me3 largely unaffected. Notably, neither glucose deprivation (Figure 6I) nor cell-cycle arrest[60] reduced H3K9 and H3K23 acetylation (Figure 6J). CSE deletion and the associated loss of H3 acetylation reduced binding of H3K9ac and H3K23ac (Figure S6A; Table S4) at loci controlling endothelial signaling, angiogenesis, and cell growth (Figures S6B and S6C). ATAC sequencing revealed 7,932 regions with altered accessibility in CSE-deficient cells (Figure 6K; Table S5), and transcription factor footprinting showed decreased accessibility at ETS family motifs, with a pronounced loss of ERG-binding sites (Figure 6L).

Non-permissive chromatin in promoters was found in downregulated genes on the RNA level in CSE-deleted endothelial cells (Figure S6D). Differentially accessible chromatin regions overlapped by 70% with the RNA-seq changes (Figure 6M), and loci enriched in H3K9ac/H3K23ac with accessible chromatin corresponded to genes involved in growth factor signaling and angiogenesis (Figure S6E). Motif analysis of transcription factors potentially binding to enhancers revealed that CSE-depleted cells lose *Etv4* and *Erg* binding and gain *Spi1* binding (Figure 6N), a driver of endothelial-to-mesenchymal transition.[61] As expected, chromatin reorganization resulted in altered endothelial cell transcription in cells lacking CSE (Figure 6O) and a dysregulation of ETS family target genes (Figure 6P; Table S6). Promoters marked by cystine-dependent H3K23ac/H3K9ac were significantly enriched among differentially expressed RNAs, over 50% of which were ETS regulated (Figure S6F). Indeed, endothelial cells lacking CSE showed reduced levels

Figure 5. Cystine oxidative metabolism supports PDH-mediated nuclear acetyl-CoA generation

(A and B) Percentage of ^{13}C-glucose (Glu), ^{13}C-cystine (CC), and ^{13}C-palmitate (Pal) contribution to $^{13}C_2$-acetyl-CoA in (A) human and (B) P6 murine retinal CD144$^+$ proliferating (pEC) and quiescent (qEC) endothelial cells.

(C) Schematic showing the metabolic routes for acetyl-CoA generation and flux in the mitochondria, cytoplasm, and nucleus.

(D) Percentage of ^{13}C-cysteine contribution to acetyl-CoA, citrate, 3-hydroxybutyrate (3HB), palmitate, and HMG-CoA in samples as in (A).

(E) Percentage of ^{13}C-cystine contribution to cysteine-SH, pyruvate, and acetyl-CoA in different cellular fractions (Cyt, cytoplasm; Mitos, mitochondria; Nuc, nuclei) of proliferating human endothelial cells.

(F) Structural models of the CSE-PDHA1 protein complex were generated using AlphaFold 3 and used for docking stimulations using AutoDock. Predicted cystine interaction sites on CSE and PDHA1 (hydrogen bonding) are highlighted.

(G) Pyruvate dehydrogenase E1 subunit alpha 1 (PDHA1) in different cellular fractions after immunoprecipitation (IP) of CSE.

(H) PDHA1 in cells cultured in a cystine/cysteine-depleted media (ΔCC) or in media supplemented with 100 μmol L-cystine (CC) for 24 h, prior to IP of CSE.

(I) CSE in different cellular fractions in samples as in (H).

(J) Percentage of ^{13}C-cystine to nuclear acetyl-CoA in endothelial cells overexpressing an NES-PDHA1 construct.

(K) CSE in cells as in (J).

(L) Graphical abstract summarizing the proposed mechanism of cystine-derived nuclear acetyl-CoA generation.

n = 4–6 biological replicates. Mann-Whitney (A, B, D, and J) and one-way ANOVA with Dunnett's test (E).

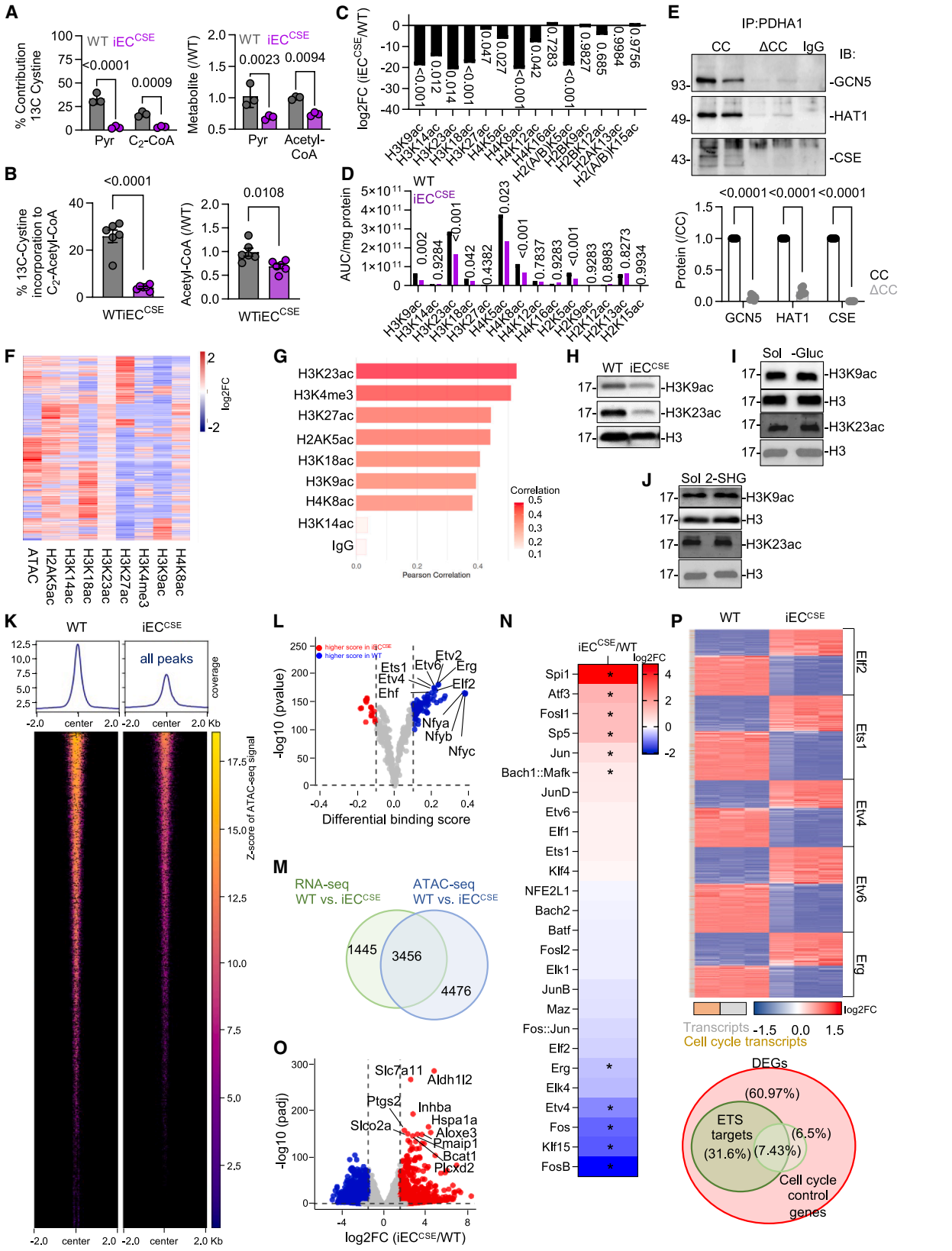

(legend on next page)

of the ERG transcripts[62] *Dll4*, *Hey1*, and *Hes1* (Figure S6G). Notably, 74 of those ETS family targets were cell-cycle transcripts. Collectively, RNA-seq studies showed loss of tip and stalk cell identity markers, as well as reduced endothelial cell fate commitment markers (Figure S6H), alongside upregulation of differentiation genes such as *Vim* (Vimentin) (Figure S6I), which was also validated *in vivo* (Figure S6J). Taken together, our data suggest that cystine/CSE-dependent endothelial cell commitment precedes proliferative responses, and re-establishing cell cycle without appropriate cystine oxidative catabolic flux fails to preserve the transcription of key endothelial cell genes.

Cystine supplementation enhances vascular regeneration in aging

Loss of cystine oxidative flux was a common feature of aged organs (Figures 7A and 7B), whereas rejuvenating strategies, i.e., aortic injury or stimulating the IRS by caloric restriction,[51] boosted cystine oxidative metabolism in the endothelium (Figure 7B). To translate the findings to humans, we analyzed human aged and young endothelial cells[6] (Figure 7C). Although *SLC7A11* transcriptional levels were unchanged (Figure 7D), and CSE (gene name *CTH*) was partially reduced in human aged endothelial cells (Figure 7E), aged cells failed to increase protein levels of SLC7A11 when proliferation was required, in contrast to the respective young cells (Figure 7F). ATF4 overexpression in the aged endothelium was able to restore both SLC7A11 and CSE levels within 24 h of recovery (Figure 7G), re-establishing cystine oxidative flux (Figure 7H) and allowing them to enter the cell cycle (Figure 7I), although to a lesser extent than the double SLC7A11/CSE overexpression (Figure 7I). Targeted metabolomic analysis revealed altered cysteine and methionine metabolism in aged endothelial cells (Figures S7A–S7C), which had reduced cystine oxidative flux compared with the young cells at baseline (Figure 7J), correlating with decreased H3K9ac and H3K23ac marks (Figure 7K). Differentially accessible chromatin and transcriptional identity of the aged endothelium overlapped by 16.9% (Figure 7L) and 19.9% (Figure 7M), respectively, with the CSE-deleted endothelial cells, in regions primarily linked to extracellular matrix deposition and growth factor signaling (Figure 7N). Interestingly, in endothelial cell aging CSE deletion is a strong regulator of the cell-cycle arrest gene, transcriptional factor p53.[6] As such, next, we attempted to release the cell-cycle arrest of endothelial cells lacking CSE and evaluate their identity. Indeed, deleting p53 in CSE-deleted endothelial cells allowed the cells to enter the cell cycle (Figure S7D). However, endothelial cells failed to maintain their transcriptional program as no changes were detected in ETS family target transcripts when both p53 and CSE were absent, compared with cells lacking only CSE (Figure S7E). Given that vascular aging is associated with poor outcomes in vascular repair,[63] we next evaluated whether increased cystine administration could be beneficial to promote endothelial regeneration/re-endothelization upon injury. Circulating aminograms from aged and young patients (cohort as previously published[6]) showed reduced cystine levels in the circulation, albeit higher cystathionine and cysteine levels (Figure 7O), with an overall higher cystine/cysteine ratio in the plasma of young subjects (Figure 7P). Similarly, plasma of young mice showed a higher cystine/cysteine ratio compared with aged mice, which was reversed after oral administration of cystine for 4 consecutive days at 18 months of age (Figure 7Q). By administrating cystine in a mouse model of aortic regeneration at 18 months of age, we were able to enhance vascular regeneration and increase the proliferative capacity of the endothelium approximately four times (Figures 7R and 7S). Taken together, these data suggest that although the oxidative environment is diminishing intracellular cystine levels in aging, administration of cystine can favor endothelial cell proliferation after injury.

DISCUSSION

Here, we report that (1) endothelial cells upregulate translation of SLCs, such as SLC7A11, to increase cystine uptake before cell-cycle entry; (2) cyst(e)ine is indispensable for proliferation; (3) nuclear CSE-driven oxidative catabolism of cystine sustains epigenetic marks and chromatin accessibility for endothelial transcription factors; (4) aging blunts cystine plasma availability and intracellular oxidative metabolism; and (5) cystine supplementation restores endothelial regeneration after injury.

Figure 6. Endothelial deletion of CSE alters histone acetylation signatures, chromatin accessibility, and transcription

(A) Contribution of ^{13}C-cystine to ^{13}C-pyruvate (Pyr) and $^{13}C_2$-acetyl-CoA in mouse lung microvascular endothelial cells from WT and iEC^{CSE} mice.
(B) Contribution of ^{13}C-cystine to $^{13}C_2$-acetyl-CoA (Cys) in cells as in (B).
(C and D) Histone acetyl-proteomics of ^{13}C-cystine (C) or unlabeled acetyl-proteomics (D) in cells as in (B).
(E) GCN5, HAT1, and CSE in the nuclear compartment of pre-proliferative endothelial cells cultured in either a cystine/cysteine-depleted media (ΔCC) or in media supplemented with 100 μmol L-cystine (CC) for 24 h, prior to PDHA1 immunoprecipitation.
(F) Heatmap showing relative enrichment of chromatin accessibility (ATAC-seq) and histone modifications (ACT-seq) across the 50,000 most variable genomic peaks in proliferating WT endothelial cells.
(G) Pearson correlation between the ATAC and ACT-seq overlapping genomic loci presented in (F).
(H–J) Representative immunoblot of H3 acetylation sites at lysine 9 and 23 in (H) WT and iEC^{CSE} endothelial cells, (I) cells treated for 4 h with solvent or glucose-deprived media (−Gluc), or (J) cells treated for 8 h with solvent or 800 μmol/L 2-S-hydroxyglutarate (2-SHG).
(K) ATAC coverage in all identified peaks between WT and iEC^{CSE} cells around the transcription start site (center) ± 2,000 bp.
(L) Volcano plot of ATAC-seq transcriptional factor footprinting analysis demonstrating differential binding score between WT (blue) and iEC^{CSE} (red) cells.
(M) Overlay of ATAC and RNA differentially expressed genes.
(N) Heatmap showing the top transcription factors for the differential enhancers of down- and upregulated differentially expressed genes (FDR $\leq$ 0.05, log2FC $\geq$ 0.585) from WT (blue) and iEC^{CSE} (red) endothelial cells.
(O) Volcano plot showing $\log_2$FC of all differentially expressed genes from mRNA-seq. Red, $\log_2 \geq 1.5$, $p < 0.005$; blue, $\log_2 \leq -1.5$, $p < 0.005$.
(P) Heatmap showing log2FC mRNA expression of ETS family targets. Yellow color annotates genes for a cell-cycle-related function. Venn diagram shows the overlay of ETS family targets and cell-cycle control genes.
n = 3–6 biological replicates and 2 technical replicates. Unpaired (A and C–E) and paired (B) Student's t test.

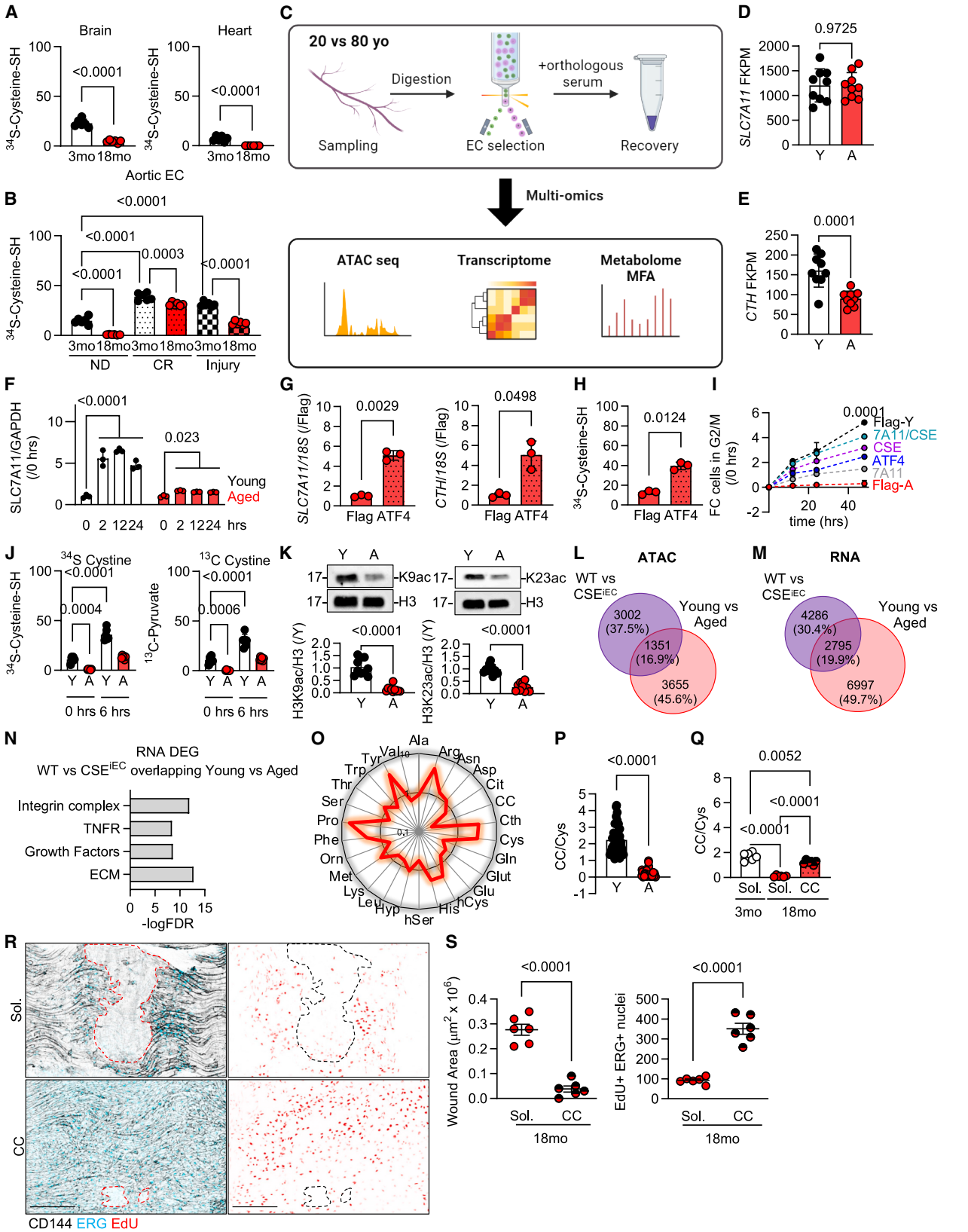

(legend on next page)

Endothelial cells import nutrients to sustain basal function[64,65] and when cycling increase uptake of carbon, nitrogen, and reducing agents for vascular expansion.[66] In our study, we report that prior to active proliferation, endothelial cells are modifying the nutrients imported and used. Sparse endothelial cells alter SLC expression to prime nutrient import and enter the cell cycle, which was recently linked to YAP/TAZ-TEAD activation and subsequent mTORC1-dependent protein synthesis and growth.[67] Among these, SLC7A11—a cystine/glutamate antiporter[68]—was the earliest and strongest responder. Biochemically, imported cystine is rapidly reduced to cysteine, a precursor for glutathione[69–73] and CoA,[74,75] making cysteine availability a therapeutic target in multiple pathologies. While endothelial dependence on cysteine varies—resisting ferroptosis[37] yet required for fitness[6,40,53,76,77]—its role in vascular growth remains elusive. Under nutrient deletion, ATF4-mediated CSE induction can enhance neovascularization via cysteine-to-sulfur flux,[51] but in our model, sulfur supplementation had minimal impact, suggesting a distinct pro-angiogenic role for cyst(e)ine. Here, we provide solid evidence that CSE regulates both cystine oxidative flux and *de novo* cysteine synthesis from methionine,[77,78] requiring a shift to homocysteine as substrate.[48] CSE's flexibility on substrate preference, though poorly studied,[79] may be therapeutically exploitable to lower homocysteine in hyperhomocysteinemia.

Notably, CSE preference for oxidatively catabolizing cystine to pyruvate defines a previously unrecognized pathway with broad implications for transcriptional regulation. While cysteine also influences epigenetics via CoA biosynthesis in melanoma,[80] the possibility of cystine itself to act as an alternative source for acetyl moieties was not studied. Here, we show that cystine itself fuels nuclear acetyl-moiety production, altering histone acetylation and chromatin structure in proliferating endothelial cells. Mechanistically, cystine bridges CSE to cytoplasmic PDHA1, enabling nuclear translocation of the complex and local acetyl-moiety production for nearby histone acetyltransferases (e.g., GCN5 and HAT1), ensuring site-specific H3 acetylation. Without cystine, PDHA1 still enters the nucleus but fails to sustain equivalent histone acetylation, impairing transcription and proliferation. Complete loss of cystine import and catabolism results in embryonic lethality and reduced vascular growth, whereas cystine supplementation after injury enhances neovascularization and improves organ function.

Metabolites can decorate histone lysines to reprogram transcription and cell fates,[81,82] but links to endothelial growth remain limited.[28,83] Here, we describe a rather unexpected epigenetic control mechanism of actively dividing endothelial cells, We show that cystine—not glucose—provides carbons for H3 lysine acetylation, opening chromatin to ETS transcription factors, key regulators of endothelial cell fates.[84,85] Notably, specific H3 lysine marks maintained before proliferation support transcription and angiogenic responses. Unlike universal cysteine-reductive metabolism, this oxidative pathway depends on CSE, which is cell-type specific[40] and sensitive to inflammation[86] and aging.[6] Yet oral administration of cystine was able to reverse the reduced cystine/cysteine ratio in the circulation and contributed to better endothelial cell proliferation after injury in the aged mice. Overall, our study shows that cystine, though normally non-essential, is crucial for vascular growth. Through CSE-driven oxidative catabolism, it sustains nuclear acetyl pools that safeguard endothelial transcriptional programs for cell-cycle entry and vessel formation. Although glycolysis remains the dominant energy source, cystine oxidation emerges as a complementary carbon pathway that primes endothelial proliferation. These findings position cystine metabolism as a therapeutic target to boost vascular regeneration in aging and injury.

Limitations of the study

The upstream cues driving SLC translational changes—particularly SLC7A11 induction in pre-proliferative endothelial cells—remain undefined. Cystine supplementation likely affects both vascular and non-vascular cells, contributing to the *in vivo*

Figure 7. Cystine oxidative catabolism is blunted in aging, while cystine administration enhances vascular regeneration

(A and B) Cystine oxidative flux to cysteine-SH in (A) brain and heart and (B) aortic endothelial cells. Young (3-month [3mo]) vs. aged (18-month [18mo]) mice, homeostatic (normal diet, ND), caloric restriction (CR), or after injury.

(C) Graphical abstract showing human native endothelial cell isolation and analysis.

(D and E) Fragments per kilobase per million (FKPM) following RNA-seq in endothelial cells isolated from 20- (young, Y) and 80- (aged, A) year-old individuals.

(F) SLC7A11/GAPDH levels in young and aged human native endothelial cells 0, 2, 12, and 24 h after adhesion.

(G) Relative mRNA levels of SLC7A11 and CTH in aged human native endothelial cells following lentiviral overexpression of a control virus (FLAG) or a virus overexpressing ATF4.

(H) Percentage of ^{34}S-cystine contribution to ^{34}S-cysteine-SH in samples as in (G).

(I) Fold change (FC) of cells in G2/M in aged human native endothelial cells following lentiviral overexpression of a control virus (FLAG) or a virus overexpressing ATF4, or SLC7A11 and/or CSE.

(J) Percentage of contribution to ^{34}S-cysteine-SH and ^{13}C-pyruvate following 30 min labeling with ^{34}S- or ^{13}C-cystine in baseline or following 6 h post-adhesion in human native young and aged endothelial cells.

(K) H3K9ac, H3K23ac, and H3 in samples as in (G).

(L and M) Overlapping of differentially accessible ATAC peaks (L) or mRNA transcripts (M) between murine endothelial cells isolated from WT or CSE^{iEC} mice and young or aged human native endothelial cells.

(N) GO enrichment analysis of mRNA transcripts overlapping in (M).

(O) Aminogram showing relative fold change in the plasma of aged compared with young individuals, $n = 90$.

(P) Cystine-to-cysteine ratio in plasma from samples as in (O).

(Q) Cystine-to-cysteine ratio in plasma from animals at 3 and 18 months, receiving solvent or 100 mg/kg/day cystine in the drinking water 1 day prior to and for 72 h following aortic injury.

(R) Immunofluorescent staining (ERG, cyan; EdU, red; CD144, black; scale bar, 200 μm) in 18-month-old mice treated as in (Q).

(S) Percentage of wound area and EdU$^+$ERG$^+$ endothelial cells in samples as in (R).

$n = 3$–9 biological replicates. One-way ANOVA with Bonferroni (A and B) and paired (D–K) and unpaired (Q) Student's *t* test.

regenerative effects. While vascularization increases after cystine supplementation in AMI models, we cannot come to a conclusion on endothelial proliferation during the regenerative early days following injury. Anti-angiogenic phenotypes induced by cystine depletion or CSE loss might be partly mediated by chromatin remodeling at ETS transcription factors such as ERG[62,87,88] and ETV2,[89] with downstream effects on Notch signaling transcripts,[62] rather than solely from loss of histone acetylation. Finally, the extent of this oxidative catabolic pathway across vascular beds or non-endothelial tissues and its modulation by aging remains to be determined.

RESOURCE AVAILABILITY

Lead contact

Requests for further information and resources should be directed to and will be fulfilled by the lead contact, Sofia-Iris Bibli (iris.bibli@medma.uni-heidelberg.de).

Material availability

Plasmids and mouse lines generated in this study are listed in STAR Methods and the key resources table and will be made available upon request.

Data and code availability

- This paper does not report original code; all R packages used are listed in the STAR Methods and the key resources table.
- Raw data are found in Data S1.
- Proteomics raw data have been deposited at PRIDE: PXD068385. Sequencing raw data have been deposited at GEO: GSE214476, GSE305819, GSE305820, GSE305822, GSE305823, GSE305824, GSE305826, and GSE305827.

ACKNOWLEDGMENTS

The authors are indebted to Britta Heckmann for expert technical assistance. Schematics were created with Biorender.com (https://BioRender.com/rpl1aj7). We also thank the FlowCore Mannheim, the Live Cell Imaging Mannheim (LIMa), and the Preclinical Models Core Facilities of the UMM. This work was supported by the Deutsche Forschungsgemeinschaft (CRC1531/1; A02 to S.-I.B., A03 to R.P.B., A05 to M. Siragusa, and B03 to J. Hu and I.F., S03 to M.H.S., project ID 456687919; CRC1366/2; B01 to I.F. and S.-I.B., C06 to M. Singhal, A03 to G.D., A06 to J. Heineke, and B08 to H.F.L., project ID 39404578); the Emmy Noether Programme BI 2163/1-1 to S.-I.B.; the Cardio-pulmonary Institute, EXC 2026, project ID 390649896 to I.F., R.P.B., and M.H.S.; the National Natural Science Foundation of China, Project IDs 82070501, 82271479, and 32350021 to J. Hu; and the Onnasis Foundation to M.-K.D.

AUTHOR CONTRIBUTIONS

Conceptualization, S.-I.B.; study design, S.-I.B.; writing, S.-I.B., M.-K.D., and J.M.; methodology, S.-I.B., M.-K.D., D. Wang, J.M., F.D.L., C.K., J.E., Y.M., M. B., D. Weichenhan, J.W., B.Z., H.C., X.L., J.O., A.W., M. Siragusa, A.P., S.K., M. Singhal, and J. Hu; sequencing and bioinformatics, D.H., J.C., S.G., M.L., and M.H.S.; conceptual advice, I.F., A.P., R.P.B., M. Singhal, H.L., C.P., J. Heineke, G.D., and J. Hu; and all authors read the manuscript and provided feedback before submission.

DECLARATION OF INTERESTS

The authors declare no conflicts of interest.

STAR★METHODS

Detailed methods are provided in the online version of this paper and include the following:

SUPPLEMENTAL INFORMATION

Supplemental information can be found online at https://doi.org/10.1016/j.cmet.2025.10.003.

Received: November 2, 2024
Revised: July 6, 2025
Accepted: October 5, 2025
Published: October 31, 2025

REFERENCES

1. Augustin, H.G., and Koh, G.Y. (2024). A systems view of the vascular endothelium in health and disease. Cell *187*, 4833–4858. https://doi.org/10.1016/j.cell.2024.07.012.
2. Augustin, H.G., and Kipnis, J. (2021). Vascular rejuvenation is geroprotective. Science *373*, 490–491. https://doi.org/10.1126/science.abj8674.
3. Grunewald, M., Kumar, S., Sharife, H., Volinsky, E., Gileles-Hillel, A., Licht, T., Permyakova, A., Hinden, L., Azar, S., Friedmann, Y., et al. (2021). Counteracting age-related VEGF signaling insufficiency promotes healthy aging and extends life span. Science *373*, eabc8479. https://doi.org/10.1126/science.abc8479.
4. Suda, M., Shimizu, I., Katsuumi, G., Yoshida, Y., Hayashi, Y., Ikegami, R., Matsumoto, N., Yoshida, Y., Mikawa, R., Katayama, A., et al. (2021). Senolytic vaccination improves normal and pathological age-related phenotypes and increases lifespan in progeroid mice. Nat. Aging *1*, 1117–1126. https://doi.org/10.1038/s43587-021-00151-2.

5. Wagner, J.U.G., Tombor, L.S., Malacarne, P.F., Kettenhausen, L.-M., Panthel, J., Kujundzic, H., Manickam, N., Schmitz, K., Cipca, M., Stilz, K.A., et al. (2023). Aging impairs the neurovascular interface in the heart. Science *381*, 897–906. https://doi.org/10.1126/science.ade4961.

6. Hu, J., Leisegang, M.S., Looso, M., Drekolia, M.-K., Wittig, J., Mettner, J., Karantanou, C., Kyselova, A., Dumbovic, G., Li, X., et al. (2023). Disrupted binding of cystathionine γ-lyase to p53 promotes endothelial senescence. Circ. Res. *133*, 842–857. https://doi.org/10.1161/CIRCRESAHA.123.323084.

7. Falkenberg, K.D., Rohlenova, K., Luo, Y., and Carmeliet, P. (2019). The metabolic engine of endothelial cells. Nat. Metab. *1*, 937–946. https://doi.org/10.1038/s42255-019-0117-9.

8. Eelen, G., de Zeeuw, P., Treps, L., Harjes, U., Wong, B.W., and Carmeliet, P. (2018). Endothelial cell metabolism. Physiol. Rev. *98*, 3–58. https://doi.org/10.1152/physrev.00001.2017.

9. De Bock, K., Georgiadou, M., Schoors, S., Kuchnio, A., Wong, B.W., Cantelmo, A.R., Quaegebeur, A., Ghesquière, B., Cauwenberghs, S., Eelen, G., et al. (2013). Role of PFKFB3-driven glycolysis in vessel sprouting. Cell *154*, 651–663. https://doi.org/10.1016/j.cell.2013.06.037.

10. Schoors, S., Bruning, U., Missiaen, R., Queiroz, K.C., Borgers, G., Elia, I., Zecchin, A., Cantelmo, A.R., Christen, S., Goveia, J., et al. (2015). Fatty acid carbon is essential for dNTP synthesis in endothelial cells. Nature *520*, 192–197. https://doi.org/10.1038/nature14362.

11. Welti, J., Loges, S., Dimmeler, S., and Carmeliet, P. (2013). Recent molecular discoveries in angiogenesis and antiangiogenic therapies in cancer. J. Clin. Invest. *123*, 3190–3200. https://doi.org/10.1172/JCI70212.

12. Figlia, G., Willnow, P., and Teleman, A.A. (2020). Metabolites regulate cell signaling and growth via covalent modification of proteins. Dev. Cell *54*, 156–170. https://doi.org/10.1016/j.devcel.2020.06.036.

13. Li, X., Egervari, G., Wang, Y., Berger, S.L., and Lu, Z. (2018). Regulation of chromatin and gene expression by metabolic enzymes and metabolites. Nat. Rev. Mol. Cell Biol. *19*, 563–578. https://doi.org/10.1038/s41580-018-0029-7.

14. Dai, Z., Ramesh, V., and Locasale, J.W. (2020). The evolving metabolic landscape of chromatin biology and epigenetics. Nat. Rev. Genet. *21*, 737–753. https://doi.org/10.1038/s41576-020-0270-8.

15. Piunti, A., and Shilatifard, A. (2016). Epigenetic balance of gene expression by Polycomb and COMPASS families. Science *352*, aad9780. https://doi.org/10.1126/science.aad9780.

16. ENCODE; Project Consortium (2012). An integrated encyclopedia of DNA elements in the human genome. Nature *489*, 57–74. https://doi.org/10.1038/nature11247.

17. Shogren-Knaak, M., Ishii, H., Sun, J.-M., Pazin, M.J., Davie, J.R., and Peterson, C.L. (2006). Histone H4-K16 acetylation controls chromatin structure and protein interactions. Science *311*, 844–847. https://doi.org/10.1126/science.1124000.

18. Bannister, A.J., and Kouzarides, T. (2011). Regulation of chromatin by histone modifications. Cell Res. *21*, 381–395. https://doi.org/10.1038/cr.2011.22.

19. Bannister, A.J., Zegerman, P., Partridge, J.F., Miska, E.A., Thomas, J.O., Allshire, R.C., and Kouzarides, T. (2001). Selective recognition of methylated lysine 9 on histone H3 by the HP1 chromo domain. Nature *410*, 120–124. https://doi.org/10.1038/35065138.

20. Chen, R.-J., Shun, C.-T., Yen, M.-L., Chou, C.-H., and Lin, M.-C. (2017). Methyltransferase G9a promotes cervical cancer angiogenesis and decreases patient survival. Oncotarget *8*, 62081–62098. https://doi.org/10.18632/oncotarget.19060.

21. Duan, Y., Wu, X., Zhao, Q., Gao, J., Huo, D., Liu, X., Ye, Z., Dong, X., Fu, Z., Shang, Y., et al. (2016). DOT1L promotes angiogenesis through cooperative regulation of VEGFR2 with ETS-1. Oncotarget *7*, 69674–69687. https://doi.org/10.18632/oncotarget.11939.

22. Jacobson, R.H., Ladurner, A.G., King, D.S., and Tjian, R. (2000). Structure and function of a human TAFII250 double bromodomain module. Science *288*, 1422–1425. https://doi.org/10.1126/science.288.5470.1422.

23. Kim, T.-K., Hemberg, M., Gray, J.M., Costa, A.M., Bear, D.M., Wu, J., Harmin, D.A., Laptewicz, M., Barbara-Haley, K., Kuersten, S., et al. (2010). Widespread transcription at neuronal activity-regulated enhancers. Nature *465*, 182–187. https://doi.org/10.1038/nature09033.

24. Liang, G., Lin, J.C.Y., Wei, V., Yoo, C., Cheng, J.C., Nguyen, C.T., Weisenberger, D.J., Egger, G., Takai, D., Gonzales, F.A., et al. (2004). Distinct localization of histone H3 acetylation and H3-K4 methylation to the transcription start sites in the human genome. Proc. Natl. Acad. Sci. USA *101*, 7357–7362. https://doi.org/10.1073/pnas.0401866101.

25. Rada-Iglesias, A., Bajpai, R., Swigut, T., Brugmann, S.A., Flynn, R.A., and Wysocka, J. (2011). A unique chromatin signature uncovers early developmental enhancers in humans. Nature *470*, 279–283. https://doi.org/10.1038/nature09692.

26. Utley, R.T., Ikeda, K., Grant, P.A., Côté, J., Steger, D.J., Eberharter, A., John, S., and Workman, J.L. (1998). Transcriptional activators direct histone acetyltransferase complexes to nucleosomes. Nature *394*, 498–502. https://doi.org/10.1038/28886.

27. Bazou, D., Ng, M.R., Song, J.W., Chin, S.M., Maimon, N., and Munn, L.L. (2016). Flow-induced HDAC1 phosphorylation and nuclear export in angiogenic sprouting. Sci. Rep. *6*, 34046. https://doi.org/10.1038/srep34046.

28. Kim, M.S., Kwon, H.J., Lee, Y.M., Baek, J.H., Jang, J.E., Lee, S.W., Moon, E.J., Kim, H.S., Lee, S.K., Chung, H.Y., et al. (2001). Histone deacetylases induce angiogenesis by negative regulation of tumor suppressor genes. Nat. Med. *7*, 437–443. https://doi.org/10.1038/86507.

29. Iizuka, N., Morita, A., Kawano, C., Mori, A., Sakamoto, K., Kuroyama, M., Ishii, K., and Nakahara, T. (2018). Anti-angiogenic effects of valproic acid in a mouse model of oxygen-induced retinopathy. J. Pharmacol. Sci. *138*, 203–208. https://doi.org/10.1016/j.jphs.2018.10.004.

30. Michaelis, M., Michaelis, U.R., Fleming, I., Suhan, T., Cinatl, J., Blaheta, R.A., Hoffmann, K., Kotchetkov, R., Busse, R., Nau, H., et al. (2004). Valproic acid inhibits angiogenesis in vitro and in vivo. Mol. Pharmacol. *65*, 520–527. https://doi.org/10.1124/mol.65.3.520.

31. Kalucka, J., Bierhansl, L., Conchinha, N.V., Missiaen, R., Elia, I., Brüning, U., Scheinok, S., Treps, L., Cantelmo, A.R., Dubois, C., et al. (2018). Quiescent endothelial cells upregulate fatty acid β-oxidation for vasculoprotection via redox homeostasis. Cell Metab. *28*, 881–894.e13. https://doi.org/10.1016/j.cmet.2018.07.016.

32. Parker, J.L., Deme, J.C., Kolokouris, D., Kuteyi, G., Biggin, P.C., Lea, S.M., and Newstead, S. (2021). Molecular basis for redox control by the human cystine/glutamate antiporter system xc. Nat. Commun. *12*, 7147. https://doi.org/10.1038/s41467-021-27414-1.

33. Zhang, Y., Tan, H., Daniels, J.D., Zandkarimi, F., Liu, H., Brown, L.M., Uchida, K., O'Connor, O.A., and Stockwell, B.R. (2019). Imidazole ketone erastin induces ferroptosis and slows tumor growth in a mouse lymphoma model. Cell Chem. Biol. *26*, 623–633.e9. https://doi.org/10.1016/j.chembiol.2019.01.008.

34. Ferrari, S., Bandi, H.R., Hofsteenge, J., Bussian, B.M., and Thomas, G. (1991). Mitogen-activated 70K S6 kinase. Identification of in vitro 40 S ribosomal S6 phosphorylation sites. J. Biol. Chem. *266*, 22770–22775. https://doi.org/10.1016/S0021-9258(18)54634-2.

35. Dufner, A., and Thomas, G. (1999). Ribosomal S6 kinase signaling and the control of translation. Exp. Cell Res. *253*, 100–109. https://doi.org/10.1006/excr.1999.4683.

36. Yang, W.S., and Stockwell, B.R. (2016). Ferroptosis: death by lipid peroxidation. Trends Cell Biol. *26*, 165–176. https://doi.org/10.1016/j.tcb.2015.10.014.

37. Wortmann, M., Schneider, M., Pircher, J., Hellfritsch, J., Aichler, M., Vegi, N., Kölle, P., Kuhlencordt, P., Walch, A., Pohl, U., et al. (2013). Combined deficiency in glutathione peroxidase 4 and vitamin E causes multiorgan thrombus formation and early death in mice. Circ. Res. *113*, 408–417. https://doi.org/10.1161/CIRCRESAHA.113.279984.

38. Jakobsson, L., Franco, C.A., Bentley, K., Collins, R.T., Ponsioen, B., Aspalter, I.M., Rosewell, I., Busse, M., Thurston, G., Medvinsky, A., et al. (2010). Endothelial cells dynamically compete for the tip cell position during angiogenic sprouting. Nat. Cell Biol. *12*, 943–953. https://doi.org/10.1038/ncb2103.

39. Sicklinger, F., Zhang, Y., Lavine, K.J., Simon, N., Bucher, V., Jugold, M., Lehmann, L., Konstandin, M.H., Katus, H.A., and Leuschner, F. (2020). A minimal-invasive approach for standardized induction of myocardial infarction in mice. Circ. Res. *127*, 1214–1216. https://doi.org/10.1161/CIRCRESAHA.120.317794.

40. Bibli, S.-I., and Fleming, I. (2021). Oxidative post-translational modifications: A focus on cysteine S-sulfhydration and the regulation of endothelial fitness. Antioxid. Redox Signal. *35*, 1494–1514. https://doi.org/10.1089/ars.2021.0162.

41. Miseta, A., and Csutora, P. (2000). Relationship between the occurrence of cysteine in proteins and the complexity of organisms. Mol. Biol. Evol. *17*, 1232–1239. https://doi.org/10.1093/oxfordjournals.molbev.a026406.

42. Yoon, S.J., Combs, J.A., Falzone, A., Prieto-Farigua, N., Caldwell, S., Ackerman, H.D., Flores, E.R., and DeNicola, G.M. (2023). Comprehensive metabolic tracing reveals the origin and catabolism of cysteine in mammalian tissues and tumors. Cancer Res. *83*, 1426–1442. https://doi.org/10.1158/0008-5472.CAN-22-3000.

43. Shibuya, N., and Kimura, H. (2013). Production of hydrogen sulfide from d-cysteine and its therapeutic potential. Front. Endocrinol. *4*, 87. https://doi.org/10.3389/fendo.2013.00087.

44. Chua, B.H., Giger, K.E., Kleinhans, B.J., Robishaw, J.D., and Morgan, H.E. (1984). Differential effects of cysteine on protein and coenzyme A synthesis in rat heart. Am. J. Physiol. *247*, C99–C106. https://doi.org/10.1152/ajpcell.1984.247.1.C99.

45. Stipanuk, M.H., and Ueki, I. (2011). Dealing with methionine/homocysteine sulfur: cysteine metabolism to taurine and inorganic sulfur. J. Inherit. Metab. Dis. *34*, 17–32. https://doi.org/10.1007/s10545-009-9006-9.

46. Höfler, S., Lorenz, C., Busch, T., Brinkkötter, M., Tohge, T., Fernie, A.R., Braun, H.-P., and Hildebrandt, T.M. (2016). Dealing with the sulfur part of cysteine: four enzymatic steps degrade l-cysteine to pyruvate and thiosulfate in Arabidopsis mitochondria. Physiol. Plant. *157*, 352–366. https://doi.org/10.1111/ppl.12454.

47. Borbényi-Galambos, K., Erdélyi, K., Ditrói, T., Jurányi, E.P., Szántó, N., Szatmári, R., Czikora, Á., Schmidt, E.E., Garai, D., Cserepes, M., et al. (2025). Realigned transsulfuration drives BRAF-V600E-targeted therapy resistance in melanoma. Cell Metab. *37*, 1171–1188.e9. https://doi.org/10.1016/j.cmet.2025.01.021.

48. Singh, S., Padovani, D., Leslie, R.A., Chiku, T., and Banerjee, R. (2009). Relative contributions of cystathionine beta-synthase and gamma-cystathionase to H_2S biogenesis via alternative trans-sulfuration reactions. J. Biol. Chem. *284*, 22457–22466. https://doi.org/10.1074/jbc.M109.010868.

49. Pakos-Zebrucka, K., Koryga, I., Mnich, K., Ljujic, M., Samali, A., and Gorman, A.M. (2016). The integrated stress response. EMBO Rep. *17*, 1374–1395. https://doi.org/10.15252/embr.201642195.

50. Labbé, K., LeBon, L., King, B., Vu, N., Stoops, E.H., Ly, N., Lefebvre, A.E.Y.T., Seitzer, P., Krishnan, S., Heo, J.-M., et al. (2024). Specific activation of the integrated stress response uncovers regulation of central carbon metabolism and lipid droplet biogenesis. Nat. Commun. *15*, 8301. https://doi.org/10.1038/s41467-024-52538-5.

51. Longchamp, A., Mirabella, T., Arduini, A., MacArthur, M.R., Das, A., Treviño-Villarreal, J.H., Hine, C., Ben-Sahra, I., Knudsen, N.H., Brace, L.E., et al. (2018). Amino acid restriction triggers angiogenesis via GCN2/ATF4 regulation of VEGF and H_2S production. Cell *173*, 117–129.e14. https://doi.org/10.1016/j.cell.2018.03.001.

52. Sbodio, J.I., Snyder, S.H., and Paul, B.D. (2016). Transcriptional control of amino acid homeostasis is disrupted in Huntington's disease. Proc. Natl. Acad. Sci. USA *113*, 8843–8848. https://doi.org/10.1073/pnas.1608264113.

53. Bibli, S.-I., Hu, J., Looso, M., Weigert, A., Ratiu, C., Wittig, J., Drekolia, M.K., Tombor, L., Randriamboavonjy, V., Leisegang, M.S., et al. (2021). Mapping the endothelial cell S-sulfhydrome highlights the crucial role of integrin sulfhydration in vascular function. Circulation *143*, 935–948. https://doi.org/10.1161/CIRCULATIONAHA.120.051877.

54. Pietrocola, F., Galluzzi, L., Bravo-San Pedro, J.M., Madeo, F., and Kroemer, G. (2015). Acetyl coenzyme A: a central metabolite and second messenger. Cell Metab. *21*, 805–821. https://doi.org/10.1016/j.cmet.2015.05.014.

55. Piazza, I., Kochanowski, K., Cappelletti, V., Fuhrer, T., Noor, E., Sauer, U., and Picotti, P. (2018). A map of protein-metabolite interactions reveals principles of chemical communication. Cell *172*, 358–372.e23. https://doi.org/10.1016/j.cell.2017.12.006.

56. Liu, Y., Yang, X., Gan, J., Chen, S., Xiao, Z.-X., and Cao, Y. (2022). CB-Dock2: improved protein-ligand blind docking by integrating cavity detection, docking and homologous template fitting. Nucleic Acids Res. *50*, W159–W164. https://doi.org/10.1093/nar/gkac394.

57. Gowers, R., Linke, M., Barnoud, J., Reddy, T., Melo, M., Seyler, S., Domański, J., Dotson, D., Buchoux, S., Kenney, I., et al. (2016). MDAnalysis: A python package for the rapid analysis of molecular dynamics simulations. Proceedings of the 15th Python in Science Conference (SciPy), 98–105. https://doi.org/10.25080/Majora-629e541a-00e.

58. Carter, B., Ku, W.L., Kang, J.Y., Hu, G., Perrie, J., Tang, Q., and Zhao, K. (2019). Mapping histone modifications in low cell number and single cells using antibody-guided chromatin tagmentation (ACT-seq). Nat. Commun. *10*, 3747. https://doi.org/10.1038/s41467-019-11559-1.

59. Kurdistani, S.K., Tavazoie, S., and Grunstein, M. (2004). Mapping global histone acetylation patterns to gene expression. Cell *117*, 721–733. https://doi.org/10.1016/j.cell.2004.05.023.

60. Andrade, J., Shi, C., Costa, A.S.H., Choi, J., Kim, J., Doddaballapur, A., Sugino, T., Ong, Y.T., Castro, M., Zimmermann, B., et al. (2021). Control of endothelial quiescence by FOXO-regulated metabolites. Nat. Cell Biol. *23*, 413–423. https://doi.org/10.1038/s41556-021-00637-6.

61. Ren, J., Xiao, X., Li, R., Lv, C., Zhang, Y., Wang, L., Hong, T., Zhang, H., and Wang, Y. (2023). Single-cell sequencing reveals that endothelial cells, EndMT cells and mural cells contribute to the pathogenesis of cavernous malformations. Exp. Mol. Med. *55*, 628–642. https://doi.org/10.1038/s12276-023-00962-w.

62. Shah, A.V., Birdsey, G.M., Peghaire, C., Pitulescu, M.E., Dufton, N.P., Yang, Y., Weinberg, I., Osuna Almagro, L., Payne, L., Mason, J.C., et al. (2017). The endothelial transcription factor ERG mediates Angiopoietin-1-dependent control of Notch signalling and vascular stability. Nat. Commun. *8*, 16002. https://doi.org/10.1038/ncomms16002.

63. Donato, A.J., Machin, D.R., and Lesniewski, L.A. (2018). Mechanisms of dysfunction in the aging vasculature and role in age-related disease. Circ. Res. *123*, 825–848. https://doi.org/10.1161/CIRCRESAHA.118.312563.

64. Augustin, H.G., and Koh, G.Y. (2017). Organotypic vasculature: From descriptive heterogeneity to functional pathophysiology. Science *357*, eaal2379. https://doi.org/10.1126/science.aal2379.

65. Potente, M., and Mäkinen, T. (2017). Vascular heterogeneity and specialization in development and disease. Nat. Rev. Mol. Cell Biol. *18*, 477–494. https://doi.org/10.1038/nrm.2017.36.

66. Li, X., Sun, X., and Carmeliet, P. (2019). Hallmarks of endothelial cell metabolism in health and disease. Cell Metab. *30*, 414–433. https://doi.org/10.1016/j.cmet.2019.08.011.

67. Ong, Y.T., Andrade, J., Armbruster, M., Shi, C., Castro, M., Costa, A.S.H., Sugino, T., Eelen, G., Zimmermann, B., Wilhelm, K., et al. (2022). A YAP/TAZ-TEAD signalling module links endothelial nutrient acquisition to angiogenic growth. Nat. Metab. *4*, 672–682. https://doi.org/10.1038/s42255-022-00584-y.

68. Shin, C.-S., Mishra, P., Watrous, J.D., Carelli, V., D'Aurelio, M., Jain, M., and Chan, D.C. (2017). The glutamate/cystine xCT antiporter antagonizes glutamine metabolism and reduces nutrient flexibility. Nat. Commun. *8*, 15074. https://doi.org/10.1038/ncomms15074.

69. Badgley, M.A., Kremer, D.M., Maurer, H.C., DelGiorno, K.E., Lee, H.-J., Purohit, V., Sagalovskiy, I.R., Ma, A., Kapilian, J., Firl, C.E.M., et al. (2020). Cysteine depletion induces pancreatic tumor ferroptosis in mice. Science *368*, 85–89. https://doi.org/10.1126/science.aaw9872.

70. Bonifácio, V.D.B., Pereira, S.A., Serpa, J., and Vicente, J.B. (2021). Cysteine metabolic circuitries: druggable targets in cancer. Br. J. Cancer *124*, 862–879. https://doi.org/10.1038/s41416-020-01156-1.

71. Combs, J.A., and DeNicola, G.M. (2019). The non-essential amino acid cysteine becomes essential for tumor proliferation and survival. Cancers *11*, 678. https://doi.org/10.3390/cancers11050678.

72. Koppula, P., Zhuang, L., and Gan, B. (2021). Cystine transporter SLC7A11/xCT in cancer: ferroptosis, nutrient dependency, and cancer therapy. Protein Cell *12*, 599–620. https://doi.org/10.1007/s13238-020-00789-5.

73. Liu, X., Olszewski, K., Zhang, Y., Lim, E.W., Shi, J., Zhang, X., Zhang, J., Lee, H., Koppula, P., Lei, G., et al. (2020). Cystine transporter regulation of pentose phosphate pathway dependency and disulfide stress exposes a targetable metabolic vulnerability in cancer. Nat. Cell Biol. *22*, 476–486. https://doi.org/10.1038/s41556-020-0496-x.

74. Lee, A.H., Orliaguet, L., Youm, Y.-H., Maeda, R., Dlugos, T., Lei, Y., Coman, D., Shchukina, I., Andhey, P.S., Smith, S.R., et al. (2025). Cysteine depletion triggers adipose tissue thermogenesis and weight loss. Nat. Metab. *7*, 1204–1222. https://doi.org/10.1038/s42255-025-01297-8.

75. Varghese, A., Gusarov, I., Gamallo-Lana, B., Dolgonos, D., Mankan, Y., Shamovsky, I., Phan, M., Jones, R., Gomez-Jenkins, M., White, E., et al. (2025). Unravelling cysteine-deficiency-associated rapid weight loss. Nature *643*, 776–784. https://doi.org/10.1038/s41586-025-08996-y.

76. Bibli, S.-I., Hu, J., Leisegang, M.S., Wittig, J., Zukunft, S., Kapasakalidi, A., Fisslthaler, B., Tsilimigras, D., Zografos, G., Filis, K., et al. (2020). Shear stress regulates cystathionine γ lyase expression to preserve endothelial redox balance and reduce membrane lipid peroxidation. Redox Biol. *28*, 101379. https://doi.org/10.1016/j.redox.2019.101379.

77. Nagahara, N., and Sawada, N. (2006). The mercaptopyruvate pathway in cysteine catabolism: a physiologic role and related disease of the multifunctional 3-mercaptopyruvate sulfurtransferase. Curr. Med. Chem. *13*, 1219–1230. https://doi.org/10.2174/092986706776360914.

78. Serpa, J. (2020). Cysteine as a carbon source, a hot spot in cancer cells survival. Front. Oncol. *10*, 947. https://doi.org/10.3389/fonc.2020.00947.

79. Alam, S., Pardue, S., Shen, X., Glawe, J.D., Yagi, T., Bhuiyan, M.A.N., Patel, R.P., Dominic, P.S., Virk, C.S., Bhuiyan, M.S., et al. (2023). Hypoxia increases persulfide and polysulfide formation by AMP kinase dependent cystathionine gamma lyase phosphorylation. Redox Biol. *68*, 102949. https://doi.org/10.1016/j.redox.2023.102949.

80. Yu, D., Liang, J., Widlund, H.R., and Puigserver, P. (2024). Feedforward cysteine regulation maintains melanoma differentiation state and limits metastatic spread. Cell Rep. *43*, 114484. https://doi.org/10.1016/j.celrep.2024.114484.

81. Janke, R., Dodson, A.E., and Rine, J. (2015). Metabolism and epigenetics. Annu. Rev. Cell Dev. Biol. *31*, 473–496. https://doi.org/10.1146/annurev-cellbio-100814-125544.

82. Ly, C.H., Lynch, G.S., and Ryall, J.G. (2020). A metabolic roadmap for somatic stem cell fate. Cell Metab. *31*, 1052–1067. https://doi.org/10.1016/j.cmet.2020.04.022.

83. Ni, L., Lin, B., Zhang, Y., Hu, L., Lin, J., Fu, F., Shen, M., Li, C., Chen, L., Yang, J., et al. (2023). Histone modification landscape and the key significance of H3K27me3 in myocardial ischaemia/reperfusion injury. Sci. China Life Sci. *66*, 1264–1279. https://doi.org/10.1007/s11427-022-2257-9.

84. Gomez-Salinero, J.M., Itkin, T., Houghton, S., Badwe, C., Lin, Y., Kalna, V., Dufton, N., Peghaire, C.R., Yokoyama, M., Wingo, M., et al. (2022). Cooperative ETS transcription factors enforce adult endothelial cell fate and cardiovascular homeostasis. Nat. Cardiovasc. Res. *1*, 882–899. https://doi.org/10.1038/s44161-022-00128-3.

85. Craig, M.P., and Sumanas, S. (2016). ETS transcription factors in embryonic vascular development. Angiogenesis *19*, 275–285. https://doi.org/10.1007/s10456-016-9511-z.

86. Bibli, S.-I., Hu, J., Sigala, F., Wittig, I., Heidler, J., Zukunft, S., Tsilimigras, D.I., Randriamboavonjy, V., Wittig, J., Kojonazarov, B., et al. (2019). Cystathionine γ lyase sulfhydrates the RNA binding protein Human Antigen R to preserve endothelial cell function and delay atherogenesis. Circulation *139*, 101–114. https://doi.org/10.1161/CIRCULATIONAHA.118.034757.

87. Birdsey, G.M., Dryden, N.H., Amsellem, V., Gebhardt, F., Sahnan, K., Haskard, D.O., Dejana, E., Mason, J.C., and Randi, A.M. (2008). Transcription factor Erg regulates angiogenesis and endothelial apoptosis through VE-cadherin. Blood *111*, 3498–3506. https://doi.org/10.1182/blood-2007-08-105346.

88. McLaughlin, F., Ludbrook, V.J., Cox, J., von Carlowitz, I., Brown, S., and Randi, A.M. (2001). Combined genomic and antisense analysis reveals that the transcription factor Erg is implicated in endothelial cell differentiation. Blood *98*, 3332–3339. https://doi.org/10.1182/blood.v98.12.3332.

89. Garry, D.J. (2016). Etv2 is a master regulator of hemoendothelial lineages. Trans. Am. Clin. Climatol. Assoc. *127*, 212–223.

90. Drekolia, M.-K., Karantanou, C., Wittig, I., Li, Y., Fuhrmann, D.C., Brüne, B., Katsouda, A., Hu, J., Papapetropoulos, A., and Bibli, S.-I. (2024). Loss of cardiac mitochondrial complex I persulfidation impairs NAD^+ homeostasis in aging. Redox Biol. *69*, 103014. https://doi.org/10.1016/j.redox.2023.103014.

91. Hu, J., Bibli, S.-I., Wittig, J., Zukunft, S., Lin, J., Hammes, H.-P., Popp, R., and Fleming, I. (2019). Soluble epoxide hydrolase promotes astrocyte survival in retinopathy of prematurity. J. Clin. Invest. *129*, 5204–5218. https://doi.org/10.1172/JCI123835.

92. Connor, K.M., Krah, N.M., Dennison, R.J., Aderman, C.M., Chen, J., Guerin, K.I., Sapieha, P., Stahl, A., Willett, K.L., and Smith, L.E.H. (2009). Quantification of oxygen-induced retinopathy in the mouse: a model of vessel loss, vessel regrowth and pathological angiogenesis. Nat. Protoc. *4*, 1565–1573. https://doi.org/10.1038/nprot.2009.187.

93. Cao, M., Li, M., Li, X., Li, Y., Chen, Y., Drekolia, M.-K., Cheng, X., Lagos, F.D., Bibli, S.-I., and Hu, J. (2025). Endothelial soluble epoxide hydrolase links polyunsaturated fatty acid metabolism to oxidative stress and atherosclerosis progression. Redox Biol. *85*, 103730. https://doi.org/10.1016/j.redox.2025.103730.

94. Chen, W.W., Freinkman, E., Wang, T., Birsoy, K., and Sabatini, D.M. (2016). Absolute quantification of matrix metabolites reveals the dynamics of mitochondrial metabolism. Cell *166*, 1324–1337.e11. https://doi.org/10.1016/j.cell.2016.07.040.

95. Shechter, D., Dormann, H.L., Allis, C.D., and Hake, S.B. (2007). Extraction, purification and analysis of histones. Nat. Protoc. *2*, 1445–1457. https://doi.org/10.1038/nprot.2007.202.

96. Hu, J., Dziumbla, S., Lin, J., Bibli, S.-I., Zukunft, S., de Mos, J., Awwad, K., Frömel, T., Jungmann, A., Devraj, K., et al. (2017). Inhibition of soluble epoxide hydrolase prevents diabetic retinopathy. Nature *552*, 248–252. https://doi.org/10.1038/nature25013.

97. Drekolia, M.-K., Talyan, S., Cordellini Emídio, R., Boon, R.A., Guenther, S., Looso, M., Dumbović, G., and Bibli, S.-I. (2022). Unravelling the impact of aging on the human endothelial lncRNA transcriptome. Front. Genet. *13*, 1035380. https://doi.org/10.3389/fgene.2022.1035380.

98. Zippel, N., Ding, Y., and Fleming, I. (2016). A modified aortic ring assay to assess angiogenic potential in vitro. Methods Mol. Biol. *1430*, 205–219. https://doi.org/10.1007/978-1-4939-3628-1_14.

99. Corces, M.R., Trevino, A.E., Hamilton, E.G., Greenside, P.G., Sinnott-Armstrong, N.A., Vesuna, S., Satpathy, A.T., Rubin, A.J., Montine, K.S., Wu, B., et al. (2017). An improved ATAC-seq protocol reduces background and enables interrogation of frozen tissues. Nat. Methods *14*, 959–962. https://doi.org/10.1038/nmeth.4396.

100. Buenrostro, J.D., Giresi, P.G., Zaba, L.C., Chang, H.Y., and Greenleaf, W.J. (2013). Transposition of native chromatin for fast and sensitive

epigenomic profiling of open chromatin, DNA-binding proteins and nucleosome position. Nat. Methods *10*, 1213–1218. https://doi.org/10.1038/nmeth.2688.

101. Bolger, A.M., Lohse, M., and Usadel, B. (2014). Trimmomatic: a flexible trimmer for Illumina sequence data. Bioinformatics Oxf. Engl. *30*, 2114–2120. https://doi.org/10.1093/bioinformatics/btu170.
102. Dobin, A., Davis, C.A., Schlesinger, F., Drenkow, J., Zaleski, C., Jha, S., Batut, P., Chaisson, M., and Gingeras, T.R. (2013). STAR: ultrafast universal RNA-seq aligner. Bioinformatics Oxf. Engl. *29*, 15–21. https://doi.org/10.1093/bioinformatics/bts635.
103. Zhang, Y., Liu, T., Meyer, C.A., Eeckhoute, J., Johnson, D.S., Bernstein, B.E., Nusbaum, C., Myers, R.M., Brown, M., Li, W., et al. (2008). Model-based analysis of ChIP-seq (MACS). Genome Biol. *9*, R137. https://doi.org/10.1186/gb-2008-9-9-r137.
104. Liao, Y., Smyth, G.K., and Shi, W. (2014). featureCounts: an efficient general purpose program for assigning sequence reads to genomic features. Bioinformatics Oxf. Engl. *30*, 923–930. https://doi.org/10.1093/bioinformatics/btt656.
105. Love, M.I., Huber, W., and Anders, S. (2014). Moderated estimation of fold change and dispersion for RNA-seq data with DESeq2. Genome Biol. *15*, 550. https://doi.org/10.1186/s13059-014-0550-8.
106. Lê, S., Josse, J., and Husson, F. (2008). FactoMineR: An R package for multivariate analysis. J. Stat. Soft. *25*. https://doi.org/10.18637/jss.v025.i01.
107. Xie, C., Mao, X., Huang, J., Ding, Y., Wu, J., Dong, S., Kong, L., Gao, G., Li, C.-Y., and Wei, L. (2011). KOBAS 2.0: a web server for annotation and identification of enriched pathways and diseases. Nucleic Acids Res. *39*, W316–W322. https://doi.org/10.1093/nar/gkr483.
108. Korotkevich, G., Sukhov, V., Budin, N., Shpak, B., Artyomov, M.N., and Sergushichev, A. (2016). Fast gene set enrichment analysis. Preprint at bioRxiv. https://doi.org/10.1101/060012.
109. Subramanian, A., Tamayo, P., Mootha, V.K., Mukherjee, S., Ebert, B.L., Gillette, M.A., Paulovich, A., Pomeroy, S.L., Golub, T.R., Lander, E.S., et al. (2005). Gene set enrichment analysis: a knowledge-based approach for interpreting genome-wide expression profiles. Proc. Natl. Acad. Sci. USA *102*, 15545–15550. https://doi.org/10.1073/pnas.0506580102.
110. Zambelli, F., Pesole, G., and Pavesi, G. (2009). Pscan: finding over-represented transcription factor binding site motifs in sequences from co-regulated or co-expressed genes. Nucleic Acids Res. *37*, W247–W252. https://doi.org/10.1093/nar/gkp464.
111. Castro-Mondragon, J.A., Riudavets-Puig, R., Rauluseviciute, I., Lemma, R.B., Turchi, L., Blanc-Mathieu, R., Lucas, J., Boddie, P., Khan, A., Manosalva Pérez, N., et al. (2022). JASPAR 2022: the 9th release of the open-access database of transcription factor binding profiles. Nucleic Acids Res. *50*, D165–D173. https://doi.org/10.1093/nar/gkab1113.
112. Bentsen, M., Goymann, P., Schultheis, H., Klee, K., Petrova, A., Wiegandt, R., Fust, A., Preussner, J., Kuenne, C., Braun, T., et al. (2020). ATAC-seq footprinting unravels kinetics of transcription factor binding during zygotic genome activation. Nat. Commun. *11*, 4267. https://doi.org/10.1038/s41467-020-18035-1.
113. Kulakovskiy, I.V., Vorontsov, I.E., Yevshin, I.S., Sharipov, R.N., Fedorova, A.D., Rumynskiy, E.I., Medvedeva, Y.A., Magana-Mora, A., Bajic, V.B., Papatsenko, D.A., et al. (2018). HOCOMOCO: towards a complete collection of transcription factor binding models for human and mouse via large-scale ChIP-seq analysis. Nucleic Acids Res. *46*, D252–D259. https://doi.org/10.1093/nar/gkx1106.
114. Hecker, D., Behjati Ardakani, F., Karollus, A., Gagneur, J., and Schulz, M.H. (2023). The adapted Activity-By-Contact model for enhancer-gene assignment and its application to single-cell data. Bioinformatics Oxf. Engl. *39*, btad062. https://doi.org/10.1093/bioinformatics/btad062.
115. Frankish, A., Diekhans, M., Jungreis, I., Lagarde, J., Loveland, J.E., Mudge, J.M., Sisu, C., Wright, J.C., Armstrong, J., Barnes, I., et al. (2021). GENCODE 2021. Nucleic Acids Res. *49*, D916–D923. https://doi.org/10.1093/nar/gkaa1087.
116. Grant, C.E., Bailey, T.L., and Noble, W.S. (2011). FIMO: scanning for occurrences of a given motif. Bioinformatics Oxf. Engl. *27*, 1017–1018. https://doi.org/10.1093/bioinformatics/btr064.
117. Bailey, T.L., and Grant, C.E. (2021). SEA: Simple Enrichment Analysis of motifs. Preprint at bioRxiv. https://doi.org/10.1101/2021.08.23.457422.
118. Kheradpour, P., and Kellis, M. (2014). Systematic discovery and characterization of regulatory motifs in ENCODE TF binding experiments. Nucleic Acids Res. *42*, 2976–2987. https://doi.org/10.1093/nar/gkt1249.
119. Lelong, S., Zhou, X., Afrasiabi, C., Qian, Z., Cano, M.A., Tsueng, G., Xin, J., Mullen, J., Yao, Y., Avila, R., et al. (2022). BioThings SDK: a toolkit for building high-performance data APIs in biomedical research. Bioinformatics Oxf. Engl. *38*, 2077–2079. https://doi.org/10.1093/bioinformatics/btac017.
120. Wu, C., Macleod, I., and Su, A.I. (2013). BioGPS and MyGene.info: organizing online, gene-centric information. Nucleic Acids Res. *41*, D561–D565. https://doi.org/10.1093/nar/gks1114.
121. Xin, J., Mark, A., Afrasiabi, C., Tsueng, G., Juchler, M., Gopal, N., Stupp, G.S., Putman, T.E., Ainscough, B.J., Griffith, O.L., et al. (2016). High-performance web services for querying gene and variant annotation. Genome Biol. *17*, 91. https://doi.org/10.1186/s13059-016-0953-9.
122. Quinlan, A.R., and Hall, I.M. (2010). BEDTools: a flexible suite of utilities for comparing genomic features. Bioinformatics Oxf. Engl. *26*, 841–842. https://doi.org/10.1093/bioinformatics/btq033.
123. Dale, R.K., Pedersen, B.S., and Quinlan, A.R. (2011). Pybedtools: a flexible Python library for manipulating genomic datasets and annotations. Bioinformatics Oxf. Engl. *27*, 3423–3424. https://doi.org/10.1093/bioinformatics/btr539.

STAR★METHODS

KEY RESOURCES TABLE

REAGENT or RESOURCE	SOURCE	IDENTIFIER
Antibodies		
Anti-VE Cadherin	Abcam	Cat#33168; LOT:GR3427140-1; RRID: AB_870662
Anti-CD31	BD Bioscience	Cat#555444; LOT:8157637; RRID: AB_395837
Anti-Ki67 RB705	BD Bioscience	Cat#570281; RRID: AB_3685636
Anti-Ki67	Abcam	Cat#ab15580; RRID: AB_443209
Anti-Ki67	eBioscience, Invitrogen	Cat#14-5698-82; RRID: AB_10854564
Alexa Fluor 546 Phalloidin	Thermo Fisher Scientific	Cat#A22283; LOT:2301063; RRID: AB_2632953
APC anti-mouse CD144	BioLegend	Cat#138012; clone BV13; RRID: AB_10680420
APC anti-human CD144	BioLegend	Cat#348507; RRID: AB_10639861
B-ACTIN	Santa Cruz	Cat#sc-69879; LOT:K1522; RRID: AB_1119529
eIF2α	Cell Signaling Technology	Cat#5324S; RRID: AB_10692650
ERG1	Abcam	Cat#ab92513; RRID: AB_2630401
ERG- Alexa Fluor 647	Abcam	Cat#ab196149; RRID: AB_3697463
CYCLIN A2 (BF683)	Cell Signaling Technology	Cat#4656T; RRID: AB_2071958
CYCLIN B1 (D5C10)	Cell Signaling Technology	Cat#12231T; RRID:AB_2783553
CYCLIN D1	Abcam	Cat#ab16663; RRID: AB_443423
CYCLIN E1	Cell Signaling Technology	Cat#4129T; RRID: AB_2071200
Donkey anti-Rabbit Alexa Fluor 488	Thermo Fisher Scientific	Cat#A-21206; LOT:2289872; RRID: AB_2535792
Donkey anti-Rabbit Alexa Fluor 647	Thermo Fisher Scientific	Cat#A-31573; LOT:2359136; RRID: AB_2536183
CSE	Proteintech	Cat#12217-1-AP; RRID: AB_2087497
Fibronectin antibody (FITC)	Fitzgerald	Cat#60-S1104GND1-AF-22; RRID: AB_11202814
GAPDH	Santa Cruz	Cat#sc-47724; LOT:K2222; RRID: AB_627678
GCN2	Cell Signaling Technology	Cat#65981S
GCN5	Proteintech	Cat#66575-1; RRID: AB_2881935
Goat anti-mouse IgG, H&L Chain Specific Peroxidase	Merck Milipore	Cat#401253; RRID: AB_437779
Goat anti-rabbit Alexa Fluor 647	Invitrogen	Cat#A31573; RRID: AB_2536183
Goat anti-mouse Alexa Fluor 488	Invitrogen	Cat#A21206; RRID: AB_2535792
Goat anti-Rabbit IgG, H&L Chain Specific Peroxidase	Merck Millipore	Cat#401393; RRID: AB_10683386
Griggonia Simplificolia Lectin I	Vector Laboratories	Cat#FL-1201-.5; RRID: AB_2314663
HAT1	Cell Signaling Technology	Cat#15348S
Histone H3	Cell Signaling Technology	Cat#9715S; LOT:23; RRID: AB_331563
H2AK5ac	Abcam	Cat#ab1764; RRID: AB_10563138
H3K9ac	Abcam	Cat#ab4441; RRID: AB_2118292
H3K9ac	Active Motif	Cat#39017; LOT:23088181-13; RRID: AB_2616593
H3K14ac	Cell Signaling Technology	Cat#7627T; LOT:6; RRID: AB_10839410

(*Continued on next page*)

Continued

REAGENT or RESOURCE	SOURCE	IDENTIFIER
H3K18ac	Active Motif	Cat#397755; ; RRID: AB_2714186
H3K23ac	Active Motif	Cat#39131; RRID: AB_2793165
H3K27ac	Abcam	Car#ab177178; RRID: AB_2828007
H3K27ac	Active Motif	Car#39685; RRID: AB_2793305
H3K4me3	Diagenode	Cat#C15410003; RRID: AB_2924768
H3K4me3	Active Motif	Cat#39159; RRID: AB_2615077
Isolectin GS-IB4-A647	Thermo Fisher Scientific	Cat#I32450; LOT:2591221; SCR_014365
PDHA1	Abcam	Cat#ab125602; RRID: AB_3698302
PDHA1	Invitrogen	Cat#PA5-21536; RRID: AB_11152360
Phospho-eIF2α (Ser51)	Cell Signaling Technology	Cat#3597S; LOT:12; RRID: AB_390740
Phospho-GCN2 (Thr899)	Cell Signaling Technology	Cat#94668S; LOT:1
Phospho-Rb (Ser 807/811)	Cell Signaling Technology	Cat#8516T; RRID: AB_11178658
Phospho-S6 Ribosomal Protein (Ser235/236)	Cell Signaling Technology	Cat#4857S; LOT:14; RRID: AB_2181035
Rat anti mouse CD144	BD Bioscience	Cat#555289; LOT:1076252; RRID: AB_395707
Rat anti mouse CD31	BD Bioscience	Cat#553370; LOT:1005853; RRID: AB_394816
SLC7A11 Polyclonal Antibody	Invitrogen	Cat#PA1-16893; RRID: AB_2286208
SLC7A11	Thermo Fisher Scientific	Cat#PA1-16893; LOT:XJ3734346A; RRID: AB_2286208
SLC7A11	Thermo Fisher Scientific	Cat#MA5-35360; LOT:XI3708804; RRID: AB_2849261
SLC7A11/xCT	Proteintech	Cat#26864-1-AP; LOT:00100100; RRID: AB_2880661
S6 Ribosomal Protein	Cell Signaling Technology	Cat#2217S; LOT:10; RRID: AB_331355
Vinculin	Thermo Fisher Scientific	Cat#MA5-11690; RRID: AB_10976821
Vimentin	Novocastra	Cat#NCL-L-VIM-V9; RRID: AB_564055
Wheat Germ Agglutinin	Invitrogen	Cat#w21405
Chemicals, peptides, and recombinant proteins		
13C3-L-Cysteine	Cambridge Isotope Laboratories	Cat#CLM-4320-H-0.1
13C6-34S-Cystine	Cambridge Isotope Laboratories	Cat#CSLM-11349-PK (Custom synthesis)
13C6-Glucose	Sigma-Aldrich	Cat#389274
34S-methionine	Santa Cruz	Cat#1006386-95-3
5-Ethyl-2-deoxyuridin	Sigma-Adlrich	Cat#900584
5x SuperScript IV RT Reaction Buffer	Invitrogen	Cat#18090050B
accutase	Sigma-Aldrich	Cat#A6964
Albumin, Bovine Serum, Fraction V, Fatty Acid-Free, Nuclease- and Protease-Free	Sigma-Aldrich	Cat#126609
Anti-HA-tag magnetic beads	MBL	Cat#M180-11
Antipain	Applichem	Cat#A2129,0010
Aprotinin	Applichem	Cat#A2132,0010
BD Pharmingen FITC Annexin V Apoptosis Detection Kit I	BD Bioscience	Cat#556547
Bioanalyzer High Sensitivity DNA analysis	Agilent Technologies	Cat#5067-4626
Blue S'Green qPCR kit	Biozym	Cat#331416
BODIPY 581/591 C11	Thermo Fisher Scientific	Cat#D3861
BSA	Sigma Aldrich	Cat#A1470-100G
BSA	Gibco	Cat#15260037
ChemiDoc Imaging System	Bio-Rad	Cat#12003153
chloroform	Carl Roth	Cat#7331.2

(*Continued on next page*)

Continued

REAGENT or RESOURCE	SOURCE	IDENTIFIER
Chymostatin	Applichem	Cat#A2144,0010
Clarity Western ECL Substrate	Bio-Rad	Cat#1705061
Collagen I, Rat tail	Corning	Cat#354236
collagenase type I	Thermo Fisher Scientific	Cat#C1-22-1G
Concanavalin A Beads	Polyscience	Cat#86057-3
custom formulated DMEM/F-12	Gibco	NA
CUTANA pAG-MNase	EpiCypher	Cat#15-1016
Cycloheximide	Sigma-Aldrich	Cat#C4859
DAPI	Sigma-Aldrich	Cat#D9542
D-glucose	Carl Roth	Cat#HN06.3
D-mannitol	Merck	Cat#M9546
D-sucrose	Merck	Cat#S7903
Direct red 80	Sigma-Aldrich	Cat#365548
Distilled water	Gibco	Cat#15230162
Dispase II	Roche Diagnostics	Cat#58817100
DMEM 1X	Gibco	Cat#41966-029
DMEM/F12	Gibco	Cat#21041-025
DMEM/F12 cystine/cysteine depleted medium	Genaxxon	Cat#C4018.0500
DMEM/F12 L-glutamine/ glucose depleted medium	Genaxxon	Cat#C4022.0500
DMSO (Dimethylsulfoxide)	Sigma-Aldrich	Cat#D2438
DNase	Roche	Cat#11284932001
Dnase/RNAse free water	Invitrogen	Cat#10977-035
dNTPs	Bioline	Cat#BIO-39026
donkey serum	Sigma-Aldrich	Cat#S30-100ML
DTT	Thermo Fisher Scientific	Cat#707265ML
Dynabeads sheep anti-rat IgG	Thermo Fisher Scientific	Cat#11035
DynaMag-2 Magnet	Thermo Fisher Scientific	Cat#12321D
Endothelial Cell Growth Medium -2 (ECGM-2)	Promocell	Cat#C-22011
ECGF Bovine (Crude Extract, cell culture grade) + Heparin (Endothelial cell growth factor)	Pelobiotech	Cat#PB-ECGF-1 Heparin
EDTA Dinatriumsalz-Dihydrat	Applichem	Cat#A1104,0250
EGTA	Merck	Cat#3777-10G
Erastin	Cayman Chemicals	Cat#17754
Fibronectin	Merck	Cat#11080938001
fixable viability stain 510	BD Bioscience	Cat#564406
fluorescent mounting media	Invitrogen	Cat#00-4958-02
Fetal bovine serum	Gibco	Cat#10500064; LOT:2563339
GCN2iB	MCE	Cat#HY-112654
Glycerol	Merck	Cat#G5516
Hanks' balanced salt solution	Sigma	Cat#H6648
HCl	Roth	Cat#X896.2
HEPES	Sigma-Aldrich	Cat#H0887
Hydrocortisone	Sigma	Cat#H088
IKE	Cayman Chemicals	Cat#27088
isoflurane	CP-Pharma	Cat#GK140K23A
isopropanol	Carl Roth	Cat#AE73.2

(*Continued on next page*)

Continued

REAGENT or RESOURCE	SOURCE	IDENTIFIER
L-Ascorbic acid	Carl Roth	Cat#3525.1
L-cysteine	Sigma Aldrich	Cat#C7352-25G
L-cystine	Sigma Aldrich	Cat#C7602
Leupeptin	Applichem	Cat#A2183,0010
L-glutamine	Gibco	Cat#25030-024
lipofectamine RNAiMAX Transfection Reagent	Thermo fisher scientific	Cat#13778150
L-methionine	Serva	Cat#28821
Magnesium Chloride	Merck	Cat#M4880
Medium 199	Sigma-Aldrich	Cat#M0650
Methyl cellulose	Sigma-Aldrich	Cat#M0512
NP-40	Thermo fisher scientific	Cat#85124
Protein A Sepharose 4 Fast Flow	Cytiva	Cat#17528001
Sodium Bicarbonate	Gibco	Cat#25080
okadaic acid sodium salt	LC laboratories	Cat#O-5857
Opti-MEM	Gibco	Cat#11058021
orthovandate	Merck	Cat#S6508
Penicillin-Streptomycin (10,000 U/mL)	Gibco	Cat#15140122
Pepstatin	Applichem	Cat#A2205,0010
PMSF	Thermo Fisher Scientific	Cat#36978
Polybrene	Santa Cruz	Cat#28728-55-4
Potasium Chloride	Merck	Cat#P4504
Propidium Iodide	Miltenyi Biotec	Cat#130-093-23
Protein G Sepharose 4 Fast Flow	Cytiva	Cat#17061801
Puromycin	Invivogen	Cat#ant-pr-5
Randon Primers	Promega	Cat#C118A
Recombinant human EGF	Peprotech	Cat#AF-100-15
Recombinant human FGF basic	Preprotech	Cat#100-18B
Recombinant human IGF-I	Peprotech	Cat#100-11
Recombinant human VEGF-165	Peprotech	Cat#3525.1
Recombinant mouse EGF	Peprotech	Cat#315-09
Recombinant mouse FGF basic	Peprotech	Cat#450-33
Recombinant mouse IGF-I	Peprotech	Cat#250-19
Recombinant murine VEGF-165	Peprotech	Cat#450-32
RNeasy Plus Universal Mini Kit	QIAGEN	Cat#73404
ROTI Block	Carl Roth	Cat#A151.3
SDS	Merck	Cat#L3771-1KG
Sodium Bicarbonate	Gibco	Cat#25080-060
Sodium Chloride	Merck	Cat#S9888
Sodium Pyruvate	Gibco	Cat#11360-039
SUPERase-In RNAse inhibitor	Thermo Fisher Scientific	Cat#AM2696
SuperScript IV Reverse Transcriptase	Thermo Fisher Scientific	Cat#18090010
Tamoxifen	Merck	Cat#10540-29-1
Tissue-Tek O.C.T. Compound	Sakura	Cat#4583
TRIS	Roth	Cat#AE15.3
Triton X-100	Sigma-Aldrich	Cat#9002-93-1
Trizol	QIAGEN	Cat#79306
trypsin	Biochrom	Cat#L2103-20G
Trypsin-Inhibitor	Applichem	Cat#A1441,0250

(*Continued on next page*)

Continued

REAGENT or RESOURCE	SOURCE	IDENTIFIER
TURBO DNAseI	Thermo Fisher Scientific	Cat#AM223
U-13C16-palmitic acid	Cambridge Isotope Laboratories	Cat#CLM-309-PK
Critical commercial assays		
Chromatin IP DNA Purification Kit	Active Motif	Cat#58002
Click-iT EdU Cell Proliferation Kit for Imaging, Alexa Fluor 488 dye	Thermo Fisher Scientific	Cat#C10337
DyLight 405 Conjugation kit	Novus Biologicals	Cat#ab201798
EZ:faast GC-MS Physiological, Amino Acid Analysis Kit	Phenomenex	Cat#KG0-7166
FITC Annexin V Apoptosis Detection Kit I	BD Pharmingen	Cat#556547
Illumina Tagment DNA TDE1 Enzyme and Buffer Large Kit	Illumina	Cat#20034198
MycoStrip – Mycoplasma Detection Kit	Invivogen	Cat#rep-mys-10
QIAquick PCR Purification Kit	QIAGEN	Cat#28104
SMARTer Stranded Total RNA Sample Prep Kit HI Mammalian	Takara Bio	Cat#634873
ThruPLEX DNA-Seq Kit	Takara Bio	Cat#R400674
VAHTS Universal Stranded mRNA-seq - V6	Vazyme	Cat#NR604
Zymo ChIP DNA Clean and concentrator Kit	Zymo Research	Cat#D5205
Deposited data		
RNA-seq data	This paper	GEO: GSE305819
ATAC-seq data	This paper	GEO: GSE305823; GSE305822
Ribotag-seq data	This paper	GEO: GSE305827
CUT&RUN/Act-seq data	This paper	GEO: GSE305820; GSE305824; and GSE305826
Proteomics data	This paper	PRIDE: PXD068385
Raw data	This paper	Data S1
Experimental models: Cell lines		
Human: umbilical vein endothelial cells (HUVEC)	Lonza Promocell	Cat#C2519A; #C2517; #00191027; Cat#C12203; #C12200; #C12205
Human: 293	American Type Culture Collection (ATCC)	Cat#CRL-1573
Lenti-XTM HEK 293T	Takara	Cat#632180
Experimental models: Organisms/strains		
SLC7A11$^{fl/fl}$xPdgfb-CreERT2	Shanghai model Organisms And The Jackson Laboratory	C57BL/6Smoc-Slc7a11em1(flox)Smoc: Cat#NM-CKO-2117850B6.Cg-Tg(Pdgfrb-cre/ERT2)6096Rha/J: Cat#029684
PdgfbCreERT2	The Jackson Laboratory	B6.Cg-Tg(Pdgfrb-cre/ERT2)6096Rha/J; Strain#029684
CSE$^{fl/fl}$xPdgfb-CreERT2	This paper	N/A
CSE$^{fl/fl}$xCdh5-CreERT2	https://doi.org/10.1161/CIRCULATIONAHA.118.034757	N/A
FUCCI	Riken Bioresource research center	B6.Cg-Tg(FUCCIS/G2/M)#504BsiTg (FUCCIG1)#596Bsi; Cat#RBRC02892
WT mice (C57BL/6JRj)	Janvier Labs	C57BL/6JRj Mouse - Janvier Labs
Recombinant DNA		
pCDH-CMV-3xFlag–human-ATF4-copGFP	Synthetized by Genomeditech, Shanghai, China	N/A
pCDH-CMV-3xFlag–human-CSE-copGFP	Synthetized by Genomeditech, Shanghai, China	N/A
pCDH-CMV-3xFlag–human-SLC7A11-copGFP	Synthetized by Genomeditech, Shanghai, China	N/A

(*Continued on next page*)

Continued

REAGENT or RESOURCE	SOURCE	IDENTIFIER
pCDH-CMV-3xFlag-copGFP	Synthetized by Genomeditech, Shanghai, China	N/A
LentiCRISPR_v2	Addgene	RRID: Addgene_52961
PDHA1-NES construct	Genomeditech, Shanghai, China	N/A
pMD2.G	Addgene	RRID: Addgene_12259
psPAX2	Addgene	RRID: Addgene_12260
pLentiCRISPR_v2_P53	https://doi.org/10.1161/CIRCRESAHA.123.323084	NA
pLentiCRISPR_v2_NTC	https://doi.org/10.1161/CIRCRESAHA.123.323084	N/A
adCSE-GFP track	https://doi.org/10.1161/CIRCRESAHA.123.323084	N/A
Empty adRFP track	Addgene	RRID: Addgene_12520
pCDH-CMV-Ribotag (RPL22-3xHA)-EF1-Puro-NM-000983.4	Synthetized by Genomeditech, Shanghai, China	N/A
mcherry-hCdt1(30/120)pCSII-EF	Riken Bioresource research center	Cat#RDB15273
mAG-hGeminin(1/110)/pCSII-EF	Riken Bioresource research center	Cat#RDB15268
Oligonucleotides		
Primer for mDll4 Forward: TTTGCTCTCCCAGGGACTCT	Biospring	N/A
Primer for mDll4 Reverse: AGGCTCCTGCCTTATACCTCT	Biospring	N/A
Primer for mHes1 Forward: AATTCCTCGTCCCCGGTGGCT	Biospring	N/A
Primer for mHes1 Reverse: CTTGGAATGCCGCGAGCTATCTT	Biospring	N/A
Primer for mHey1 Forward: TCGGCTCTAGGTTCCATGTCCCC	Biospring	N/A
Primer for mHey1 Reverce: AGCTTAGCAGATCCCTGCTTCTCAA	Biospring	N/A
Primer for 18s Forward: CTTTGGTCGCTCGCTCCTC	Biospring	N/A
Primer for 18s Reverse: CTGACCGGGTTGGTTTTGAT	Biospring	N/A
Primer for hSLC7A11 Reverse: TCAGAATTGCTGTGAGCTTGCA	Biospring	N/A
Primer for hSLC7A11 Forward: CCTGGCATTTGGACGCTACAT	Biospring	N/A
Primer for hCTH Reverse: GCCAAAGGGCGCTTGGTTT	Biospring	N/A
Primer for hCTH Forward: ACTTCAGGCAAGTGGCATCTG	Biospring	N/A
Single guide RNA against TP53 antisense: AAACTCGCTATCTGAGCAGCGCTCC	Biospring	N/A
Single guide RNA against TP53 sense: CACCGGAGCGCTGCTCAGATAGCGA	Biospring	N/A
Single guide RNA non-targeting control antisense: AAACAGGACTTGTTAGCCCGGAAC	Biospring	N/A
Single guide RNA non-targeting control sense:CACCGTTCCGGGCTAACAAGTCCT	Biospring	N/A
siRNA targeting sequence: CSE: UUCUUCGAACGUGGCACGAdTdT	Eurogentec	N/A

(*Continued on next page*)

Continued

REAGENT or RESOURCE	SOURCE	IDENTIFIER
siRNA duplex negative control	Eurogentec	Cat#SR-CL000-005
siRNA targeting SLC7A11 siRNA	Horizon Discovery	Cat#E-007612-00-0005; LOT#221102
siRNA Non-targeting control pool	Horizon Discovery	Cat#D-001910-10
Software and algorithms		
AlphaFold 3	https://doi.org/10.1038/s41586-024-07487-w	https://alphafoldserver.com/about
AutoDock	https://doi.org/10.1093/nar/gkac394	https://autodock.scripps.edu/
Bowtie2	https://doi.org/10.1038/nmeth.1923	http://bowtie-bio.sourceforge.net/bowtie2/index.shtml
Deeptools (version 3.3.1)	https://doi.org/10.1093/nar/gku365	https://imagej.nih.gov/ij/
FIMO	https://doi.org/10.1093/ bioinformatics/btr064	https://github.com/liuchengwucn/FIMO
Fiji	https://doi.org/10.1038/nmeth.2019	https://imagej.net/software/fiji/
FlowJo (version 9.0)	BD Bioscience	https://www.flowjo.com
GENCODE	https://doi.org/10.1093/nar/gkaa1087	https://github.com/abiliogp/genCode
GraphPad Prism	GraphPad	https://www.graphpad.com
GSEA msigdb collection h/c2	https://doi.org/10.1073/pnas.0506580102	https://www.gsea-msigdb.org/gsea/msigdb/human/collections.jsp
ImageJ	https://doi.org/10.1038/nmeth.2089	https://imagej.nih.gov/ij/
Image Lab Software	Bio Rad	https://www.bio-rad.com/de-de/product/image-lab-software?ID=KRE6P5E8Z
Incucyte Base Software	Essen Bioscience	https://www.essenbioscience.com/en/products/incucyte/
HOCOMOCO (version 11)	https://doi.org/10.1093/nar/gkx1106	https://github.com/GabrielHoffman/tfbsDB
JASPAR (2022)	https://doi.org/10.1093/nar/gkab1113	http://jaspar.genereg.net/
Kobas	https://doi.org/10.1093/nar/gkr483	https://github.com/xmao/kobas
MACS (version 3.0.1)	https://doi.org/10.1186/gb-2008-9-9-r137	https://github.com/macs3-project/MACS
Metaboanalyst 5.0	https://doi.org/10.1093/nar/gkp356	https://www.metaboanalyst.ca
MultiQuant v.3.0	Sciex	https://sciex.com
MyGene.info	https://doi.org/10.1186/s13059-016-0953-9	https://github.com/biothings/mygene.info
Picard (version 3.1.1)	Broad Institute	https://broadinstitute.github.io/picard/
ProteoWizard msconvert	ProteoWizard	https://proteowizard.sourceforge.io/
Pscan	https://doi.org/10.1093/nar/gkp464	https://pscan.uk/install/windows.html
R (version 44.1)	R studio	https://github.com/rstudio
R package: bedtools (version 2.31.1)	https://doi.org/10.1093/bioinformatics/btq033	https://github.com/arq5x/bedtools2
R Package: DESeq2 (version 1.27.32)	https://doi.org/10.1186/s13059-014-0550-8	http://bioconductor.org/packages/release/bioc/html/DESeq2.html
R package: FactoMineR	https://doi.org/10.18637/jss.v025.i01	https://cran.r-project.org/web/packages/FactoMineR/index.html
R package: featureCounts (version 1.6.5)	https://doi.org/10.1093/bioinformatics/btt656	https://rnnh.github.io/bioinfo-notebook/docs/featureCounts.html
R package: fGSEA	https://doi.org/10.1101/060012	https://bioconductor.org/packages/release/bioc/html/fgsea.html
R package: pybedtools (version 0.8.1)	https://doi.org/10.1093/bioinformatics/btr539	https://pypi.org/project/pybedtools/
R package: samtools (version 1.9)	https://doi.org/10.1093/bioinformatics/btp352	https://bioconductor.org/packages/release/bioc/html/Rsamtools.html
SEA	https://doi.org/10.1101/2021.08.23.457422	https://github.com/ecnu-sea/SEA
Spectronaut software	Spectronaut 14.4.200727.47784	N/A
STAR (version 2.7.3a)	https://doi.org/10.1093/bioinformatics/bts635	https://github.com/alexdobin/STAR

(*Continued on next page*)

Continued

REAGENT or RESOURCE	SOURCE	IDENTIFIER
STARE (version 1.0.4)	https://doi.org/10.1093/bioinformatics/btad062	https://github.com/SchulzLab/STARE
Tobias footprinting motif analysis	https://doi.org/10.1038/s41467-020-18035-1	N/A
Trimmomatic (version 0.39)	https://doi.org/10.1093/bioinformatics/btu170	https://github.com/usadellab/Trimmomatic
ZEN Black	Zeiss	https://www.micro-shop.zeiss.com/de/de/softwarefinder/software-categories/zen-black/zen-black-desk/
ZORBAX Extend RR HD 1.8μm column	Agilent Technologies	ZORBAX Reversed-Phase HPLC Columns | Buy Online | Agilent
Agilent 1290 Infinity LC system	Agilent Technologies	https://www.agilent.com/en/product/liquid-chromatography/hplc-systems/analytical-hplc-systems/1290-lc-system

EXPERIMENTAL MODEL AND SUBJECT DETAILS

Mice

Housing conditions and regulations

Mice were housed in conditions that conform to the guide for the care and use of Laboratory Animals published by the U.S. National Institutes of Health (NIH publication no. 85-23). Animals received the usual laboratory diet or subjected to caloric restriction as previously described.[51] All studies were approved by the animal research ethic committee in Darmstadt and Karlsruhe (G-60/24, FU1250, FU2077) or Tongji Medical College, Wuhan.

Animal strains

CSE (fl/fl) mice were generated as previously described[86] and SLC7A11 fl/fl were generated from Shanghai model Organisms (C57BL/6Smoc-Slc7a11em1(flox)Smoc; # NM-CKO-2117850). CSE fl/fl were then crossed to the Cdh5CreERT2 deleter line as previously described[53] and both CSE and SLC7A11 fl/fl mice were crossed to the PdgfbCreERT2 deleter line (B6.Cg-Tg(Pdgfrb-cre/ERT2)6096Rha/J; # 029684, The Jackson Laboratory). SLC7A11 fl/fl x CSE fl/fl were generated from PdgbCreERT2 CSE fl/fl crossing with PdgbCreERT2 SLC7A11 fl/fl. FUCCI mice (B6.Cg-Tg(FUCCIS/G2/M)#504BsiTg(FUCCIG1)#596Bsi) were purchased from Riken Bioresource research center (#RBRC02892). Wild type mice C57BL/6 were purchased from Jackson laboratory (#000664).

Cell culture

Human umbilical vein endothelial cells (HUVEC, newborn age, male and female mixed sex, and single adult donors, #C2519A; #C2517; #00191027; Lonza; #C12203; #C12200; #C12205; Promocell)

Cells were cultured on fibronectin pre-coated surfaces (25 μg/mL) (#11080938001, Merck) in endothelial cell growth media 2 (ECGM-2) (#C-22011, Promocell) supplemented with heat-inactivated 5% fetal bovine serum (FBS) (#10500064, LOT:2563339, Gibco) and 0.5% penicillin-streptomycin (#15140122, Gibco).

Mouse lung endothelial cells (mLEC)

Endothelial cells were isolated as previously described[53,86] and mixed from male and female mice at age 8-12 weeks old, unless specified, as indicated in the specific experiments. Cells were cultured on fibronectin-coated surfaces (25 μg/mL) (#11080938001, Merck Millipore) in DMEM/F12 (#21041-025, Gibco) supplemented with sterile filtered Endothelial cell growth factor (#PB-ECGF-1 Heparin, Pelobiotech), 20% FBS and 0.5% penicillin-streptomycin (mLEC media).

HEK293 cells (#CRL-1573; ATCC)

HEK293 cells were grown in DMEM (#41966-029, Gibco) supplemented with 10% FBS and 0.5% penicillin-streptomycin.

Lenti-X HEK 293T cells *(HEK293T, #632180; Takara)*

Cells were cultured in DMEM/F12 supplemented with 10% FBS, 0.5% penicillin-streptomycin as previously described.[90]

All cells were incubated in 37°C, 5% CO2 tested for mycoplasma weekly using a mycoplasma detection kit (#rep-mys-10; Invivogen).

Human cohort

Plasma and human cells from mesenteric arteries were isolated from subjects of 20±2.3 and 80±3.4 years of age (previously published and ethically approved/SC55/22-2-2018 human cohort, with details provided in Hu et al.[6]). In brief, for the plasma isolation blood was collected in EDTA-treated tubes, centrifuged to isolate platelet-free plasma (2000 g, 15 minutes at 4°C) and the supernatant was stored at -80°C until further analysis. For the human mesenteric endothelial cell isolation, arteries were incubated with dispase II (5 Units/mL, # 58817100, Roche) for 20 minutes. Subsequently, cells were pelleted and labelled with anti-CD144 antibody (#348507; Biolegend) and subjected to FACS sorting with a BD FACSAria III (BD Biosciences, Germany) and either snap frozen in

liquid N2 until evaluation, or cryopreserved in 10% DMSO in ECGM-2 media for functional analyses. Cells were cultured similarly to the human umbilical vein endothelial cells for only one passage.

METHOD DETAILS

Mice and treatments

The allocation of animals to the different treatment groups was blinded to the investigator and was revealed only after the data had been analyzed. Animals were randomized using the block randomization method to ensure similar sample sizes per age and sex matched group. In case of pup evaluation of the specific genotypes, all animals were used and genotyping was performed after the phenotypical analysis. Experiments were performed in a double blinded manner and no animals were excluded from the analysis.

Tamoxifen induction

For *in vivo* induction of CSE and/or SLC7A11 endothelial cell specific deletion, pups at postnatal day 0 or 1 were injected intraperitoneally for 3 consecutive days with 1 mg/kg tamoxifen (#10540-29-1, Merck) dissolved in corn or peanut oil. Induction in the murine embryos was achieved with 1 mg/kg tamoxifen administration with oral gavage to the pregnant mice from embryonic day (E) E9.5 and for three consecutive days. Adult mice were induced as previously described.[53] In brief, to induce Cre activity, tamoxifen (75 mg/kg) was administered intraperitoneal (i.p.) for 5 consecutive days and sufficient knock down was achieved 7 days post-injection.

EdU injections

5-Ethyl-2-deoxyuridin (EdU) (#900584, Sigma-Aldrich) injections were performed as previously described,[6] 4 hours prior to sacrifice. Littermates of both genders were used.

Intravitreal injections

Intravitreal injections were performed in postnatal day 4 of WT mice as described before.[91] In each mouse, one eye was injected with 0.5 μL solvent (1% DMSO in 0.9% NaCl) and the contralateral eye with 1 mmol/L of L-Cystine (#C7602, Sigma Aldrich) or 1 mmol/L Na_2S_3 (#SB03-10, Dojindo). The injections were performed using an Ultramicropump III injector (World Precision Instruments) with self-pulled glass pipettes at a rate of 10 nL/second and continuously monitored with the aid of a stereo microscope.

Aortic regeneration model in vivo

Abdominal aortic injury in old (18 month) mice was induced as previously described.[6] In particular, the aortic injury was surgically induced with the dissection of the surrounding tissue from the abdominal aorta and the applying of a vascular clamp (width: 800 μm) for 60 seconds, in order to result in loss of the endothelial lining at that location. The abdomen was then closed. Mice received 100 mg/kg/day cystine in the drinking water (#C7602, Sigma Aldrich) starting 24 hours prior and for 72 hours after injury. To visualize endothelial cell proliferation mice were injected 4 hours prior to sacrifice with EdU (50 mg/Kg, #900584, Sigma-Aldrich) and imaging was performed as described below in "Immunofluorescence and EdU staining: Immunofluorescence of whole mount aortae".

Retinopathy of prematurity model

The oxygen-induced retinopathy was performed as previously described.[91,92] In brief, the murine pups were born and grown from p0 and up to p7 in room air. Subsequently, together with their mothers were exposed to 75% O_2 using a ventilated chamber (Shanghai TOW Intelligent Technology Company) from p7 to p12 and then returned to room air from p12 to p17. Control pups were kept in room air for all time points. Mothers received either solvent or 100 mg/kg/day cystine in the drinking water (#C7602, Sigma Aldrich) in two groups from p7-p12 and from p12-p17. Animals were sacrificed at p17 and retinas were isolated for further validation (described in "Immunofluorescence and EdU staining: Immunofluorescence of whole mount retina").

Minimal-invasive myocardial infarction (MI)

Minimal-invasive myocardial infarction and subsequent echocardiographic analysis was performed in 8-10 week old mice as previously described.[39] Briefly, mice were anaesthetized with isoflurane (induction: 3% / 800 mL O_2, maintenance with respiratory mask: 1.5-2% / 800mL O_2). The coronary arteries of the heart were then visualized with a high-resolution ultrasound (VisualSonics, MS550 high resolution probe). After a neutral electrode was attached, a 26-gauge electrically insulated monopolar needle was guided by ultrasound through the side of the closed chest, past the dorsal lung and placed on the left descending artery (LAD). Subsequently, high-frequency alternating current from an electrosurgical unit was employed to sclerosed the LAD. The absence of blood flow distal of occlusion, regional akinesia and characteristic echocardiographic changes were used as indicators of a successful MI induction. Following successful occlusion, the needle was withdrawn, the mice were ventilated with pure oxygen until fully awake and then placed in a heated cage. Mice received either solvent (Sol.) or 50 mg/kg/day cystine in the drinking water one day prior and for up to 4 weeks post-surgery. Echocardiography was performed at different time points as indicated. All data were analyzed using VevoStrain software. Tissues were collected 4 weeks post-surgery, embedded in Tissue-Tek O.C.T. Compound (#4583; Sakura), cut in 7 μm cryo-slices using a cryotome and validated with histological and immunohistological analysis (described in "Immunofluorescence and EdU staining: Immunofluorescence of the murine heart and Sirius Red staining of the heart").

Small interfering RNA

Human umbilical vein endothelial cells were treated with control siRNA (30 – 50 pmol) (#D-001910-10, Horizon discovery) or siRNA directed against SLC7A11 (50 pmol) (#E-007612-00-0010, Horizon discovery), or siRNA directed against CSE (30 pmol) (sequence

UUCUUCGAACGUGGCACGAdTdT) (custom made, Eurogentec) 72 hours prior experimentation. Transfection was performed in Opti-MEM media (#11058021, Gibco) using the lipofectamine RNAiMAX Transfection Reagent (#13778150, Thermo Fisher Scientific) according to the manufacturer's instructions.

Generation of lentiviruses and transduction

Constructs

Constructs for ribotag virus (pCDH-CMV-Ribotag (RPL22-3xHA)-EF1-Puro-NM-000983.4), ATF4-3xFLag, SLC7A11-3xflag, CSEx3-flag (pCDH-CMV-3xflag-human-Protein of interest-ef1-copgfp-t2a-puro), 3xFlag control (pCDH-CMV-MCS-EF1α-copGEP-T3A-puro) and a PDHA1-NES construct (C terminal addition of the NES peptide: LQLPPLERLTLD) were synthetized by Genomeditech (Shanghai, China). FUCCI constructs of mcherry-hCdt1 (#RDB15273, mcherry-hCdt1(30/120)pCSII-EF) and mAG-Geminin (#RDB15268, mAG-hGeminin(1/110)/pCSII-EF) were purchased from Riken BRC Center (Ibaraki, Japan). Lenti backbone plasmids for psPAX2 (Addgene plasmid, #12260, https://www.addgene.org/12260/) and for pMD2.G (Addgene plasmid, #12259, https://www.addgene.org/12259/) were purchased from Addgene (Watertown, USA). Guide RNAs against human P53 were generated as previously described[6] (antisense: AAACTCGCTATCTGAGCAGCGCTCC and sense: CACCGGAGCGCTGCTCAGATAGCGA). In brief, gRNAs targeting human P53 were designed with an online tool (http://chochop.cbu.uib.no/) and were cloned into pLenti-CRISPRv2 (Addgene plasmid, #52961, https://www.addgene.org/52961/) co-expressing a Cas9 nuclease. Additionally, non-targeted control (NTC) (antisense: AAACAGGACTTGTTAGCCCGGAAC and sense: CACCGTTCCGGGCTAACAAGTCCT) was cloned into pLentiCRISPRv2 as previously described.[6]

Lentivirus generation and transduction

Lentiviruses were generated following HEK293T cell transfection, as previously described.[6] Briefly, HEK293T were allowed to seed (seeding dencity 40,000 cells/cm^2) in a 60 cm^2 cell culture plate 24 hours prior transfection in 9 mL DMEM/F12 (10% FBS, 1% penicillin-streptomycin) supplemented with 0.01 mol/L HEPES (#H0887, Sigma Aldrich). The plasmid of interest (4.1μg), psPAX2 (3.8μg) and pMD2.G (2.1μg) were mixed in 700 μL Opti-MEM media (#11058021, Gibco) (Mix A), while polyethylenamine (PEI, 50 μg, #408727, Sigma-Aldrich) was added in 650 μL Opti-MEM media (Mix B). Both Mix A and B were incubated for 5 minutes at RT, and then solution A was added to B, the mixture was incubated for 20 minutes at RT and added dropwise on the cells. The media was replaced 24 hours post transfection with fresh media containing 0.01 mol/L HEPES and the viruses were collected 72 hours later and filtered through a 0.45 μm sterile filter before adding to target cells. Subsequently, to generate a stable lentiviral cell line, HUVECs and human isolated aged endothelial cells (80 years) were plated in a density of 15,000 cells/cm^2 24 hours prior to transduction. The next day were transduced for 24 hours with 1:1 endothelial cell growth media: Viral volumes in the presence of 8 μg/mL polybrene (#28728-55-4, Santa Cruz). Lentiviral media was exchanged to endothelial cell growth media after 24 hours. If needed, cells were treated with 1 μg/μL puromycin (#ant-pr-5, Invivogen) to select positive transduced cells. Cells were allowed to recover after selection for additional 48 hours in ECGM-2 prior to other experiments.

CSE adenovirus generation and infection of mLEC

CSE adenovirus with a GFP track (adCSE) and an empty RFP track adenovirus were generated and used for infecting mLEC as previously described.[53] In brief, mouse endothelial cells were transduced with adCSE (10 MOI) or the empty RFP trackvirus in mLEC media for 24 hours. After 24 hours adenovirus was removed and media was changed to mLEC media. Positive transduced cells were observed under a fluorescence microscope by GFP or RFP expression. Cells were used 24 – 48 hours after adenovirus transduction for experiments.

Cell treatments

SLC7A11 inhibition

endothelial cells were treated with Solvent (Sol.) (DMSO, ##D2438, Sigma Aldrich) or with 10 μmol/L Imidazole Ketone Erastin (IKE, #27088, Cayman Chemicals), a selective SLC7A11 inhibitor (7A11i),[33] to prevent the uptake of cystine up to 24 hours.

Cystine deprivation in human endothelial cells

After 24 hours culture in ECGM-2, cells were washed twice with 1x DPBS with calcium and magnesium and then cultured in a custom DMEM/F12 cystine/cysteine depleted media (ΔCC) (#C4018.0500, Genaxxon) in the presence of 5 ng/mL recombinant human endothelial growth factor (#AF-100-15, Peprotech, Thermo Fisher Scientific), 10 ng/mL human basic fetal growth factor (#100-18B-50UG, Peprotech, Thermo Fisher Scientific), 20 ng/mL human insulin-like growth factor (#100-11-100UG, Peprotech, Thermo Fisher Scientific), 10 ng/mL recombinant human VEGF-165 (#100-20-1MG, Peprotech, Thermo Fisher Scientific), 1 μg/mL L-Ascorbic acid (#3525.1, Carl Roth), 1 μg/mL hydrocortisone (#50-23-7, Merck), 1 mg/mL sodium bicarbonate (#25080-060, Gibco), 10% FBS and 100 μmol/L L-methionine (#28821, Serva). In addition the control cystine/cysteine media (CC) was supplemented with 100 μmol/L sterile filtered L-cystine (#C7602, Sigma- Aldrich). As indicated for the specific experiments cells were either maintained in CC or ΔCC condition or 24 hours later cells were cultured again in ECGM-2 medium (Allev) for 24 hours.

Cystine deprivation in mouse endothelial cells

After 24 hours culture in mLEC media, cells were washed twice with 1x DPBS with calcium and magnesium and then were cultured in a custom formulated DMEM/F12 cystine/cysteine depleted media (ΔCC) (#C4018.0500, Genaxxon) in the presence of 5 ng/mL recombinant mouse endothelial growth factor (#315-09, Peprotech, Thermo Fisher Scientific), 10 ng/mL mouse basic fetal growth factor (#450-33, Peprotech, Thermo Fisher Scientific), 20 ng/mL mouse insulin growth factor I (#250-19, Peprotech, Thermo Fisher

Scientific), 10 ng/mL recombinant mouse VEGF-165 (#450-32, Peprotech, Thermo Fisher Scientific), 1 μg/mL L-Ascorbic acid (#3525.1; Carl Roth), 1 μg/mL hydrocortisone (#50-23-7; Merck), 1 mg/mL sodium bicarbonate (#25080-060; Gibco), 20% FBSand 100 μmol/L L-methionine (#28821, Serva). In addition the control cystine/cysteine media (CC) was supplemented with 100 μmol/L sterile filtered 100 μmol/L L-cystine (#C7602, Sigma- Aldrich).

GCN2 inhibition

Cells were pre-treated for 24 hours with 10 μmol/L GCN2iB (#HY-112654, MCE) in endothelial cell growth media. Subsequently, media was changed to the custom made ΔCC as described above supplemented with 10 μmol/L GCN2iB for 48 hours with refreshing the media after 24 hours.

Timecourse experiment

Endothelial cells non-transduced or lentivirally transduced with FUCCI virus were cultured in ECGM-2, in fibronectin coated plates, till 100% confluence. Subsequently cells were maintained for 10 days in contact inhibition (quiescent state, 0 hours) with regular medium change (every 1-2 days). The cells were re-seeded in low density to achieve proliferation and following adhesion (estimated 2 hours interval) cells were collected at the respective time points (2, 6, 12, 24 hours) for further analysis.

Immunoblotting

Whole-cell lysates were prepared in fresh RIPA buffer (150 mmol/L NaCl, 50 mmol/L Tris-HCl, 1% Triton X-100, #9002-93-1, Sigma-Aldrich, 0.5% sodium deoxycholate, 0.1% SDS) supplemented with protease and phosphatase inhibitors of 1% orthovandate (OA) (#S6508-50g, Merck), 1% okadaic acid sodium salt (OV) (#O-5857-1mg, LC laboratories), 0.8% Phenylmethylsulfonyl fluoride (PMSF) (#36978, Thermo Fisher Scientific), and 1.2% PIM (Antipain (#A2129,0010, Applichem), Aprotinin (#A2132,0010, Applichem), Chymostatin (#A2144,0010, Applichem), Leupeptin (#A2183,0010, Applichem), Pepstatin (#A2205,0010, Applichem), Trypsin-Inhibitor). Protein concentration was measured using the Bradford assay. Equal amounts of proteins were solubilized in 3x SDS sample buffer (25.5% glycerin, 6% SDS, 188 mmol/L Tris/HCl pH 6.8, 60 mmol/L DTT, 0.006% bromophenol blue) and separated in sodium dodecylsulfate-polyacrylamide gel electrophoresis and transferred onto a nitrocellulose membrane using the wet electroblotting system (Bio-Rad, Hercules, USA). Membranes were blocked in 1X ROTI Block (#A151.3 Carl Roth) and incubated with primary antibodies diluted in 1X ROTI Block over night at 4°C, followed by horseradish peroxidase-conjugated secondary antibody (1:10.000, #401393; #401253, Merck Milipore) incubation for 2 hours at room temperature. Proteins were visualized with Clarity Western ECL Substrate (#1705061, Bio-Rad) using the ChemiDoc Imaging System (BioRad, Hercules, USA) and the Image Lab software (BioRad, Hercules, USA). Western blot quantification was performed using ImageJ software Gel Analyzer function to generate the intensity profile of the selected bands. The background was subtracted and the generated peaks corresponding to each band where measured. The measures were normalized to the loading control and showed as fold change difference to a reference sample, unless specified different. All western blot results were included. Antibodies used for western blot are: GAPDH (1:1000, #sc-47724, Santa Cruz), β-ACTIN (1:1000, #sc-69879, Santa Cruz), VINCULIN (1:1000, # MA5-11690, Thermo Fisher Scientific), eIF2α (1:1000, #5324S, Cell Signaling Technology), pEIF2α^{Ser51} (1:1000, #3597S, Cell Signaling Technology), pS6$^{Ser235/236}$ (1:1000, #4857S, Cell Signaling Technology) S6 ribosomal protein (1:1000, #22170, Cell Signaling Technology), CSE (1:1000, #12217-1AP, Proteintech), SLC7A11/xCT (1:1000, #26864-1AP, Proteintech), GCN2 (1:1000, #65981S, Cell Signaling Technology), pGCN2^{Thr899} (1:1000, #94668s, Cell Signaling Technology), HAT1 (1:1000, #15348S, Cell Signaling Technology), GCN5 (1:1000, #66575-1, Proteintech), Goat Anti-Rabbit IgG Peroxidase Conjugate (#401393, Merck Milipore), Goat Anti-Mouse IgG Peroxidase Conjugate (#401253, Merck Milipore), CYCLIN D1 (1:1000, #ab16663, Abcam), CYCLIN A2 (BF683) (1:1000, #4656T, Cell Signaling Technology), CYCLIN B1 (D5C10) (1:1000, #12231T, Cell Signaling Technology), CYCLIN E1 (1:1000, #4129T, Cell Signaling), phospho-Rb (Ser 807/811) (1:1000, #8516T, Cell Signaling Technology), PDHA1 (1:1000, #ab125602, Abcam), H3 (1:1000, #9715, Cell Signaling Technology), H3K23ac (1:1000, #39131, Active Motif), H3K27ac (1:1000, #39685, Active Motif), H3K9ac (1:1000, #39017, Active Motif).

Mitochondria isolation

Mitochondria isolation was carried out as previously described[93,94] with modifications. In brief, cells were washed, scraped in ice cold 1x DPBS and centrifuged at 200 x g for 5 minutes at 4°C. The sample pellets were suspended in 1x M Buffer (220 mmol/L Mannitol, 70 mmol/L Sucrose, 5 mmol/L HEPES pH 7.4, 1 mmol/L EGTA) supplemented with 12 μL/mL PIM and homogenized using a pre-cooled glass homogenizer. The homogenate was transferred to a new tube and centrifuged twice at 800 x g for 5 minutes at 4°C to pellet nuclei and remaining intact cells. The supernatant was collected with a cut edge 1 mL-pipette tip and centrifuged at 12,000 x g for 10 minutes at 4°C to pellet the mitochondria. The mitochondrial fraction was suspended with ice cold 1x M buffer, using a cut edge 200 μL-pipette tip, and stored at -80°C till further processing.

Nuclear and cytosolic extraction

Nuclear and cytosolic extraction was performed as previously described[6] with modifications. Cells were harvested (via scraping) on ice with cytoplasmic buffer (CE buffer, 0.075% v/v NP-40 in 10 mmol/L HEPES, 60 mmol/L KCl, 1 mmol/L EDTA, 1 mmol/L DTT and 1 mmol/L PMSF, pH 7.6) supplemented with protease and phosphatase inhibitors (1 % OA, 1 % OV, 1.2 % PIM), resuspended by pipetting and incubated on ice for 5 minutes. Samples were centrifuged at 10,000 x g for 5 minutes at 4°C in order to separate the cytoplasmic (supernatant) and nuclear (pellet) compartments. The supernatant (cystoplasmic extract) was stored at -80°C for further processing. The pellet was washed 3 times with CE buffer-without NP-40, resuspended in nuclear extraction buffer (NE, 20 mmol/L Tris HCl, 420 mmol/L NaCl, 1.5 mmol/L MgCl2, 0.2 mmol/L EDTA, 1 mmol/L PMSF and 25% (v/v) glycerol, pH 8.0), vortexed and

incubated for 10 minutes on ice with regular vortexing. Finally, samples were centrifuged at 16,000 x g for 5 minutes at 4°C and the supernatant (nuclear extract) was collected and stored at -80°C for further processing.

Immunoprecipitation (IP)

Immunoprecipitations were carried out in 500 µL lysis buffer (1% Triton X100, 50 mmol/L Tris pH 7.4, 150 mmol/L NaCl) containing 500 µg of protein by addition of 0.5 µg from the respective antibody (CSE, #12217-1AP, Proteintech or PDHA1, #PA5-21536, Invitrogen) to the lysate. Prior to addition of the antibody an input sample was collected. The mixture was incubated overnight at 4°C. The next day a 1:1 mixture of Protein A (#17528001, Cytiva) and Protein G (#17061801, Cytiva) Sepharose was equilibrated by washing three times with lysis buffer. After equilibration the bead mixture was added to the lysates and incubated for an additional 2 hours at 4°C. Beads were settled via centrifugation at 500 x g for 2 minutes and the supernatant was removed. This step was repeated twice for a total of three wash steps. Lastly bound proteins were eluted from the beads by addition of 50 µl of SDS based sample buffer and boiling for 3 minutes at 95°C.

Histone extraction and analyses

Histones were isolated according to the protocol published by Shechter et al.[95] In brief, nuclei were extracted by lysing the cells in hypotonic lysis buffer (10 mmol/L Tris/HCl pH 8, 1 mmol/L KCl, 1.5 mmol/L $MgCl_2$) supplemented with 1% OA (#S6508-50g, Merck), 1% OV (#O-5857-1mg, LC laboratories), 0.8% PMSF (#36978, Thermo Fisher Scientific), 1.2% PIM, 1mmol/L DTT (#646563-10X.5ML, Sigma-Adlrich), 10 mmol/L sodium butyrate (#166898-1G, Thermo Fisher Scientific), 5 µmol/L valproic acid (#P4543-10G, Sigma-Aldrich), and 5 µmol/L Ciclopirox (#6384/10, Tocris). Afterwards the histones were extracted by acid extraction using 0.2 mol/L H_2SO_4, precipitated by the use of TCA and dissolved in ddH_2O.

For immunoblotting: Cells were treated with 10 µmol/L of valproic acid (#P4543-10G, Sigma-Aldrich) (to sustain histone acetylation sites) 24 hours and 4 hours prior histone extraction. For glucose depletion studies WT mLECs were washed twice with 1x DPBS with calcium and magnesium and subsequently treated 4 hours before harvesting with DMEM/F12 (#C4022.0500, Genaxxon) supplemented with 2.5 mmol/L L-glutamine (#25030-024; Gibco Waltham), 10% FBS and 1% penicillin/streptomycin. Additionally, the control media was supplemented with 17 mmol/L D-glucose (#HN06.3, Carl Roth). Immunoblotting of histones and analysis was performed as described above ‘‘Immunoblotting’’. Antibodies used: H3 (1:1000, #9715s, Cell Signaling Technology), H3K9ac (1:1000, #39017, Active Motif), H3K14ac (1:1000, #7627T, Cell Signaling Technology), H3K18ac (1:1000, #39755, Active Motif), H3K23ac (1:1000, #39131, Active Motif).

For proteomics: Cells were labelled with 13C6-Cystine for 48 hours under hypoxic conditions at 37°C. SILAC-proteomics and analysis was performed by Creative proteomics.

Cell-cycle inhibition and immunoblotting

Mouse lung endothelial cells from WT (C57BL/6) mice were treated with 800 µmol/L of (2S)-Octyl-alpha-hydroxyglutarate (2-SGH) (#1391194-64-1, Biochrom), which is arresting endothelial cells[60] for 24 hours and 10 µmol/L of valproic acid (#P4543-10G, Sigma-Aldrich) co-treatment 4 hours prior harvesting. Cells were collected and histones extracted as described in ‘‘Histone extraction and immunoblotting’’.

Limited proteolysis mapping

Cells were collected, proteins extracted with 1x DPBS through homogenization, their concentration was measured with BCA protein assay and subsequently were divided into 2 groups. Half of the groups were treated with solvent (H_2O) and the rest with 1 mmol/L cystine for 30 minutes at 37°C. All the samples were then processed with a modified version of the protocol as previously described.[55]

In brief, the samples were treated with proteinase K (15 µg protein were used for SDS-PAGE analysis) and subsequently incubated with a denaturant (UA/DOC) and DTT (to final concentration 20 mM) for 2 hours at 30°C, following cooling to RT. IAA (to final concentration 25 mM) was then added, the samples were shaked at 600 rpm for 1 minute and further incubated for 30 minutes at RT (dark). In order to dilute UA/DOC (to final concentration <1.5 M) NH_4HCO_3 buffer (50 mM) was added and tryptic digestion followed with addition of 2 µg of trypsin and incubation for 16 hours at 37°C. After the digestion, the peptides were sequentially desalted, lyophilized, reconstituted in 0.1% formic acid, their concentration was accessed with OD280 and 2 µg of peptides per sample were spiked with iRT standard peptides and used for mass spectrometry analysis (Shanghai Applied Protein Technology Co., Ltd., Shanghai, China).

The data-independent acquisition (DIA) analysis was utilized and the chromatographic separation was achieve using a nanoflow Vanquish Neo (Thermo Fisher) system. The HPLC-separated samples were further analyzed in DIA mode by an Astral high-resolution mass spectrometer (Thermo Scientific). For the detection a positive ion mode was used (precursor ion scan range: 380-980 m/z) and the full MS resolution was fixed to 240,000, 200 m/z (normalized AGC target: 500%, max. injection time: 5 ms). For MS^2, the used DIA acquisition had 299 scanning windows (isolation window: 2 m/z, HCD collision energy: 25 eV, normalized AGC target: 500%, max. injection time: 3 ms).

The generated DIA data were analyzed using Spectronaut software. The set parametes for the system were the following: (i) retention time prediction type: dynamic iRT, (ii) interference on MS^2 level correction: enabled, (iii) cross-run normalization: enabled. The results were further filtered with Q value cutoff of 0.01 (equivalent to FDR <1%). ProteoWizard msconvert was used to convert all data to mzML and subsequently MS-GF+ searched the data against the SwissProt Homo sapiens database (January 2023) (search

parameters: trypsin digestion, carbamidomethylation (C, fixed), oxidation (M, variable)). To estimate the FDR, a decoy database was applied and the resulted identification were eventually exported in mzIdentML format.

Surface plasmon resonance (SPR)

Recombinant human CSE[86] was immobilized onto a CM5 sensor chip via standard amine coupling chemistry. Briefly, the chip surface was activated with a 1:1 mixture of 0.4 mol/L EDC and 0.1 mol/L NHS for 7 minutes at a flow rate of 10 μL/min in HBS-EP+ running buffer (10 mmol/L HEPES, 150 mmol/L NaCl, 3 mmol/L EDTA, 0.05% v/v surfactant P20, pH 7.4). CSE was diluted to 40 μg/mL in 10 mmol/L sodium acetate, pH 4.5, and injected over the activated surface to achieve a final immobilization level of approximately 600 response units (RU). Remaining active esters were blocked with 1 mol/L ethanolamine-HCl, pH 8.5, for 7 minutes. A reference flow cell was prepared by activation and blocking without protein immobilization. For binding assays, recombinant PDHA1 (#ab125602, Abcam) was diluted in running buffer to final concentrations ranging from 1 to 20 μmol/L, with or without 100 μmol/L freshly prepared cystine. Where indicated, PDHA1 was pre-incubated with cystine for 15 minutes at room temperature before injection. Binding analyses were performed at 25°C with a flow rate of 30 μL/min, an association time of 120 seconds, and a dissociation time of 300 seconds. After each cycle, the surface was regenerated with 10 mmol/L glycine-HCl, pH 2.5, for 30 seconds. Sensorgrams were processed by double referencing against both the reference flow cell and buffer-only injections, and binding kinetics and affinities were determined using a 1:1 Langmuir interaction model within the Biacore T200 evaluation software. Differences in binding responses with and without cystine were quantified to determine cystine dependency of the CSE–PDHA1 interaction.

Proliferation assay by live imaging

Human endothelial cells or FUCCI transduced endothelial cells (described in "Generation of lentivirus and transduction") were seeded in 96-well plates (Sarstedt, Nümbrecht, Germany) in triplicates per condition in ECGM-2. Endothelial cells were treated after 24 hours with Sol. (DMSO) or 10 μmol/L IKE (#27088, Cayman Chemicals) for up to 72 hours to prevent the uptake of cystine or cultured for 24 hours in ΔCC or the control CC medium (composed as described on the section "Cell treatments") and changed back to ECGM-2 after 24 hours.

All endothelial cells were imaged every 2-4 hours in brightfield to access phase contrast confluence levels using Incucyte live cell imaging system (Sartorius, Göttingen, Germany). Images acquired with 10x objective in default settings and an average of 3 to 5 pictures were calculated per well. Data were analyzed using the Incucyte Base Analysis software (Sartorius, Göttingen, Germany) Analysis Definition. In particular, phase analysis was performed with segmentation: AI confluence or Classic confluence (background adjusted), filters: area (μm^2) min adjusted for each experiment and the other settings in default. Proliferation was measured by fold change of confluence to time point 0 hours, unless specified differently. Additionally, the FUCCI cells were imaged with phase contrast and also with green and red fluorescence lamp in incucyte to detect FUCCI cell cycle phases (10x objective, average of 3-5 pictures per well). Phase contrast was analyzed as above. Green signal was calculated using the Analysis Definition green and orange with segmentation: surface fit, adjusted threshold, edge sensitivity and filters: area (μm^2) min for each experiment. FUCCI proliferation was measured by total amounts of green cell counts (G2/M cell cycle phase) to the time point 0 hours, unless specified differently.

Proliferation assay by cell counting

Mouse lung endothelial cells isolated from iEC^{CSE} or its Cre negative (WT) littermates were transduced with $P53^{CRISPR}$ or NTC lentiviruses (as described in the section "generation of lentivirus and transduction") or with adCSE or RFP track adenoviruses and seeded in 24-well plates (Sarstedt, Nümbrecht, Germany) in triplicate per condition in mLEC media. For counting, the cells were washed twice with 1x DPBS and detached using accutase (#A6964, Sigma-Aldrich). Each condition was calculated as the average cell number of the triplicates per condition after 24, 48, 72, 96, and 120 hours using a CASY Cell Counter (OLS OMNI Life Science).

FACS

FACS of FUCCI mice

FUCCI mice were sacrificed at postnatal day 6 and eyes were dissected as described[91] in ice cold 1x DPBS. Retinas were isolated and immediately digested in 0.1 % trypsin (#L2103-20G, Biochrom), 70 U/mL collagenase type I (#C1-22-1G, Thermo Fisher Scientific), 160 U DNase (#11284932001, Roche) in DMEM/F12 medium for 30 minutes at 37°C continuously shaking at 300rpm. Digestion was stopped with DMEM/F12 medium supplemented with 10% FBS and the suspension was filtered through a 40 μm pre-separation filter to remove remaining tissue. Filtered cells were permeabilized with 0.4% Triton X-100 (#9002-93-1, Sigma-Aldrich) for 10 min at 4°C and stained for APC anti-mouse CD144 (1:100, #138012, clone BV13, Biolegend) and SLC7A11 (#PA1-16893, Invitrogen) conjugated, according to manufacturer's instructios, using the DyLight 405 Conjugation kit (#ab201798, Novus biologicals). Live cells were immediately acquired.

FACS sorting of retinal endothelial cells: Retinal endothelial cells were isolated from WT P6 (pEC) and P15 (qEC) pups, and from P6 pups from iEC^{7A11} and iEC^{CSE} or double knock out, stained with APC anti-mouse CD144 antibody (1:100, #138012, clone BV13, Biolegend) and FACs sorted as previously described.[53]

FACS in human endothelial cells

Human endothelial cells (HUVECs) were seeded and treated as described in "Cell treatments" for the respective experiments. Subsequently cells were harvested with accutase (#A6964, Sigma-Aldrich) incubation for 5 minutes at 37°C and termination of the reaction with FACS buffer (2% FBS, 0.5 mM EDTA in 1x DPBS). Live cells were stained with fixable viability stain 510 (1:10,000, #564406,

BD Bioscience) for 5 minutes at RT. Cells were washed once with FACS buffer, fixed with 4% ROTI Histofix (#P087.1, Carl Roth, Karlsruhe, Germany) for 10 minutes at RT and permeabilized with 0.4% Triton X-100 (#9002-93-1, Sigma-Adlrich) in 1x DPBS for 10 min at RT. After washing the cells using FACS buffer, they were stained with SLC7A11 (1:100, #MA5-35360, Invitrogen, Waltham, USA) and goat anti-rabbit Alexa fluor 647 (1:200, #A31573, Invitrogen). The samples were washed and acquired.

For staining with anti-Ki67, the harvested cells after staining with the Fixable viability dye BV510, were washed once with 1x DPBS and fixed with ethanol. In particular, the cell pellet was vortexed shortly to be loose and pre-cool 70% Ethanol was added (according to cell amount) drop-wise with parallel continuous vortexing. The cells were vortexed for additional 30 seconds, and incubated for 1 hour at -20°C. Cells were washed once with 1x DPBS and incubated with anti-Ki67 RB705 (1:100, #570281, BD Bioscience) for 30 minutes at RT protected from light. The samples were washed and acquired. For cell viability assay cells were collected with accutase for 5 min at 37°C, immediately stained with FITC Annexin V apoptosis detection kit I (#556547, BD Bioscience) following the manufacturer's instructions and propidium iodide (1:100) (#130-093-233, Miltenyi Biotec) and acquired.

For lipid peroxidation assay cells were washed once with 1x DPBS with calcium and magnesium and treated with 2 μmol/L BODIPY 581/591 C11 (#D3861, Thermo Fisher Scientific, Waltham, USA) in 1x DPBS with calcium and magnesium for 30 minutes at 37°C. The cells were then washed, harvested with accutase resuspended in 1x DPBS supplemented with 0.5% BSA (#15260037; Gibco) and immediately acquired.

For fibronectin binding assay cells were seeded as in ribosomal RNA experiments for the appropriate time points. FACS analysis was performed using a FITC-fibronectin antibody (2.5 μg/mL) (#60-S1104GND1-AF-22, Fitzgerald), as previously described.[53]

All cells were acquired in LSRFortessa (BD Bioscience, Franklin Lakes, USA) or FACS Canto II (BD Biosciences, Franklin Lakes, US) cell analyzer with FACSDiva software (version 9.0; BD Bioscience, Franklin Lakes, USA). Subsequent analysis was done using FlowJo software (BD Bioscience, Franklin Lakes, USA). FUCCI color Cdt1-mKO2 or Cdt1-mcherry were detected with yellow/green (561) laser and hGem-mAG was detected with blue (488) laser. At least three biological replicates were used for each measurement and a minimum of 10,000 events was measured per sample.

Immunofluorescence and EdU staining

Immunofluorescence in cultured cells

For immunofluorescent imaging, HUVECs or endothelial cells isolated from mice iEC^{CSE} or WT littermates were seeded in 8-well chamber slides (#80806, Ibidi). 4 to 12 hours before fixation cells were treated with 10 μmol/L 5-Ethyl-2-deoxyuridin (EdU) (#900584, Sigma-Aldrich) at 37°C. Cells were fixed with 4% ROTI Histofix (#P087.1, Carl Roth) for 10 minutes at room temperature and washed thoroughly with DPBS. For permeabilization, cells were incubated in 1% Triton X-100 (#9002-93-1, Sigma-Aldrich) in 1x DPBS for 20 min at room temperature. To block non-specific antibody binding sites, the cells were incubated with blocking buffer containing 5% donkey serum (#S30-100ML, Sigma-Aldrich), 0.5% BSA (#15260037, Gibco) and 0.1% Triton X-100 (#9002-93-1, Sigma-Aldrich) in 1x DPBS for 2 hours at room temperature. In case of EdU imaging, the Click-iT EdU Imaging Kit (#C10337, Invitrogen) was used to stain EdU positive cells according to the manufacturer's instruction. Afterwards cells were incubated overnight with primary antibodies diluted in blocking buffer. The cells were then incubated with secondary fluorescently labeled antibodies diluted 1:200 in 1x DPBS, pre-conjugated primary antibodies and DAPI solution (10 ng/mL DAPI in 1x DPBS) for 2 hours at room temperature. In between each steps cells were washed at least once with 1x DPBS for 5 min. Cells were mounted with mounting media (Glycerine 5mL, 1xPBS 4 mL, 1 mL from 1 mol/L DTT; #646563-10X.5ML, Sigma-Adlrich). Antibodies used for HUVEC staining: SLC7A11 (1:100, #26864-1AP, Proteintech), donkey anti-rabbit Alexa-fluor-647 (#A21206, Invitrogen, Waltham, USA), Alexa-Fluor 546 Phalloidin (#A22283, Thermo Fisher Scientific), Anti-VE Cadherin (#ab33168, Abcam).

Immunofluorescence of whole mount retina

Mice from iEC^{7A11}, iEC^{CSE} and WT littermates were sacrificed at postnatal day 6. Eyes and retinas were isolated as previously described.[91] For immunofluorescent staining of isolated mouse retina, the tissue was blocked overnight in blocking buffer containing 3% donkey serum (#S30-100ML, Sigma-Aldrich) and 0.5% Triton X-100 (#9002-93-1, Sigma-Aldrich) in 1x DPBS. Following several washes the tissue was incubated with primary antibodies diluted in blocking buffer overnight at 4°C. After 3 times washing for 5-10 minutes with 1x DPBS, the tissue was stained with secondary fluorescently conjugated antibodies, Isolectin GS-IB$_4$-A647 (1:50) and DAPI solution (10ng/mL) diluted in PBLEC buffer (1% Triton X-100, 1 mmol/L $CaCl_2$, 1mmol/L $MgCl_2$, 0.1 mmol/L $MnCl_2$ in 1x DPBS, adjusted to pH=6.8) overnight at 4°C. The next day, retinas were washed 3-5 times for 5-10 minutes with 1x DPBS and mounted with fluorescent mounting medium (Fluoromount G, #00-4958-02, Invitrogen). Antibodies for whole mount retina: CSE (#12217-1AP, Proteintech), goat-anti rabbit Alexa-fluor-488 (#A21206, Invitrogen), Isolectin GS-IB$_4$-A647 (#I32450, Invitrogen by Thermo Fisher Scientific), SLC7A11 (#26864-1-AP, Proteintech), VIMENTIN (#NCL-L-VIM-V9, Novocastra). For EdU retinal staining, 4 hours prior to sacrifice pups were injected intraperitoneally with 20mg/kg EdU in 1x DPBS and the Click-iT EdU Imaging Kit (#C10337, Invitrogen) was used according to manufacturer's instructions after the secondary antibody staining.

Immunofluorescence of whole mount aortae

Murine aortae were fixed and stained as previously described.[86] In brief, after isolation the surrounding tissue was removed using a stereomicroscope and the aortae were fixed in 4% ROTI Histofix (#P087.1, Carl Roth, Karlsruhe, Germany) for 2 hours at RT and washed with blocking buffer (3% BSA and 0.5% Triton X100 in 1x DPBS). Further staining was perfomed as described above. Antibodies for whole mount aortae: APC anti-mouse CD144 (#138012, Biolegend), Erg1 (#ab92513, Abcam), Click-iT EdU Imaging Kit (#C10337, Invitrogen).

Immunofluorescent of the murine heart

Embedded transversal heart cryosections were incubated at room temperature for 10 or 30 minutes and the Tissue Tek was cleaned with PBS. The tissues were fixed with 4% ROTI Histofix (#P087.1, Carl Roth) for 20 minutes at room temperature and subsequently washed three times with 1x DPBS for 5 minutes at room temperature. The hearts were permabilized with 0.3% Triton X100 or 1% Triton X100 in case of nuclear staining, in 1x DPBS at room temperature, washed three times with 1x DPBS for 5 minutes at room temperature, and DAKO pen was used to mark the area around the tissues. The hearts were then blocked with blocking buffer (0.5% BSA, 0.3% Triton-X100, 5% Donkey serum in 1x DPBS) for 30 minutes at room temperature and incubated with primary antibodies overnight at 4°C. The next day all samples were washed three times with 1x DPBS for 5 minutes at room temperature and immediately incubated with the secondary antibodies, conjugated antibodies and DAPI mix in 1x DPBS overnight at 4°C. The next day samples were washed three times with 1x DPBS at room temperature and mounted with Fluoromount G (#00-4958-02, Invitrogen). Antibodies for heart cryosection staining: anti-Ki67 antibody (1:100, #15580, abcam), goat-anti rabbit Alexa-fluor-647 (#A31573, Invitrogen, Invitrogen), Wheat Germ Agglutinin (#w21405, Invitrogen), Griggonia Simplificolia Lectin I (#FL-1201-.5, Vector Laboratories).

Sirius Red staining of the heart

Hearts were fixed in 4% paraformaldehyde overnight at 4°C, processed, and embedded in paraffin. Sections (5 μm) were deparaffinized in xylene and rehydrated through a graded ethanol series (100%, 95%, 70%) to distilled water. Sections were incubated in Picrosirius Red solution (0.1% Direct Red 80 in saturated picric acid; #365548, Sigma-Aldrich) for 60 minutes at room temperature. After staining, sections were washed twice in acidified water (0.5% acetic acid in distilled water) to remove unbound dye, dehydrated through ascending ethanol concentrations, cleared in xylene, and mounted with a resinous medium. Collagen fibers were visualized by brightfield and polarized light microscopy. Quantification of collagen content was performed using ImageJ software by calculating the Sirius Red–positive area as a percentage of total tissue area in each section. Slides were scanned using Axio Scan.Z1 slide scanner (Carl Zeiss Microscopy GmbH, Germany).

Murine embryo stereomicrographic imaging

Murine whole embryos were isolated at the indicated time points. Subsequently, brightfield images of them were taken using a stereomicroscope (Olympus VS200 and FV1000 (Olympus, China)).

Confocal imaging was performed using the Zeiss LSM 780 and LSM 800 (Carl Zeiss, Jena, Germany) confocal microscope and the ZEN software (Blue and Black, Carl Zeiss, Jena, Germany). All quantification and image analysis were perform using ImageJ software. At least 3 biological replicates were used per condition and a negative control incubated with all the secondary antibodies but not primary was used on every staining. Representative images were chosen on the average intensities calculated from all biological replicates.

RT-qPCR

Total RNA from iEC^{CSE} or its Cre negative (WT) littermates isolated mouse lung endothelial cells was extracted using RNeasy kit (#73404, Qiagen) according to manufacturer instructions. Equal amounts of total RNA (1 μg) were reverse transcribed using Superscript III (Invitrogen) according to instructions. Gene expression levels were detected using SYBR Green (Absolute QPCR SYBR Green Mix; Thermo Fisher Scientifc). The relative expression levels of the different genes studied was calculated using the formula $2-\Delta Ct$ [ΔCt = Ct (gene) – Ct (housekeeping gene)] with the 18S RNA as a reference. The primer sequences used were as follows: 18s: forward 5'-CTTTGGTCGCTCGCTCCTC-3', reverse 5'-CTGACCGGGTTGGTTTTGAT-3'; *Dll4*: forward 5'-TTTGCTCTCCCAGG GACTCT-3', reverse 5'-AGGCTCCTGCCTTATACCTCT-3'; *Hes1*: forward 5'- AATTCCTCGTCCCCGGTGGCT-3', reverse 5'- CT TGGAATGCCGCGAGCTATCTT-3'; *Hey1*: forward 5'- TCGGCTCTAGGTTCCATGTCCCC-3', reverse 5'- AGCTTAGCAGATCCCT GCTTCTCAA-3'.

Persulfidation of whole mount retinas

Mice from iEC^{CSE} and its Cre negative littermates (WT) were sacrificed at postnatal day 6 and day 15. Eyes and retinas where isolated as described.[91,96] Retina tissues was blocked for 4 hours in blocking buffer (5% donkey serum; #S30-100ML; Sigma-Aldrich, 0.5% Triton X-100; #9002-93-1; Sigma-Adlrich, diluted in DPBS). Following several washes with 1x DPBS retina tissues were permeabilized with 1% Triton X-100 (#9002-93-1; Sigma-Adlrich, St. Louis, USA) diluted in DPBS for 2 hours at room temperature. Retinas were stained for persulfidation as previously described.[53] Retinas were mounted with fluorescent mounting medium (#00-4958-02, Invitrogen), imaged using the Zeiss LSM 780 (Carl Zeiss, Jena, Germany) confocal microscope and the ZEN software (Carl Zeiss, Jena, Germany) and data were quantified using ImageJ software.

Spheroid sprouting assay

Spheroid sprouting of HUVEC

Spheroids were generated as described[97] and cultured as indicated for the specific experiments in ECGM-2 supplemented with 10 μmol/L of IKE (#27088, Cayman Chemicals) and solvent or cultured in CC and ΔCC medium (as described in "Cell treatments" section) for 24 hours prior fixation.

Spheroid sprouting of iEC^{CSE}

Mouse lung endothelial cells were isolated from iEC^{CSE} and transduced with a RFP track empty adenovirus or a GFP track CSE adenovirus (adCSE). Spheroids were generated as described above with 1:1 ratio of the RFP and GFP respective cells. Similarly, spheroids were made in iEC^{CSE}, iEC^{SLC7A1}1 and iEC^{SLC7A11xCSE} isolated lung endothelial cells.

Imaging and analysis was performed as previously described.[97]

Aortic ring assay

Mice from WT or iEC^{CSE} and its Cre negative littermates (WT) were sacrificed and aortae were isolated and cultured as previously described.[98] In brief, aortae were isolated and cleaned from surrounding tissue under a strereo miscroscope, embedded in collagen gels and cultured in mLEC media. Aortae from WT mice were treated with 10 μmol/L IKE (#27088, Cayman Chemicals) or Sol. (DMSO) or cultured in mouse cystine deprivation medium with or without supplementation of 100 μmol/L L-cystine (as described in section "cell treatments"). Aortae were cultured up to 7 days in a humidified incubator at 37°C with 5% CO2 with media change every 2 days. For imaging, aortae were stained with anti-CD31 (#555444, BD Bioscience) and secondary antibody goat anti-mouse Alexa Fluor 488 (#A21206, Invitrogen) and imaged using the Zeiss LSM 800 (Carl Zeiss, Jena, Germany) confocal microscope and the ZEN software (Carl Zeiss, Jena, Germany).

Sample preparation for ribosomal RNA and total RNA sequencing

Ribosomal RNA isolation

Ribotag transduced cells (as previously described in Generation of lentiviruses and transduction) were split prior harvesting for the specific time points. Cells were let attach to the flask surface for 2 hours before counting the time after splitting (0, 2, 6, 12, and 24 hours). Cells were harvested by scraping the cells in homogenate buffer (50 mmol/L Tris-HCl, 150 mmol/L NaCl, 12 mmol/L $MgCl_2$, 1% NP-40, 1 mmol/L DTT (#707265ML, Thermo Fisher Scientific), 1.2% PIM, 200 U/mL SUPERase-In RNAse inhibitor (#AM2696, Thermo Fisher Scientific), 100 μg/mL Cycloheximide (#C4859, Sigma Aldrich), 25 U/mL TURBO DNaseI (#AM223, Thermo Fisher Scientific) in ultrapure DNase/RNase free water (#10977-035, Invitrogen) for 10 minutes on ice. Cell nuclei were isolated by breaking the cells 10 times with a 26G needle and centrifuged at 13,000xg at 4°C for 10 minutes to release cell nuclei. The supernatant containing cell nuclear extracts were incubated with Anti-HA-tag magnetic beads (#M180-11, LOT:005 MBL) rotating overnight at 4°C. HA-antibody coated cells were washed 3 times with high salt wash buffer (50 mmol/L Tris-HCl, 300 mmol/L NaCl, 12 mmol/L MgCl2, 0.5% NP-40, 200 U/mL SUPERase-In RNAse inhibitor (#AM2696, Thermo Fisher Scientific), 1 mmol/L DTT (#707265ML, Thermo Fisher Scientific), 100 μg/mL Cycloheximide (#C4859, Sigma Aldrich) in ultrapure DNase/RNase free water (#10977-035, Invitrogen)) using a DynaMag-2 Magnet (#12321D; Thermos fisher Scientific) followed by RNA purification.

Ribosomal RNA and total mRNA were isolated using the RNeasy Plus Universal Mini Kit (#73404; Qiagen) according to the manufacturer's instructions. In brief, cells were lysed in Trizol (#79306; Qiagen) with gDNA Eliminator and separated using chloroform (#7331.2, Carl Roth). The RNA in the aqueous phase was precipitated using isopropanol (#AE73.2, Carl Roth) and transferred to RNeasy mini spin columns. The RNA was eluted in RNase and DNase free water. RNA sequencing was performed and analyzed as previously described.[6]

Library preparation

For total RNA sequencing, RNA and library preparation integrity were verified with LabChip Gx Touch (Perkin Elmer). RNA amounts were normalized and 300 ng of total RNA was used as input for VaZyme_VAHTS Universal Stranded mRNA-seq - V6 (#NR604-01/02, Vazyme). Sequencing was performed on the NextSeq500 platform (Illumina, San Diego, USA) using P3 flowcell with 75bp single-end setup.

For Ribosomal RNA sequencing, RNA amounts were normalized and 500 ng of total RNA was used as input for SMARTer Stranded Total RNA Sample Prep Kit HI Mammalian (#634873, Takara Bio). Sequencing was performed on the NextSeq2000 platform (Illumina, San Diego, USA) using P3 flowcell with 72 bp single-end setup.

Sample preparation for ATAC-sequencing

DNA for ATAC-sequencing was prepared according to the protocol published[99] from endothelial cells isolated from iEC^{CSE} and its Cre negative littermates (WT) mice or from the respective human endothelial cells isolated from young and aged mesenteric arteries as previously described.[6] In brief, cell nuclei were isolated and incubated with illumina DNA Tagment Transposase (#20034198, Illumina) to release open chromatin fragments. DNA fragments were purified using the Zymo ChIP DNA Clean and concentrator Kit (#D5205, Zymo Research) according to the manufacturer's instructions. Amplification of library together with Indexing was performed as described previously.[100] Libraries were mixed in equimolar ratios and sequenced on NextSeq500 platform (Illumina, San Diego, USA) using P3 flowcell with 2x 38bp paired-end setup.

RNA- and ATAC-sequencing analysis

Trimmomatic version 0.39 was employed to trim reads after a quality drop below a mean of Q15 in a window of 5 nucleotides and keeping only filtered reads longer than 15 nucleotides.[101] Reads were aligned to the mouse reference genome (GRCm38; Ensembl release 99 / GENCODE vM25) with STAR 2.7.3a.[102] Alignments were filtered to remove: duplicates with Picard 2.21.7 or 3.1.1 (Picard: A set of tools (in Java) for working with next generation sequencing data in the BAM format) respectively, spliced (in ATAC-seq), multi-mapping, ribosomal, or mitochondrial reads. In the case of ATAC-seq peak calling was performed with Macs version 2.1.1 with

FDR < 0.0001,[103] with peaks overlapping ENCODE blacklisted regions (known misassemblies, satellite repeats) excluded and remaining peaks unified to represent a common set of regions for all samples. In both cases, counts were produced with featureCounts.[104] In particular, for the RNA-seq data gene counts were established with the 1.6.5 version of featureCounts by aggregating reads overlapping exons on the correct strand excluding those overlapping multiple genes. RNA- and ATAC-seq raw count matrices were normalized with DESeq2 version 1.26.0.[105] RNA-seq genes were classified as significantly differentially expressed at average count > 5, adjusted p-value < 0.05, $|\log_2 FC| > 0.585$. The Ensembl annotation for them was enriched with UniProt data (Activities at the Universal Protein Resource (UniProt)). ATAC-seq peaks were annotated with the promoter (TSS +- 5000 nt) of the nearest gene based on Ensembl release 99. Contrasts were created with DESeq2 based on the normalized count peak matrix with all size factors set to one. Peaks were classified as significantly differential at average count > 10 and -1 < log2FC > 1.

Downstream analyses

All downstream analyses are based on the normalized gene or peak (respectively) count matrix. Volcano and MA plots were produced to highlight DEG expression (RNA-seq) or differential peaks (ATAC-seq). A global clustering heatmap of samples was created based on the euclidean distance of regularized log transformed counts. Dimension reduction analyses (PCA) were performed on regularized log transformed counts using the R packages FactoMineR.[106] Gene set overrepresentation analysis (GSO) was performed via KOBAS.[107] One test was executed per contrast using both up- and down-regulated genes to identify perturbed pathways. Bubble plots show pathways with Benjamini-Hochberg corrected p-value < 0.2 (dashed line represents p value < 0.05). Gray circles are scaled to the number of genes comprising the respective pathway, while smaller colored circles represent subsets found to be DEGs. Top50 pathways were selected per contrast.

Directional gene set overrepresentation analysis (GSO) was performed via KOBAS.[107] Two separate tests were executed per contrast using only either up- or down-regulated genes to identify perturbed pathways per direction. Results were combined keeping pathways that showed significant overrepresentation at Benjamini-Hochberg corrected p-value < 0.2 (dashed line represents p value < 0.05) in only one input list (i.e. that were either clearly enriched for up- or down-regulated genes, but not both). Top20 pathways were selected per contrast and direction of regulation.

Gene set enrichment analysis (GSEA) was performed via fGSEA.[108] For non-human organisms, genes were mapped to human symbols by homology based on Ensembl Biomart. All genes (not just DEGs) were ranked per contrast based on log10 transformation of the DESeq2 p-value multiplied with the negative sign of the log2 fold change. This ranks the most significantly different genes at the top/bottom. Weighting scheme for KS statistic was set to "weighted". GSEA was performed using MSigDB collections h/c2.[109] The final table was filtered for gene sets with Benjamini-Hochberg corrected p-value < 0.2.

Transcription factor binding site (TFBS) enrichment analysis was performed with Pscan.[110] Reference TFBS position weight matrices CORE_vertebrates_non-redundant_pfms were extracted from JASPAR on 20221124.[111] In the RNA-seq data overrepresented TFBS were identified based on the promoter region spanning -450 nt upstream to +50 nt downstream of the transcription start site (TSS) of protein_coding genes using DEGs as foreground and all genes as background. In the ATAC-seq data overrepresented TFBS were identified based on peak nucleotide sequences using differential peaks as foreground and all peaks as background. In both cases, the resulting heatmap shows TFs that were significantly enriched with uncorrected p-value < 0.05 in at least one foreground list (yellow = overrepresented).

Statistics

DESeq2 DE: P-value based on Wald test that was corrected for multiple testing using the Benjamini and Hochberg method. Kobas GSO: P-value based on hypergeometric test that was corrected for multiple testing using the Benjamini and Hochberg method. fGSEA: P-value based on multi-level split Monte-Carlo scheme that was corrected for multiple testing using the Benjamini and Hochberg method. Pscan TFBS: P-value based on z-test; no multiple testing correction available by default. TOBIAS: P-value of differential binding based on 1) fitting a two-component gaussian-mixture model to the log-transformed background distribution of scores to estimate a threshold between unbound/bound binding sites, and 2) estimating the significance threshold of the right-most normal distribution (by a user-defined p-value); no multiple testing correction available by default.

ATAC sequencing footprinting data analysis

Digital genomic footprint analysis on ATACseq data was performed using an in-house pre-processing pipeline and the TOBIAS tool.[112] Briefly, we trimmed reads using Trimmomatic (version: v0.39, parameters: EADCROP:0 LEADING:0 TRAILING:0 SLIDINGWINDOW:5:15 CROP:500 AVGQUAL:0 MINLEN:15). For mapping, we used the star algorithm (star: 2.7.3a) and the Mus_musculus mm10 genome assembly and merged replicates into one BAM file per condition. For motif detection within TOBIAS, we used the HOCOMOCO database[113] as version 11_core_MOUSE and excluded the encode blacklisted regions for mm10. Plots were generated using TOBIAS visualization modules.

Enhancer-gene interactions and transcription factor regulation analysis

All ATAC-peaks were considered candidate enhancers and linked to genes with STARE (v.1.0.4)[114] as follows:

STARE.sh -b MLEC_ATAC_Peaks.bed -n 5,6 -a gencode.vM25.annotation.gtf -w 5000000 -f False -t 0.02 -g GRCm38.p6.genome.fa -s Jaspar_Hocomoco_Kellis_mouse_transfac.txt -o <output_path>

The mean ATAC read counts per condition were used as metric for enhancer activity and a contact estimate for contact frequency. The gene annotation version vM25 from GENCODE was used.[115] Differential ATAC-peaks were assigned to the genes with which they formed a gABC interaction in either WT or CSE^{iEC}.

Transcription factor binding sites in ATAC-peaks were called with FIMO[116] with a p-value cutoff ≤ 0.0001. The average base content of all ATAC-peaks was used as sequence background. Transcription factor motif enrichment was done with SEA,[117] for which

the sequences of the differentially accessible enhancers of down-regulated DEGs were compared to the sequences of non-differential enhancers of downregulated DEGs. The same procedure was repeated for upregulated DEGs. A gene was considered differentially expressed if it had an FDR $\leq$ 0.05, an absolute log2FC $\geq$ 0.585, and $\geq$ 5 read counts in either condition. As TF motifs a non-redundant collections assembled from JASPAR 2022,[111] HOCOMOCO v11,[113] and the study of Kheradpour and Kellis[118] was used (https://github.com/SchulzLab/STARE/blob/main/PWMs/2.2/ Jaspar Hocomoco Kellis mouse transfac.txt). Only TFs that had an RNA read count $\geq$ 5 in either condition were considered.

The mapping of gene names to Ensembl IDs was done with GENCODE's vM25 gtf-file and with the API of MyGene.info.[119–121] bedtools (v2.29.2)[122] and pybedtools (v0.8.1)[123] were used for intersecting genomic regions and getting their sequence.

ACT sequencing

Antibody-guided chromatin tagmentation (ACT-seq) was performed as previously described.[58]

All analyses were performed in R version 4.3.3 (2024-02-29), on Ubuntu 24.04.2 LTS (x86_64-pc-linux-gnu, 64-bit), using the following BLAS and LAPACK libraries as provided by Ubuntu (libblas.so.3.12.0 and liblapack.so.3.12.0). A full session info file with all package dependencies is available upon request.

A standard results directory structure was generated, with subfolders for each analysis stage (metadata, alignments, deduplicated BAMs, coverage, peak calling, counts, differential results, annotation, heatmaps, PCA, GSEA, volcano plots). Paired-end reads were aligned to the mm10 mouse reference genome GRCm38/mm10 using Bowtie2 v2.5.4 (parameters: –local –very-sensitive –no-mixed –no-discordant –phred33 -I 10 -X 700). Alignment output was piped to samtools for BAM conversion and coordinate sorting. Read group information was added to each BAM file using samtools addreplacerg. BAMs were indexed at each step.

Duplicate reads were removed using Picard MarkDuplicates (REMOVE_DUPLICATES=true). Output deduplicated BAMs were indexed and used for downstream analysis.

Read coverage was calculated using deepTools bamCoverage (RPKM normalization, 20 bp bin size, smoothing of 40 bp), with output as BigWig files for visualization in genome browsers.

All deduplicated BAMs were merged using samtools merge to maximize sensitivity for peak calling. Broad peaks were called from the merged BAM using MACS3 (–broad –nomodel -g mm -q 0.01 –shift -75 –extsize 200 –keep-dup all). Peaks were output as broadPeak files.

For each peak, raw read counts per sample were computed using bedtools multicov with the deduplicated BAMs and the broadPeak file as input. The resulting count matrix was saved as a tab-separated text file. Peaks were annotated using ChIPseeker and TxDb.Mmusculus.UCSC.mm10.knownGene, assigning genomic annotation (e.g., promoter, exon, intron, intergenic) and gene symbols using org.Mm.eg.db. Peaks were defined as ±3 kb from TSS for promoter assignment. For each mark, and for each group comparison, the following steps were performed:

- Peak-level count data were subset for relevant samples and groups.

Peaks with zero counts in all samples were filtered out.

- A DESeq2 dataset was constructed (DESeqDataSetFromMatrix), and differential analysis was performed using the default DESeq2 workflow.
- Significant differentially enriched peaks (FDR < 0.05) were identified.
- Results were merged with peak annotation information.
- For each group, mean log2CPM per group was computed and included in the result tables.
- All results were exported to Excel files using openxlsx.

For the visualization and exploratory analysis the following were used:

- Heatmaps: Significant peaks were visualized by group mean log2CPM using ComplexHeatmap and custom color schemes.
- Pie Charts: The genomic annotation distribution of significant peaks per group was visualized using ggplot2(pie/bar plots), showing the breakdown of promoter, enhancer, intergenic, etc., annotations.
- Gene Set Enrichment Analysis (GSEA): For each acetylation mark (and for all combined), significant genes (from peak annotation) were mapped to Entrez IDs using clusterProfiler (bitr function).
- KEGG pathway enrichment: Performed with enrichKEGG (organism: mmu, p-value cutoff 0.05), with results visualized via dotplots.
- GO enrichment: Performed using enrichGO for Biological Process (BP) and Molecular Function (MF), p-value cutoff 0.05, q-value cutoff 0.2, Benjamini-Hochberg correction.

Stable isotope tracing

Human endothelial cells and mouse lung endothelial cells from iEC^{CSE} and its Cre negative littermates or WT mice were seeded and cultured in ECGM-2 24 hours prior treatment.

Tracing studies for human endothelial cells were performed in custom formulated DMEM/F12 cystine/cysteine depleted media as described in "cell treatments." The custom formulated media was supplemented with 100 μmol/L of 13C6-34S-Cystine (#CSLM-11349-PK, Cambridge Isotope Laboratories, custom synthetized) or 100 μmol/L 13C3-L-Cysteine (#CLM-4320-H-0.1, Cambridge Isotope Laboratories). For tracing with 13C6-Glucose, cells were cultured in DMEM/F12 (#C4022.0500, Genaxxon) supplemented with 2.5 mmol/L L-glutamine (#25030-024; Gibco), 10% FBS and 1% penicillin/streptomycin and 17 mmol/L 13C6-Glucose (#389274-1G, Sigma-Aldrich). For 13C16-palmitic acid and 34S-methionine tracing, cells were cultured in custom formulated DMEM/F12 as previously described supplemented with 100 μmol/L U-13C16-palmitic acid (#CLM-309-PK, Cambridge Isotope Laboratories) or 100 μmol/L 34S-methionine (#CAS 1006386-95-3, Santa Cruz) and sterile filtered 100 μmol/L L-cystine (#C7602, Sigma-Aldrich). Endothelial cells were labelled with stable isotopes for 2 hours up to 24 hours. Cells were harvested by scraping the cells in media, washed with ice-cold DPBS and snap freezed in liquid nitrogen until extracting metabolites for metabolomics measurement. Tracing studies of isolated mouse lung endothelial cells were performed in custom formulated DMEM/F12 cystine/cysteine depleted media as described in "cell treatments."

For sorted murine retinal endothelial cells, following sorting of p6 CD144 positive endothelial cells, cells were recovered with 2% orthologous mouse serum in 1x DPBS supplemented with the respective heavy labelled metabolites as described above.

Targeted metabolomics measurement

Targeted metabolomics of human umbilical vein endothelial cells, isolated mouse lung endothelial as well as FACS sorted endothelial cells from murine retina were performed by Metabolomics Core Facility (Stephan Klatt, Institute for Vascular Signaling, Goethe University, Frankfurt am Main) and the Shanghai Applied Protein Technology Co., Ltd., Shanghai, China.

Cell preparations

For cultured endothelial cells, cells were incubated for 2 hours in PBS with calcium and magnesium in the presence of 0.1% fatty acid free BSA (Albumin, Bovine Serum, Fraction V, Fatty Acid-Free, Nuclease- and Protease-Free, #126609, Sigma-Aldrich) prior to the tracing experiment.

For FACS sorted cells, cells were collected in ice cold PBS with calcium and magnesium and 0.1% fatty acid free BSA and remained for 1 hour prior to the tracing experiment.

Quantification of amino acids and biogenic amines: Circulating aminogram

Free amino acids in plasma from the human cohort or from mice were measured as previously described in detail.[86]

Cysteine persulfide was detected as previously described.[47] In brief, cells were lysed in ice-cold Triton X-100 buffer (50 mmol/L Tris/HCl pH 7.5, 150 mmol/L NaCl, 20 mmol/L NaF, 10 mmol/L Na4P2O7, 1% Triton X-100 (#9002-93-1, Sigma-Adlrich)) supplemented with protease and phosphatase inhibitors (1 % OA, 1 % OV, 1.2 % PIM, 0.8 % PMSF). The lysate was sonicated for 10 seconds at 80% using the Sonoplus mini20 (Bandelin, Berlin, Germany) and centrifuged at 16,000 x g for 5-10 minutes at 4 °C. The supernatant was collected and used for protein concentration determination using the Bradford protein assay. Equal amounts of protein (250 μg) were used per reaction for amino acid profiling. For plasma analysis 100 μl were used. Sample preparation was performed using the EZ:faast LC-MS free amino acid analysis kit (Phenomenex, Aschaffenburg, Germany) according to the manufacturer's instructions, with minor modifications. Internal standards (10 μL) were applied to all samples and to the standard curve. Sample pH was adjusted to be between pH 1.5-6.0 with hydrochloric acid. Analysis of metabolites was performed by LC-MS/MS using the EZ:faast AAA-MS HPLC column (inner diameter 2 mm) on an Agilent 1290 Infinity LC system (Agilent, Waldbronn, Germany) coupled to a QTrap 5500 mass spectrometer (Sciex, Darmstadt, Germany). Electrospray ionization in positive mode was employed. The intensity of the measured metabolites was normalized to internal standards. Analyst 1.6.2 and MultiQuant 3.0 (Sciex, Darmstadt, Germany) were used for data acquisition and analysis, respectively.

Quantification of tricarboxylic acid cycle metabolites

Cells were lysed in ice-cold Triton X-100 buffer supplemented with protease and phosphatase inhibitors (1% OA, 1% OV, 1.2% PIM, 0.8% PMSF). The lysate was sonicated for 10 seconds at 80% using the Sonoplus mini20 (Bandelin, Berlin, Germany) and centrifuged at 16,000 x g for 5-10 minutes at 4°C. The supernatant was collected and used for protein concentration determination using the Bradford protein assay. Equal amounts of protein (100 μg) were used per reaction for TCA cycle analysis and mixed with a 5-fold volume of methanol and the 2.5-fold volume of isotope-labeled internal standard in water/methanol (50/50). Samples were evaporated in a vacuum concentrator plus (Eppendorf, Hamburg, Germany) at 30 °C, resolved in 50 μL water and subsequently transferred to the LC-MS system. Conditioned medium was mixed 1:1 with isotope-labeled internal standard in water and subsequently transferred to the LC-MS system.

LC-MS/MS was performed on an Agilent 1290 Infinity LC system (Agilent, Waldbronn, Germany) coupled to a QTrap5500 (Sciex, Darmstadt, Germany). Reversed-phase LC separation was performed using a Waters Acquity UPLC HSS T3 column (150 mm × 2.1 mm, 1.8 μm (Waters, Eschborn, Germany)) at 40 °C. Gradient elution was performed with 0.15 % formic acid in water (mobile phase A) and 0.15 % formic acid in acetonitrile (mobile phase B) at a flow rate of 400 μL/minute. Gradient conditions were 2 % B for 1.5 minutes, followed by a 3 minutes gradient to 100% B, followed by a cleaning and equilibration step, making 10 minutes total LC run time. Injection volume was 2.5 μL for all samples. The autosampler temperature was 6 °C. Electro spray ionization at 400 °C with -4500 V in negative ionization mode was employed. Ion source gas parameters were as follows: CUR 30 psi, GS1 45 psi, GS2 25 psi. The specific MRM transition for every compound was normalized to appropriate isotope labeled internal standards. Calibration curves were performed with authentic standards. Analyst 1.6.2 and MultiQuant 3.0 (Sciex, Darmstadt, Germany), were used for data acquisition and analysis, respectively.

Quantification of 13C-labelled TCA and 13C-labelled amine metabolites (from metabolic flux)

Cells were washed with ice-cold 1x PBS and harvested in 1 mL of ice-cold 85 % methanol. Next, cells were sonicated on ice for 3 minutes and briefly vortexed, incubated on ice for 20 minutes and sonicated again for 2 minutes. Proteins were pelleted at 14,000 rpm for 10 minutes at 4 °C. From the supernatant, 800 μL were used for TCA-flux metabolite analysis, whereas 200 μL were used for amine-flux analysis .

TCA-flux metabolite analysis

Samples were diluted 1:3 with MilliQ water, put onto dry ice until frozen and subsequently sublimated on a freeze-dryer (Alpha 3-4 LSCbasic, Martin Christ, Osterode am Harz/Germany). Dried samples were reconstituted in 50 μL of 85 % acetonitrile and transferred to MS-glass vials. Data acquisition was performed via ESI-LC-MS/MS in negative ionization dynamic MRM mode on an Agilent 1290 Infinity II Bio LC system coupled to a 6495C QQQ (both Agilent Technologies, Waldbronn/Germany). The gas temperature was set to 240 °C and the gas flow to 19 L/min. The nebulizer was set to 50 psi. The sheath gas flow was set to 11 L/min, with a temperature of 400 °C. The capillary voltage was set at 1000 V with a nozzle voltage of 500 V. The voltages of the High-Pressure RF and Low-Pressure RF were set to 100 and 70 V, respectively. A peak width of 0.07 minutes was used, with a cycle time of 1100 ms and a min/max dwell time of 4.92 ms and 262.2 ms. Metabolites (including 13C-labelled isotopologues) were identified with authentic standards and/or via retention time, elution order from the column and 1-2 transitions. Reversed-phase LC separation of metabolites was achieved by using an Acquity UPLC HSS T3 1.8 μm (2.1 x 150 mm) column (Waters). Metabolites eluted with a flow-rate of 0.3 mL/min and with the following 15 minutes gradient: 0 – 0.1 min 1% B, 0.1 – 8 min 50% B, 8.1 min 99% B, 8.1 – 11 min 99% B, 11.1 min 1% B, 11.1 – 15 min 1% B. In addition, there was a 2 minutes post-time run per sample. Solvent A consisted of 100 % water containing 0.1% formic acid and solvent B consisted of 100% acetonitrile containing 0.1% formic acid. Column oven temperature was set to 40°C, and the autosampler was set to 4°C. Injection volume was 5 μL.

Amine-flux analysis: 700 μL of MilliQ water was added to the samples, containing 100 μg/mL homotaurine as internal standard. Next, the samples were freeze-dried as above and reconstituted in 80 μL of boric acid buffer. After incubation on ice for 15 minutes, samples were briefly vortexed and derivatized with 20 μL AQC reagent (from AccQ-Tag derivatization kit, Waters, Milford/MA/USA) for 10 minutes at 55 °C. During the derivatization step with 6-Aminoquinolyl-N-hydroxysuccinimidyl carbamate, a chemical group is added to each amine-containing metabolite, enhancing the ionization capabilities within the mass spectrometer 5-50-fold. After 10 minutes, the samples were put on ice briefly, and centrifuged at 14,000 rpm for 10 minutes at 4°C to remove lipids and any insoluble material. The supernatant was transferred to MS-glass vials and then analyzed. Data acquisition was performed via ESI-LC-MS/MS in positive ionization dynamic MRM mode on an Agilent 1290 Infinity II Bio LC system coupled to a 6495C QQQ (both Agilent Technologies, Waldbronn/Germany). The gas temperature was set to 290 °C and the gas flow to 20 L/min. The nebulizer was set to 45 psi. The sheath gas flow was set to 11 L/min, with a temperature of 400 °C. The capillary voltage was set at 3800 V with a nozzle voltage of 500 V. The voltages of the High-Pressure RF and Low-Pressure RF were set to 150 and 60 V, respectively. A peak width of 0.07 minutes was used, with a cycle time of 800 ms and a min/max dwell time of 4.92 ms and 262.2 ms. Metabolites (including 13C-labelled isotopologues) were identified with authentic standards and/or via retention time, elution order from the column and 1-2 transitions. Reversed-phase LC separation of metabolites was achieved by using an Agilent ZORBAX Extend RR HD 1.8μm (2.1 x 150 mm) column (Agilent Technologies). Metabolites eluted with a flow-rate of 0.3 ml/min and with the following 19 minute gradient: 0 – 2 min 1% B, 2 – 9 min 15% B, 9 – 14 min 30% B, 14 – 16 min 60% B, 16 – 17 min 65% B, 17 – 19 min 1% B. In addition, there was a 2 minute post-time run per sample. Solvent A consisted of 100% water containing 0.1% formic acid and solvent B consisted of 100% acetonitrile containing 0.1% formic acid. Column oven temperature was set to 30 °C, and the autosampler was set to 4 °C. Injection volume was 5 μL. Data were analyzed using the Metaboanalyst 5.0.

AlphaFold 3 prediction model and molecular docking

The AlphaFold 3 model was used to predict the interactions between the proteins CSE, PDHA1 and the metabolite cystine (CC). As input the protein sequences were obtained from UniProt (FASTA forma) and the metabolite structure from PubChem or ChEMBL (SMILES format). The AlphaFold 3 model was employed through the public AlphaFold Server or locally via the open-source model weights (default settings). Molecular docking was performed using AutoDock. The binding pocket for cystine was identified based on the method described by.[56] A distance cutoff of 4.0 Å was applied to define close contacts between cystine and the protein complex. To further evaluate the effect of cystine on protein–protein interactions, the binding affinity between CSE and PDHA1 was calculated using MDAnalysis-based tools.[57]

QUANTIFICATION AND STATISTICAL ANALYSIS

Statistics and reproducibility

Statistical analyses were performed using GraphPad Prism 10 (V. 10.1.1, GraphPad Software, Boston, USA). All data are represented as mean ± SD. P values of <0.05 were considered as statistically significant. All data were analyzed for normal distribution using the Kolmogorov-Smirnov test. For normal distributed groups, statistical analysis was performed using Student's t-test for unpaired and paired data. For paired samples that did not follow normal distribution Wilcoxon test was performed: for unpaired samples that did not follow normal distribution Mann-Whitney test was performed. One-way ANOVA (Tukey's or Sidák's multiple comparison tests), two way ANOVA (followed by Tukey's multiple comparisons test) and Kruskal-Wallis test followed by Dunn's test were used where appropriate. Statistics for metabolomics were performed with Metaboanalyst 5.0. Statistical tests, biological and technical replicates (replication) are described in the Data S1. All studies where performed blindly. No data were excluded from the analysis.